



POLITECNICO
MILANO 1863

SCUOLA DI INGEGNERIA INDUSTRIALE
E DELL'INFORMAZIONE

Stability and Charge Transport Investigation of Cumulenic sp-Carbon Wires for Organic Electronics

MASTER DEGREE THESIS IN
MATERIALS ENGINEERING AND NANOTECHNOLOGY

Author: **Elda Tara Hjördis Sala Ruben**

Student ID: 962874
Advisor: Carlo Spartaco Casari
Co-advisors: Stefano Pecorario, Mario Caironi
Academic Year: 2021-22

ABSTRACT

Carbon is a truly versatile element. Essential to life, it can display a large variety of properties, according to the hybridisation of its orbitals.

Among the many sectors carbon-based materials have found applications in, one in particular has experienced a sudden development: organic electronics. After all, living beings, constituted by carbon in a large amount, have found several ways to transport electrical signals. They exploit charge transport mechanisms different from those exploited in standard electronics, which is based on inorganic semiconductors.

Organic semiconductors (OSCs) offer some remarkable features, such as easy processability, flexibility, a wide selection of molecules, biodegradability and biocompatibility. For instance, devices like organic light emitting diodes prove the potential of OSCs in electronics.

A particularly promising category of OSCs is that of highly conjugated *sp*-hybridised molecules, i.e., cumulenes and polyynes. Although theoretical studies have been conducted on them, there is still much to learn, starting from charge transport mechanisms in molecular assemblies, to technological applications, which have been hindered by the notorious reactivity of *sp*-carbon chains. However, organic field effect transistors (OFETs) based on *sp*-molecules, Tetraphenyl[3]cumulene (henceforth named [3]Ph) have been fabricated recently, paving the way for further investigation of these systems in organic electronics.

In this thesis work, thin films of a similar but longer and more conjugated molecule, Tetraphenyl[5]cumulene ([5]Ph), have been optimised to act as active layer in OFETs. Moreover, photo and thermal stability of both [3]Ph and [5]Ph have been investigated, as the properties of such materials in thin films are still largely unknown, and suitable operative conditions should be assessed, in order to discover their true potential.

As a matter of fact, combining the knowledge acquired on [3]Ph, taken as a reference, and the results of the stability tests, it was possible to fabricate [5]Ph transistors with a field effect mobility up to 10^{-3} cm²/Vs and a nearly ideal behaviour, proving that [5]Ph films are well applicable in organic electronics.

Key-words: *sp*-carbon atom wire, cumulenes, carbyne, organic electronics, ofet, stability.

SOMMARIO

Il carbonio è un elemento assai versatile. Essenziale alla vita, può esibire una grande varietà di proprietà, in base all'ibridazione dei suoi orbitali.

Fra i numerosi settori in cui i materiali di carbonio hanno trovato applicazione, uno in particolare ha compiuto una crescita improvvisa: l'elettronica organica. D'altronde, gli esseri viventi, costituiti in larga parte da carbonio, hanno trovato diversi modi per trasmettere segnali elettrici, sfruttando meccanismi di trasporto di carica diversi da quelli utilizzati nell'elettronica tradizionale, basata sui semiconduttori inorganici. I semiconduttori organici (OSC) offrono alcune notevoli qualità, come ad esempio la facilità nel processarli, la flessibilità, una vasta gamma di molecole fra cui scegliere, la biodegradabilità e la biocompatibilità. A riprova di ciò, i LED organici hanno dimostrato la validità dei materiali a base di carbonio nell'elettronica organica. Una categoria di OSC particolarmente promettente è quella delle molecole a ibridazione *sp*, molto coniugate, come cumuleni e polyne. Nonostante siano stati condotti studi teorici su questi materiali, c'è ancora tanto da apprendere, a partire dai meccanismi di trasporto di carica, per arrivare alle applicazioni tecnologiche, che sono state ostacolate dalla nota reattività delle catene di carbonio *sp*. Tuttavia, di recente, sono stati fabbricati dei transistor organici a effetto di campo (OFET), contenenti una delle sopraccitate molecole, Tetraphenyl[3]cumulene (d'ora in poi chiamato [3]Ph), come materiale attivo, aprendo la strada a futuri studi su questi materiali per l'elettronica organica.

In questo lavoro di tesi, è stata ottimizzata una molecola simile, ma più lunga e coniugata, Tetraphenyl[5]cumulene ([5]Ph), da impiegare come materiale attivo in OFET. Inoltre, è stata studiata la stabilità termica e alla luce di entrambe, [3]Ph e [5]Ph, dato che le proprietà di questi materiali in film sottile sono ancora perlopiù sconosciute e che definire delle condizioni operative adeguate è fondamentale per poter raggiungere il loro vero potenziale. Difatti, combinando le conoscenze acquisite sul [3]Ph, usato come termine di paragone, ai risultati delle prove di stabilità, è stato possibile fabbricare transistor a base di [5]Ph con una mobilità d'effetto di campo di $10^{-3} \text{ cm}^2/\text{Vs}$ e un trend di transfer quasi ideale, a dimostrazione del fatto che [5]Ph può essere utilizzato con successo nell'elettronica organica.

Parole chiave: carbonio *sp*, cumuleni, carbene, elettronica organica, ofet, stabilità.

CONTENTS

Abstract	i
Sommario	iii
Contents	v
Introduction	1
1. <i>sp</i>-carbon atomic wires	3
1.1 <i>sp</i> -hybridisation	4
1.2 Cumulenes and polyynes	5
1.3 Tuneability.....	8
2. Organic Field Effect Transistors	11
2.1 Working principle of OFETs.....	11
2.2 OFET architectures.....	15
2.3 Active layer in OFETs.....	16
2.3.1 Doping organic semiconductors.....	18
2.3.2 Charge transport in organic semiconductors	18
2.4 Charge injection.....	21
2.5 Hysteresis.....	22
3. Materials and Methods	25
3.1 Materials	25
3.1.1 Active layer	25
3.2 Device fabrication.....	28
3.2.1 Source and drain deposition	28
3.2.2 Active layer deposition.....	32
3.2.3 Dielectric deposition	35

3.2.4	Gate deposition.....	36
3.3	Characterisation techniques	38
3.3.1	Polarised optical microscopy	38
3.3.2	UV-Vis spectroscopy	39
3.3.3	Semiconductor parameter analysis.....	41
3.3.4	Atomic force microscopy	43
4.	Experimental results – Film deposition and characterisation	45
4.1	[5]Ph optimisation	45
4.1.1	Solution formulation	46
4.1.2	Deposition temperature	49
4.1.3	Nitrogen flow	52
4.1.4	Bar parameters.....	53
4.2	Thin film characterisation.....	53
4.2.1	UV-Vis spectroscopy	53
4.2.2	Atomic force microscopy	55
4.2.3	Ultraviolet photoelectron spectroscopy.....	58
5.	Experimental results – Stability	61
5.1	Stability in air and ageing.....	61
5.2	Photosensitivity	62
5.2.1	Photosensitivity in solution	62
5.2.2	Photosensitivity in solid state.....	67
5.3	Thermostability.....	71
5.3.1	Thermostability in solution	73
5.3.2	Thermostability in solid state	76
6.	Experimental results – Electrical measurements.....	81
6.1	[3]Ph	81
6.1.1	[3]Ph as a reference	81
6.1.2	Optimisation of transistors based on [3]Ph	82
6.2	[5]Ph	87

6.2.1	Transistors in BGBC configuration.....	87
6.2.2	Transistors in TGBC configuration.....	90
6.2.3	Transistors based on [5]Ph:PS.....	94
6.2.4	Transistors based on [5]Ph:PMMA.....	95
6.2.5	Instability in transistors based on [5]Ph.....	97
Conclusions and future work		103
Bibliography		107
List of Figures.....		115
Acknowledgements.....		123

INTRODUCTION

One of the most interesting characteristics of carbon is its versatility, which is a direct consequence of its capability of bonding with itself in many different allotropic forms.

Especially in recent years, carbon has proved to be an essential asset to the technological progress. In particular, its more recent allotropic forms are conquering more and more attention, due to the incomparable properties they feature. For example, nanotubes are considered the mechanically strongest material that is known, and fullerenes are the most efficient acceptors in the photovoltaic sector [1]. Carbon seems to be an element of superlatives.

One of the sectors that has developed the most in the last decade is that of organic electronics. Although organic semiconductors do not seem to hold up to their inorganic counterparts in terms of charge mobility and overall electrical performance [2], they retain some advantages: easy processability, easy tailoring of molecules, mechanical flexibility, and biocompatibility [3]–[6]. All these perks open the door to new applications, such as edible and wearable electronics, as well as to a more sustainable approach to electronics.

This thesis work enquires a particular category of organic semiconductors, which are based on *sp*-hybridised molecules, whose predicted properties are extremely promising.

Infinite *sp*-carbon atomic wires, i.e. carbyne, are considered the most elusive allotropic form of carbon. This is due to the reactivity associated to *sp*-carbon and its tendency to crosslink [7]–[11]. Although extensive theoretical study has been dedicated to carbyne, this explains the lack of experimental data and technological applications regarding even its derivatives, i.e. cumulenes and polyynes.

In recent years, though, field effect transistors have been successfully fabricated, employing as active layer a thin film of a cumulenenic molecule, i.e. Tetraphenylbutatriene ([3]Ph) [12], [13].

This thesis work focuses on the stability and on further optimisation of transistors based on [3]Ph, as well as another cumulene, Tetraphenylhexapentaene ([5]Ph), which holds promise as its backbone is longer and more conjugated. Employing them in transistors, since they work as semiconductors by exploiting the field effect, is a way to study and understand the actual potential behind *sp*-hybridised carbon.

The first two chapters of this thesis are dedicated to an introduction to *sp*-carbon and to organic field effect transistors.

After an explanation about the materials and the methods used during the experiments in Chapter 3, the next three chapters deal with the experimental results.

Chapter 4 focuses on the optimisation of [5]Ph thin films, setting the already optimised [3]Ph as a reference. Moreover, film characterisation is presented through all the techniques employed to analyse and monitor the stages of the development of a good [5]Ph film.

Chapter 5 is dedicated to the stability tests, carried out in order to assess suitable operative conditions to avoid any degradation on [3]Ph and [5]Ph. Mostly, light and heat are the *stimuli* that have been enquired.

Finally, Chapter 6 presents the electrical analysis results, with commentary on the transistor performances and on differences between [3]Ph and [5]Ph.

1. SP-CARBON ATOMIC WIRES

It is widely known that carbon can bond with itself in several different allotropic forms.

This happens because its $2s$ and $2p$ orbitals are only slightly different in energy, and as such they can almost be considered degenerate. By linearly combining them, molecular orbitals can be obtained.

The hybridisation of those orbitals can occur in three different ways. When the orbitals hybridise to form four equivalent σ -bonds, the carbon atoms are said to be sp^3 -hybridised. The resulting material is called diamond, which is an electrical insulator, due to the single bonds. As a matter of fact, from those bonds, their disposition in space and their vibrational behaviour, many more properties can be inferred. This thesis work is mainly focused on charge transport, so that is the aspect that will be discussed first and foremost, but in reality the study of carbon bonds is key to understand the incredible versatility of this element.

It is possible that one of the three $2p$ orbitals is left unhybridised, so three σ -bonds will be formed and the left $2p$ will contribute to create π -conjugation, which is related to orbitals delocalised over more than two atoms and which lends the material a conducting character along the direction of the π -bond. This is sp^2 -hybridised carbon: graphite, graphene, carbon nanotubes and fullerenes are all made of sp^2 carbon atoms.

Both sp^2 and sp^3 carbon are very stable and commonly employed materials, although diamond is not so easily found in nature, since its formation requires high temperatures and pressures.

Carbon can also hybridise its orbitals in a third way: it can form two σ -bonds and two π -bonds, achieving sp -hybridisation. Given that π -conjugation favours conductivity, due to π -clouds being easily polarisable, it is predicted, and confirmed by calculations as well as by experimental data, that sp -carbon might retain very interesting charge transport properties.

Figures 1.1(a)-(c) are the schematic representations of carbon hybridised in sp^3 , sp^2 , sp , respectively.

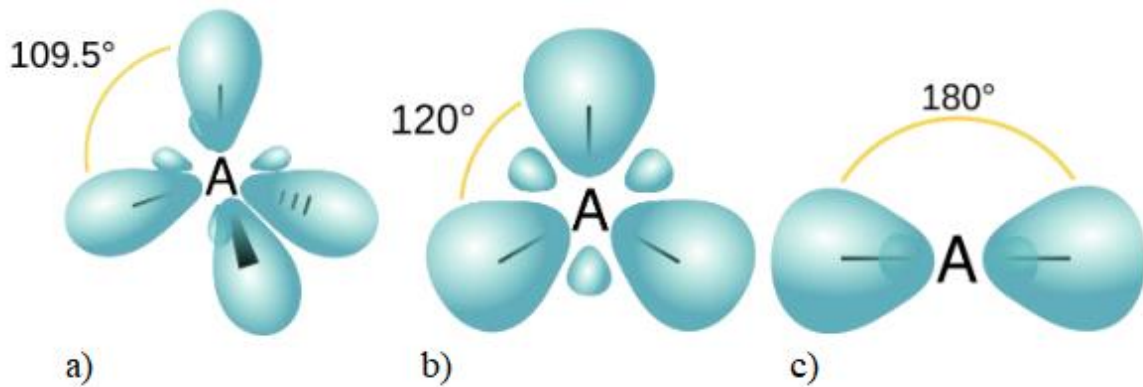


Figure 1.1 Carbon orbitals in a) sp^3 -hybridisation; b) sp^2 -hybridisation; c) sp -hybridisation.

1.1 sp -hybridisation

When carbon is sp -hybridised, it arranges itself in 1D linear chains of monoatomic thickness. The ideal, infinitely long material based on this is called carbyne. Actually, another definition of carbyne refers to a bulk material, made of parallel sp -carbon chains, interacting through weak Van der Waals forces [14].

As a matter of fact, the possibility of the existence of carbyne is up to question because of the notorious reactivity of sp -chains [7], [9]–[11], [14]–[16]. π -bonds are more energetic than σ -bonds, meaning that being in a linear chain is not an energetically favourable configuration for carbon. On the contrary, the planar structure of sp^2 -carbon or the tetragonal one of sp^3 are extremely stable, and sp -carbon tends to crosslink to lower its energy. Indeed, long carbyne chains have only been found within multi-wall carbon nanotubes, which acted as a barrier.

While an infinite chain of carbyne has not been synthesised yet, thanks to density functional theory (DFT) calculations it is possible to have an esteem of the properties expected from this material. It is supposed to have extremely high Young modulus, at 32 TPa, even higher than carbon nanotubes [17]. Carbyne effective area was calculated to be 13 000 m²/g, which is four times that of graphene [18]. Thermal conductivity is quite high as well, between 80 and 200 kW/m K, which is higher than that of graphene and carbon nanotubes [19]. This has been related to the remarkable vibrational activity that carbyne and sp -carbon based molecules display [20]: in particular, a very active effective conjugation coordinate (ECC) mode is present, giving rise to Raman signals in a region (1800 – 2300 cm⁻¹), which is uncovered by other carbon based materials [21]–[23]. Indeed, Raman spectroscopy has been largely employed to investigate molecules based on sp -carbon [21]–[25].

Above all, carbyne electrical properties are considered extremely interesting, as they are tuneable, ranging from insulator/semiconductor to metallic character.

1.2 Cumulenes and polyynes

It is now time to explain that carbyne can present in two different configurations.

The first one, referred to as polyynes, display an alternation of single and triple bonds. This generates a bond length alternation (BLA, equal to $|r_1 - r_2|$) different from zero, as can be observed in Figure 1.2(a). The second configuration is called cumulene, and it is depicted in Figure 1.2(b): theoretically, its BLA should be equal to zero. Cumulenic wires tend to be much stiffer than polyynic ones, as they hardly deviate from linearity due to the double bonds, which do not leave degrees of freedom like single bonds do [16].

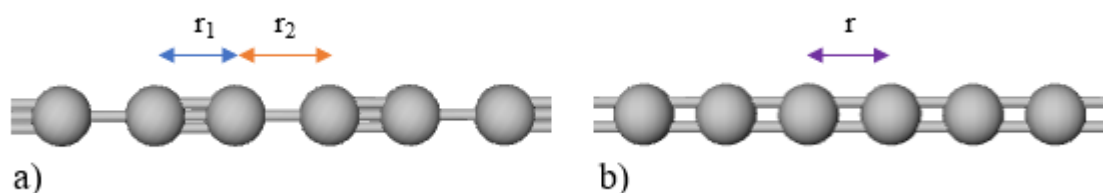


Figure 1.2 a) Schematic structure of a polyynes, with r_1 referred to the triple bond length and r_2 referred to the single bond length. b) Schematic structure of a cumulene, with equally long bonds.

These two structures are actually different in electrical character and stability, which are linked. Infinite carbyne has not been synthesised as of yet. However, finite segments of it have. By stabilising the structure with bulky end-groups, which protect the internal *sp*-carbon chain with their steric hindrance, polyynes up to 44 carbons have been synthesised [10], [26]. The longest cumulene that can be considered kinetically stable, on the other hand, is the [9]cumulene, where [9] refers to the number of double bonds [16].

The difference in their stability can be attributed to Peierls distortion, which affects 1D crystals with one atom per unit cell. The cumulenic unit cell has a one single carbon atom basis (indeed, cumulenes do not possess an optical phonon branch), as all carbon atoms are equally spaced one from another, while the polyynic unit cell basis includes two. The bond length alternation in polyynes leads to the doubling of the periodicity and so to the opening of an energy gap at the edge of the Brilluoin zone. This, in turn, causes a slight decrease in energy, thus more stability. In Figure 1.3, it is possible to see that, according to Peierls distortion alone, the cumulenic structure is highly unfavourable. Indeed, if it were only for this effect, cumulenes should not exist.

The reason why it is still possible to synthesise cumulenes sits in the fact that Peierls effect only becomes predominant above a chain length of 52 carbon atoms [27]. Below that value,

termination effects have control over the configuration. This also leads to the conclusion that, if ever a theoretically infinite carbyne could be synthesised, it would be a polyynes. Indeed, the long carbynes found inside CNT were polyynic [28].

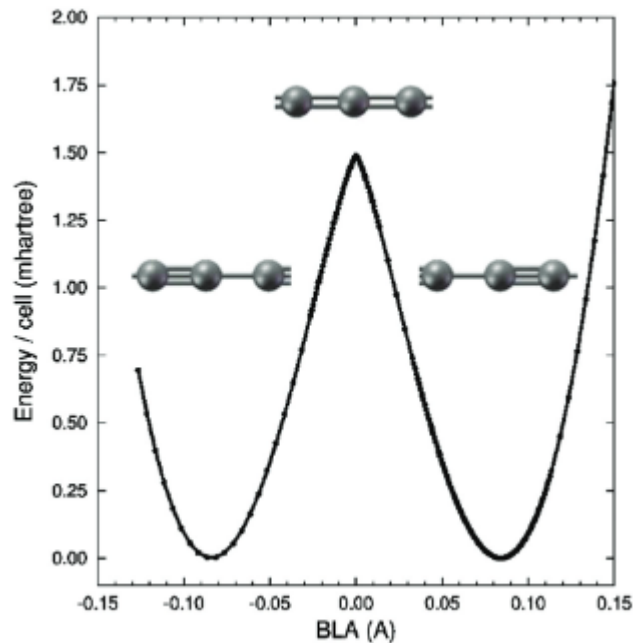


Figure 1.3 Structure energy in function of BLA, with a maximum in correspondence of the ideal cumulene, with $BLA = 0$ [15].

Stability aside, Peierls distortion effect influences the electrical behaviour of these materials as well.

The ideal cumulene does not display any gaps in its band structure. This is associated with metallic behaviour, as charges do not need to overcome a barrier to transition to another state. Indeed, it can also be proved through Huckel theory (linear combination of atomic orbitals, LCAO) that the energy gap is dependent on BLA [29].

Figure 1.4 displays the relation linking the band gap to the BLA. On top of that, the energy band gap also depends on the chain length, i.e. to the number of carbon. With cumulenes, it is actually common to count double bonds, instead of carbon atoms, since the π -conjugation length is what favours delocalisation of π -electrons, making conduction easier and shrinking the energy gap.

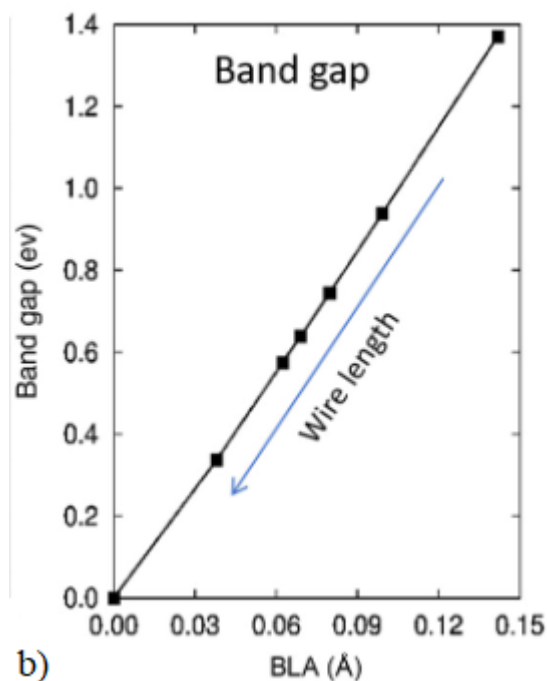


Figure 1.4 Energy band gap in function of BLA. A trend associated to wire length, so to the number of carbon atoms, is also shown [29].

In reality, a null BLA is impossible to achieve due to end-groups, so finite cumulenes are semiconductors, rather than conductors, but they are characterised by a smaller gap than polyynes, at set chain lengths.

On the other hand, polyynic energy gap implies a semiconducting or insulating behaviour.

In regard to single-molecule conductance, polyynes, due to their non negligible BLA, follow the relation linking the conductance to the length of the molecule through an exponential: $G \propto e^{-\beta L}$, where G is the conductance, β is the exponential attenuation factor (usually ranging between 0.2 \AA and 0.5 \AA), and L is the molecular length. This implies that longer molecules should be less conductive. Cumulenes, on the contrary, with their very small BLA, feature an attenuation coefficient equal to zero (meaning that the conductance is independent from the length) or less than zero, i.e. the conductance increases with the length [30].

Finally, within the family of cumulenes, it is necessary to distinguish odd-cumulenes, which have an odd number of quasi-double bonds, from even ones: they present a different arrangement of molecular orbitals, caused by mesomeric or inductive effects coming from end-groups.

Even cumulenes are characterised by two degenerate, orthogonal to each other, π -systems, each of which can conjugate with the terminations on one end only. In Figure 1.5(a), it is possible to

observe an example of even tetraphenyl-substituted cumulene (Tetraphenylpentatetraene, [4]Ph).

Odd cumulenes display two non-degenerate π -systems. One of them is extended along the cumulenic core and to both terminations, while the other is confined to the *sp*-chain (Figure 1.5(b) depict the case of [5]Ph). This actually leads to an increase of the BLA in odd cumulenes, due to end-groups effects [16]. Nevertheless, even cumulenes are considered less conductive [30], due to the shorter conjugation.

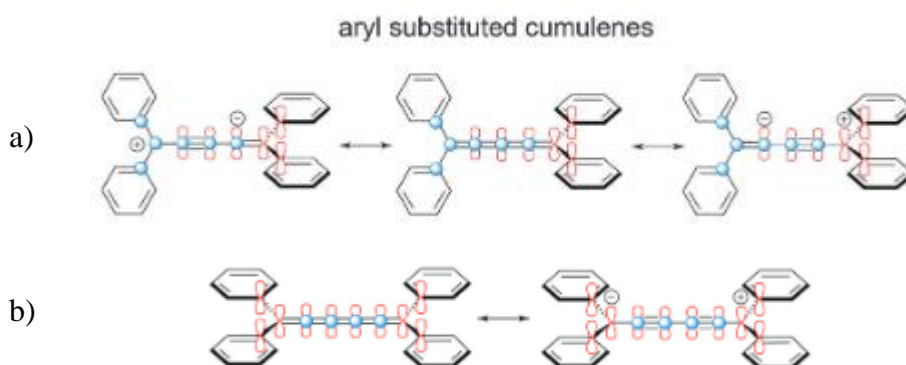


Figure 1.5 a) π -systems of even aryl-substituted cumulenes. b) π -systems of odd aryl-substituted cumulenes [16].

Furthermore, odd cumulenes are considered easier to synthesise, hence their wider diffusion with respect to even cumulenes [7].

1.3 Tuneability

Finite *sp*-carbon molecules are highly tuneable [15].

By controlling their length, as explained in the previous section, it is possible to control BLA and energy gap, which in turn influences the electrical properties. Engineering the chain length is not the easiest task, however, as the longest the *sp*-chain gets, the more unstable it becomes. Indeed, bulky groups do not seem to be able to allow for growing cumulenes longer than [9]cumulenes. Other stabilisation strategies should be considered, such as stabilisation by rotaxanes, as depicted in Figure 1.6.

Not only that, but the terminal groups play a pivotal role in shaping the molecule. It has been already said that bulky ones are chosen to stabilise *sp*-chains. In fact, they can force either a cumulenic or polyynic character onto it, too. Di-phenyl substituents are known to induce a cumulenic character onto the chain [16], [31].

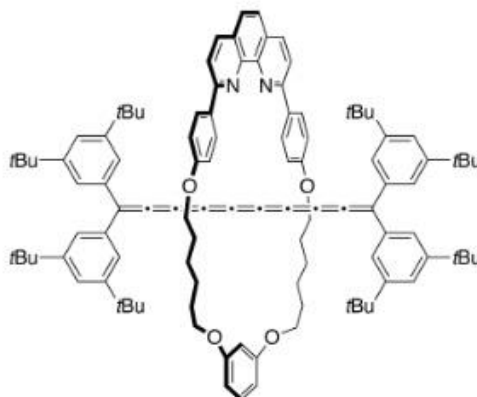


Figure 1.6 [9]cumulene stabilised by bulky end groups and a rotaxane molecule [32].

Terminations also have an effect on BLA, and this is why finite cumulenes cannot have a null BLA, although it can be very small (below 0.02 \AA). Indeed, the closest double bonds to the end groups are consistently the longest [16].

sp^2 -based end-groups, such as phenyls, can also extend the π -conjugation.

Other effects can have an influence over those molecules. For example, strains induced in the linear chain can affect the Raman signal of these molecules [33]. This is associated to an alteration in vibrational properties and very possibly to electronic transitions as well, since it is common for conjugated molecules to show coupling of π -electrons and vibrations [34].

2. ORGANIC FIELD EFFECT TRANSISTORS

2.1 Working principle of OFETs

Organic field effect transistors are three-electrode devices, and they are considered the organic counterpart of metal-oxide-semiconductor FET (MOSFET), as the two architectures share some similarities. First of all, they both exploit the field effect to modulate the conductivity of the active layer: through the application of a voltage at the gate electrode (V_G), the charge carrier density can be altered, i.e. increased, so that the current, flowing between the electrodes source and drain upon the application of a bias between them (V_D), is effectively controlled by the bias at the third electrode.

Figure 2.1 depicts the structure of an OFET, which is composed of three main items: conductive electrodes, an insulating layer and an active layer. Those components can be arranged in 4 different configurations, but more on this later on.

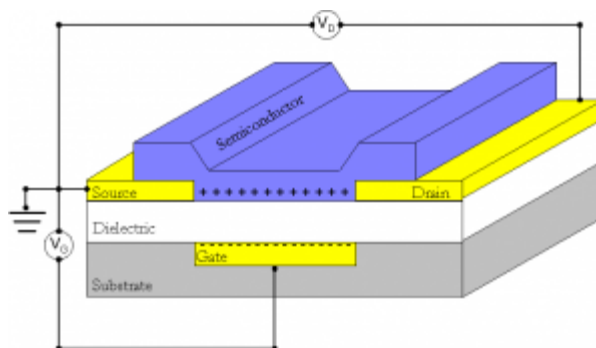


Figure 2.1 Schematic representation of the structure of an OFET.

One main difference between OFETs and MOSFETs is the regime they typically work in. While MOSFETs can operate both in depletion and accumulation mode [35], OFETs only work in accumulation regime.

In a p-type OFETs, a negative gate voltage is applied in order to accumulate positive charges (often referred to as “holes” for simplicity) at the dielectric-semiconductor interface: a thin accumulation layer of majority carriers is formed, leading to an increased charge carrier density. Similarly, in n-type OFETs, the application of a positive gate voltage results in the accumulation of negative charges (electrons). In this way, the gate voltage modulates the conductivity of the active layer through the field effect. When a voltage is applied between source and drain, a current can flow through the channel, i.e. the dielectric-semiconductor interface. Therefore, a smooth, conformal interface is crucial.

It should be pointed out that in MOSFETs the regions beneath source and drain are typically made of highly doped semiconductors (usually silicon), while in OFETs there is no need for that, as pristine organic semiconductors are characterised by a low conductivity that keeps the off current, i.e. the current flowing when the device is turned off, very low.

Before moving on to the analysis of OFETs working regimes, it should be noted that some ideality conditions should be satisfied, in order to apply the same equations employed to characterise MOSFETs [36].

- Field effect mobility should be independent from the applied voltage after a certain threshold, V_{th} , defined as the bias needed to have current flowing from source to drain (it is negative for p-types and positive for n-types). Moreover, the mobility should be constant throughout the channel.

Field effect mobility is mathematically expressed as $\mu = \frac{e \cdot D}{k_B \cdot T} = \frac{v}{E}$, where e is the elementary charge, D is the diffusion coefficient of the material, k_B is the Boltzmann constant and T is the temperature, v is the drift velocity of the charge carrier and E is the electrical field. Thus, mobility is associated with the velocity of charge carriers within a material and is linked to the current.

- Contact resistance should be negligible. This rarely happens in OFETs, but the subject will be dealt with in detail later on.
- Charge transfer should not be hindered by traps across the channel. This is also in question when it comes to organic semiconductors (OSCs). More on this later on.
- The transverse electrical field should be much larger than the longitudinal one.

In addition to that, an ideal OFET should not display dual switching on, hysteresis (which will be explained later), and linear mobility should be equal to saturation mobility. Linear and saturation regimes will be explained in a moment.

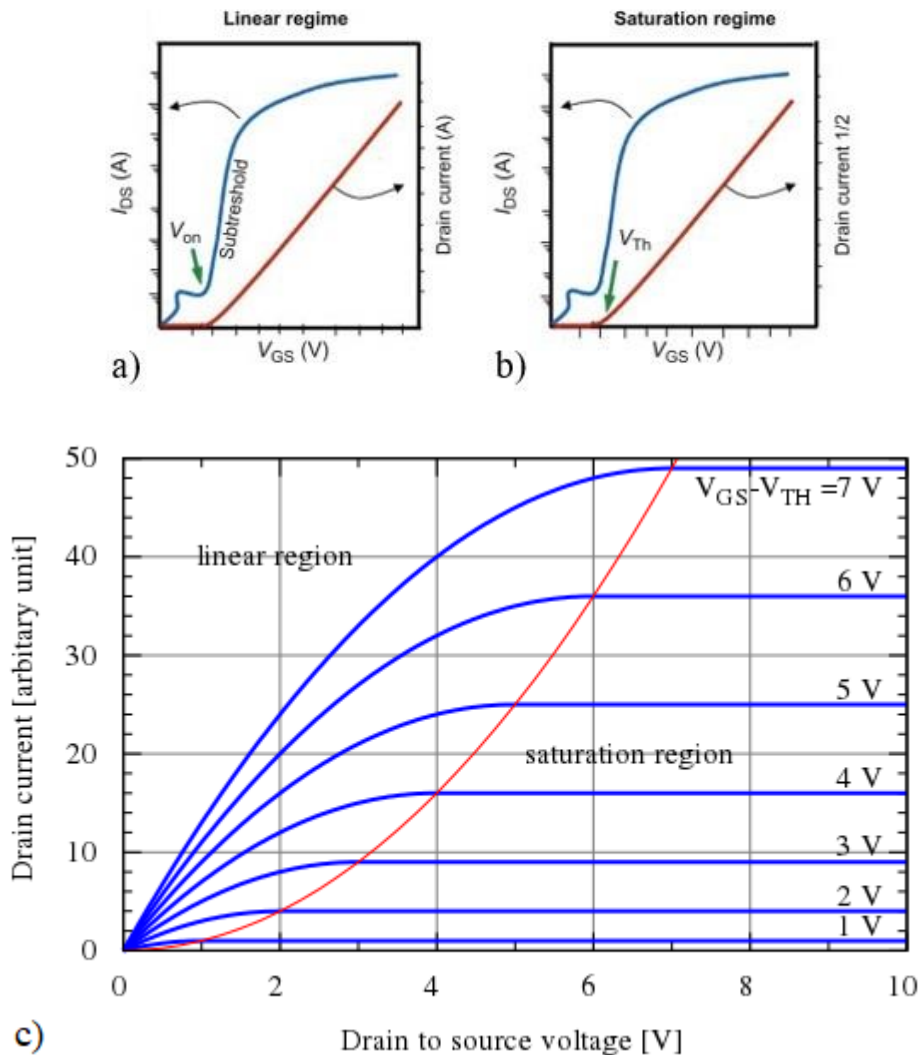


Figure 2.2 Transfer curves of an ideal OFET in **a)** linear regime and **b)** saturation regime, with the current in logarithmic scale. **c)** Output curve of an ideal OFET.

Figure 2.2(a) is the characteristic transfer curve of an OFET in linear regime: drain voltage is kept fixed at a relatively low value, while voltage gate is varied continuously, and the source-drain current is measured. When the voltage gate reaches the above defined threshold, the current reaches a plateau. We can observe the linear regime also in Figure 2.2(c), in the first part of the characteristic output curve. An output curve is obtained by keeping fixed the voltage gate and varying the drain one. It is possible to see that at the beginning the relation between drain voltage and current is linear, meaning that the semiconductor channel almost acts as an ohmic resistor: this is the linear regime. By increasing the voltage gate by discrete steps, the slope increases, as it is inversely proportional to resistance, i.e. it is proportional to conductivity, which relies on the gate bias. Sometimes, in the linear regime of an output curve, the relation is not perfectly linear, instead an “S” shape is present: that is an indication of charge injection

issues, and it is a deviation from ideality. Figure 2.2(b) is the transfer curve of an OFET in saturation regime: drain voltage is now higher. In the output curve, as the drain voltage increases, the voltage drop in the dielectric decreases, and so does the charge density. This leads to a saturation and the current reaches a plateau: this point is called pinch-off. After that point, the current is no longer dependent on the drain voltage, but it is still quadratically dependent on the gate voltage: this is the saturation regime.

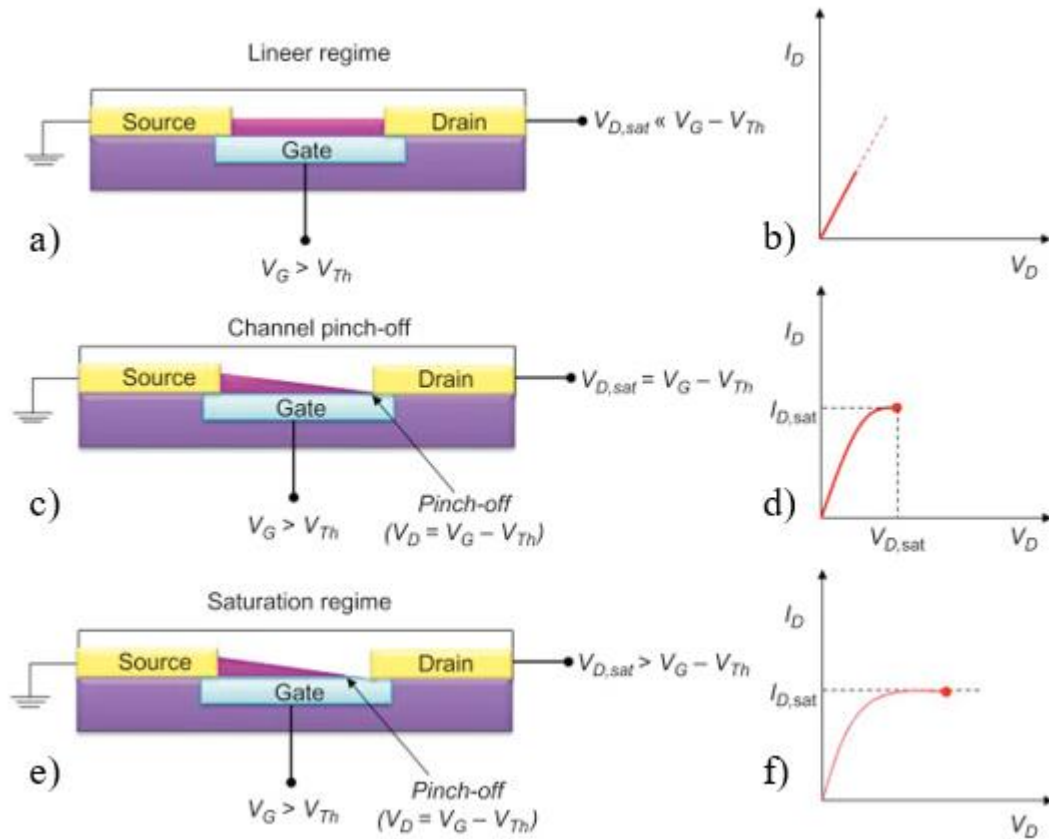


Figure 2.3 a) – b) are respectively the schematic representation and the output curve of the linear regime. c) – d) represent the pinch-off point. e) – f) are referred to the saturation regime.

Figures 2.3(a)-(f) sum up the stages a OFET goes through while functioning, both with a schematical representation of the channel and with the output curve, step by step.

It should be underlined that the mobility extracted from this graph is not the intrinsic mobility of the material. Rather, it refers to the whole device.

The same holds true for the threshold voltage, which is heavily influenced by charge injection and contact resistance.

In general, film defects, de-wetting problems, contact resistance, etc, affect the overall performance of the device, and so extrinsic factors should always be taken into account.

2.2 OFET architectures

As mentioned above, the components of these devices can be geometrically arranged in different ways. In particular, there are 4 configurations that can be adopted to fabricate a transistor of this kind, each with peculiar characteristics [3].

- Top-gate top-contact: the semiconductor is the first layer deposited on the substrate, then source and drain are deposited on top of it. Dielectric deposition follows and the gate deposition is the last step. The drawback of this configuration is the necessity to deposit the source and drain contacts on top of the semiconductor: this can lead to degradation of the active layer, as those electrodes are often metals, requiring elevated temperatures to deposit. Additionally, this coplanar architecture (in regard to source, drain and conductive channel disposition and as opposed to the staggered one) is known to lead to charge injection issues, due to geometrical reasons: the injection surface is smaller [37].
- Top-gate bottom-contact: source and drain are deposited first, then the semiconductor, the dielectric and finally the gate. This is a commonly picked configuration, since it does not involve significant risks for the active layer, as the dielectric materials is often a polymer, which can typically be processed at room temperatures. Besides, the dielectric on top of the semiconductor protects it from the external environment.
- Bottom-gate top-contact: the gate is deposited first, then the dielectric, the semiconductor, and source and drain. This configuration involves depositing the electrodes on top of the active layer.
- Bottom-gate bottom-contact: the order is gate, dielectric, electrodes, semiconductor. It is usually picked to study new semiconducting materials, often in controlled, nitrogen atmosphere, as nothing is deposited on top of it. This can be detrimental as well, though, if the semiconductor is particularly unstable. Besides, this coplanar architecture shows charge injection issues, too.

Figures 2.4 (a)-(d) represent the 4 possible configurations for OFETs.

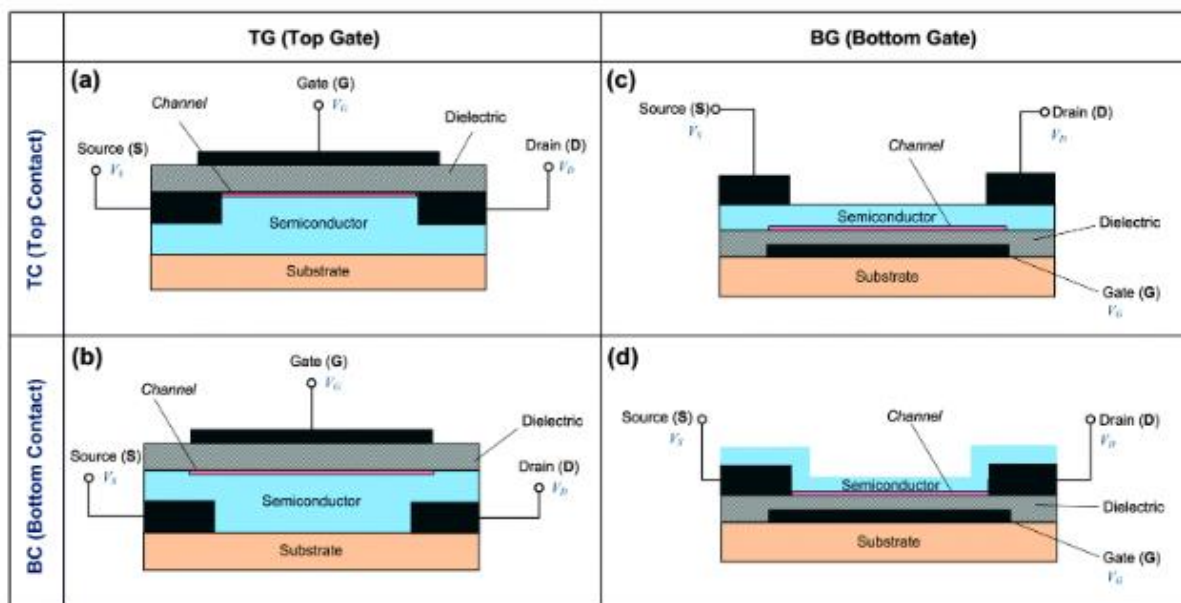


Figure 2.4 Schematic representations of devices in configurations: a) TGTC; b) TGBC; c) BGTC; d) BGBC.

2.3 Active layer in OFETs

A major difference between MOSFETs and OFETs sits in the electrical properties of the semiconductors employed in the respective active layers. They differ both in the intrinsic properties and in the processes that they undergo. For example, OSCs are often deposited in thin film either from solution or by chemical vapour deposition.

For the most part, organic semiconductors can be divided into polymers and small molecules.

Polymers feature a very easy processability by several techniques (ink-jet printing, spin coating, bar and blade coating, chemical vapour deposition, etc), in conjunction with a large variety of molecules and optimal mechanical properties, flexibility above any other. Indeed, polymers are crucial for the development of flexible electronics. The downside of using semiconducting polymers has to do with their poor mobility (up to 10^0 cm^2/Vs), as they are notoriously prone to disorder and low crystallinity, due to kinetics reasons. A few examples of this category of OSCs are N2200, P3HT and polythiophenes. In general, they are based on aromatic rings and thiophenes, which rely on sp^2 carbon to promote π -conjugation [38].

The second kind of OSCs is the category of small molecules, which the semiconductors studied in this thesis work belongs in. They have a much higher tendency to crystallise, with respect to polymers, as they are characterised by a lower degree of disorder. They are typically based on sp^2 -carbon, so aromatic rings, but sp -carbon based ones are gradually catching the attention of researchers. They can be functionalised to improve solubility and other properties, or to force

them into planarity. One of the most employed semiconducting small molecules is pentacene, which has been proved to reach mobilities of the order of magnitude of $10^1 \text{ cm}^2/\text{Vs}$, with an on-off current ratio of 10^6 . The drawback of this lies in the fact that those molecules are considerably harder to bring to film [38].

There is a third route, when it comes to OSCs, and it involves blending two or more components to exploit the characteristics of all of them.

For example, it is a common strategy to blend small molecules with polymers. The idea is that of combining the easy processability of polymers, with the higher conductivity of small molecules [4].

Either semiconducting or insulating polymers can be used. In the former case, the polymer actively participates in the charge transport, leading to the enhancement of the electrical performance of the blend. The drawback is related to the difficulty in telling apart the contribution to mobility of each component.

On the opposite, resorting to insulating polymers does not hinder the study of the small molecule, since insulating polymers, by definition, do not conduct current, meaning that they do not directly contribute to charge transport

Thanks to their easier processability from solution with respect to small molecules, insulating polymers can act as an amorphous binder for the studied small molecule and help in achieving a good coverage all over the sample. Furthermore, through a phase separation mechanism occurring during the film formation [39] this strategy allows to better control the small molecule crystallization and consequently obtaining films with better charge transport properties.

Finally, the insulating polymers can provide the small molecule layer with a partial self-encapsulation from oxygen permeation and humidity.

When blending polymers and small molecules, phase separation can take place. If on the one hand, the vertical phase separation can improve the charge transport performance of the semiconducting film, on the other hand, this phenomenon can lead to unpredictable drawbacks. Indeed, it is specifically dependent on the blend components and on their ratio, hence difficult to predict and control. For example, in bottom-contact devices like the ones fabricated in this thesis work, if the polymer preferentially segregates at the bottom interface, charge injection between the conductive contacts and the semiconducting layer will be severely hindered. Vertical phase separation might also be incomplete due to kinetics, likely leading to the embedding of small molecule crystallites in a polymeric matrix: in this case, there will not be percolation paths for charges between source and drain.

Many factors should be taken into account when formulating a blend, namely, chemical composition of the components and their relative amounts, the average molecular weight of the polymer, the solubility of the components in the solvent, crystallisation kinetics, the solvent surface tension, evaporation rate, deposition conditions, etc [4], [39]. The molecular weight of the polymer is particularly important. Due to thermodynamic reasons, a high average molecular weight is linked to an increased tendency toward phase separation, as it results in a positive mixing Gibbs energy variation, according to Flory-Huggins equation [40]. Furthermore, a higher molecular weight leads to better mechanical properties, in particular an improved plasticity with respect to brittleness, as well as to an increased viscosity, which is a crucial parameter for certain deposition techniques. For example, screen printing requires a high molecular weight, while spin coating works better on low viscosity solutions [39].

2.3.1 Doping organic semiconductors

Inorganic semiconductor doping involves the intentional insertion of impurities, in a controlled amount, into the material, in order to modify the conductivity as needed. For organic semiconductors, the doping involves a charge transfer between two molecules, a donor and an acceptor, so a reduction-oxidation reaction, which can be either reversible or not, according to the doping technique employed. Electrochemical, photo and charge injection doping procedures are reversible, while chemical doping is not. Particularly relevant is the charge injection doping, which is a reversible process that does not involve counter ions or other external substances, thus distortions are reduced. It is carried out by applying a voltage, so this form of self-doping can very well happen spontaneously, while the semiconductor is in active state in a transistor.

P-type materials act as oxidised donors, while n-types undergo reduction. Just like inorganic doping, the goal is to increase the conductivity of the pristine material.

It is important to underline that, in general, organic semiconductor are considered ambivalent. However, they do show a tendency either to be p-doped or n-doped. This has to do with their molecular orbital levels. P-types are those materials displaying a deep highest occupied molecular orbital (HOMO), while n-types have a low lowest occupied molecular orbital (LUMO).

2.3.2 Charge transport in organic semiconductors

In order to effectively study the charge transport properties of OSCs, it is essential to understand the mechanisms behind it.

In recent times, a new theory, the transient localisation, has been proposed to explain the conduction phenomena of OSCs, replacing the old one involving charge hopping from one

molecule to the other. The new theory allows to explain the experimental data compliant with a band-like behaviour, as well as those that cannot be explained by a semiclassical description [41].

The old Marcus theory supports the fact that charge carriers, generated in organic molecules by doping and partially self-trapped by the distortions around them, can move with greater speed and ease along the conjugated molecule (intrachain), but that can make an interchain jump from one molecule to the other upon thermal stimulation, carrying out a reduction-oxidation reaction between two molecules. These motions are always associated to distortions, as the donor molecule relaxes, with a relaxation energy linked to polaron binding energy, and the acceptor one needs to accommodate the new charge, leading to a strong electron-vibration coupling [42], [43].

This theory presents an issue: calculations revealed that it cannot explain polaron localisation [44]. Moreover, small polaron theory does not work, either, as *ad hoc* regularisations are needed to make calculations compliant to evidence [45].

As for the semiclassical Bloch-Boltzmann theory, it does not apply either. Bloch-Boltzmann description of charge transport relies on the concept of Bloch states, which are plane waves modulated by a periodic function, which describe particles moving in a perfectly periodic potential, such as an ordered crystal. Well defined wave packets only encounter scattering rarely, but this cannot apply to more disordered, more thermally active molecules.

Poor conductors like OSCs present a disruption of the Bloch-Boltzmann theory, since the lack of high-degree order, and especially the thermal molecular motions cause the carriers to scatter. After a scatter event, loss of coherence takes place, significantly reducing the carriers' mean free path. The wave function associated to the carriers ends up localised: mathematically, the envelope function, which acts as a modulator for the wave function itself, decays exponentially [46], as depicted by Figure 2.5. This is called Anderson localisation and it can be defined as the incapability for waves to propagate in a disordered medium [47].

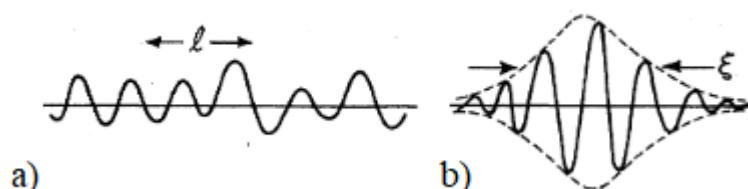


Figure 2.5 a) Wave function of an extended state, l being the mean free path. b) Localised state, showing the wave function (solid line) decaying to zero assisted by the envelope function (dotted line) [46].

Thermal molecular motions are so large in OSCs because the molecules are held together by weak Van der Waals forces, that only provide a weak restoring force to the distortions. Combined with the important masses of typical organic molecules, this leads to extremely slow motions, so that the carriers feel a significant disorder around them at any given instant [45].

As slow as these motions are, the lattice is still dynamic, meaning that the static Anderson localisation is too restrictive to actually describe this phenomenon.

To accommodate for the dynamicity of these systems, a time relaxation approximation is applied to consider the inelastic scattering events, due to low frequency phonons.

Experimental data, acquired on crystalline rubrene, actually proved the transient localisation for time scales included between the characteristic elastic scattering time, below which quantum ballistic regime is established, and a characteristic time associated to the molecular vibration [41]. Figure 2.6 shows the trend of carriers' diffusion in function of time scale.

Transient localisation theory explains why even highly crystallised OSCs show a mobility of $10 \text{ cm}^2/\text{Vs}$, while inorganic semiconductors can reach even $10^7 \text{ cm}^2/\text{Vs}$ in heterostructures [45]. Such a low carrier mobility is due to very short mean free paths.

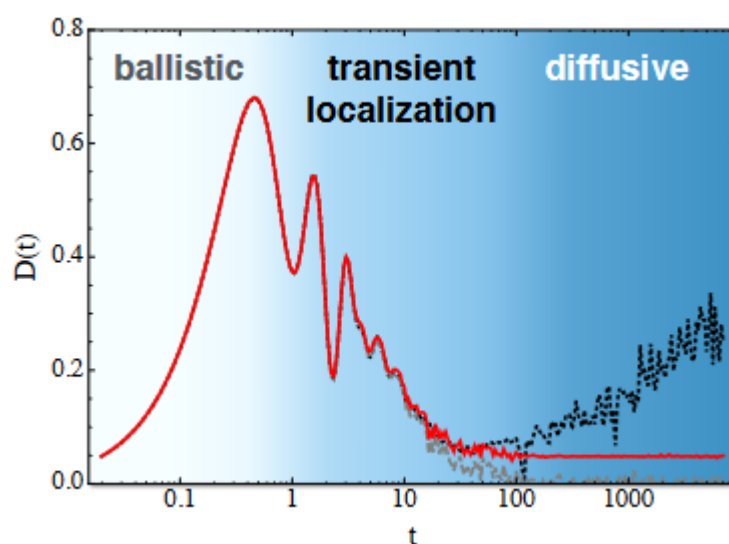


Figure 2.6 Time scale against charge carrier diffusion [45].

The localisation of the wave function only lasts as long as the typical time scale of the molecular vibration, meaning that at much longer times the behaviour of the carriers goes back to being itinerant (diffusive).

Aside from low mobility values, the transient localisation theory can explain a large variety of phenomena.

For example, in pure samples at high temperature, where structural disorder is not too relevant, the mobility trend follows a power law relation exactly like organic semiconductors do, and yet the mean free path is equal or even shorter than the typical intermolecular spacing, in open contrast with Bloch-Boltzmann theory [45].

Moreover, the Seebeck coefficient of OSCs is comparable to that of inorganic ones, suggesting some form of band-like behaviour [48].

Next, photoemission spectra confirmed the existence of a coupling between the intra-molecular vibrations and the molecular orbitals, but this interaction does not narrow the electronic bands as expected from polaron theory [49].

A further confirm to this theory comes from diffraction experiments, which have detected very active thermal molecular motion [50]. Electron Spin Resonance (ESR) measurements support the finite extension of the carriers' wavefunction [51], while Charge Modulated Spectroscopy (CMS) confirms finite localisation length [52].

It is possible to conclude that transient localisation is a solid theory, which can explain charge carriers' behaviour inside OSCs better than the band-like model and the Marcus theory about hopping.

2.4 Charge injection

When dealing with charge injection, it is about source and drain injecting and collecting charges into and from the active layer. Charge injection issues can easily reduce the performance of the device, even if the semiconductor is perfectly crystallised in a good film.

The mechanisms by which charge injection occurs are the following: thermionic emission, through which charges overcome an energy barrier thanks to thermal excitation, defect-assisted injection, in which mid-gap states are created due to defects and those help overcoming the barrier, and finally field emission, which relies on tunnelling. It should be noted that thermionic and field emission can be active together [37].

In order to have good injection, it is essential that the electrode material, often metal, and the semiconductor are compatible from an energetic level point of view.

For p-types, the work function, i.e. the difference between its Fermi level and the vacuum level, of the chosen metal should be close to the HOMO of the semiconductor, which is related to the ionisation potential of the OSC. For n-types, the work function of the metal should be comparable with the LUMO, linked to the electron affinity of the material.

There are situations, though, where the work function of the metal can be altered. It should be always remembered that the work function is a surface property. Thus, any change to the surface can lead to oscillation in the energetic structure. Passivation of the metal, especially in solution, can affect its charge injection efficiency. On top of that, phenomena of physisorption or chemisorption (weak or strong) can also alter the metal work function. For example, if the OSC is physisorbed at surface, the π -cloud can push the tail of the electron charge density back, lowering the work function [37].

Other causes of charge injection issues are related to the semiconductor: relaxed polaronic states and defects can act as traps can hinder the performance of the whole device. Positional disorder is also a factor, and the HOMO and the LUMO can follow a Gaussian distribution, with a width of 0.1 eV [37].

Furthermore, the device configuration plays a role in charge injection, too. As already mentioned, coplanar architectures (TGTC and BGBC) offer a smaller surface to the semiconducting layer, so there is a smaller surface to engage in charge injection, with respect to staggered architectures (TGBC and BGTC).

Solutions to overcome charge injection issues include the application of self-assembled monolayers, which can alter the semiconductor-electrode interface both topologically and energetically, and swap of device configuration and/or electrode material.

2.5 Hysteresis

Transfer hysteresis is encountered when the detected currents from the forward and reverse sweep do not comply with each other. In other words, either the forward or the backward sweep gives back a higher current than the other, as depicted in figure 2.5(a)-(b).

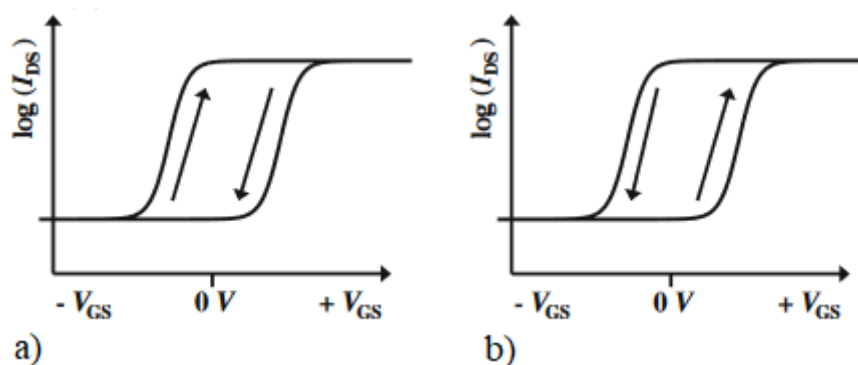


Figure 2.7 Transfer curves showing a) lower back sweep current (BSC) hysteresis, and b) higher BSC hysteresis [53].

Hysteresis can be due to three main reasons.

- A. Phenomena related to the semiconductor channel, divided into: majority or minority charges trapped in the proximity of the semiconductor-dielectric interface (A1); charges flowing from the semiconductor into the dielectric (A2); ions and polarons moving in the semiconductor, preventing other charges to access the channel (A3). Those effects deplete the channel from charges and result in a lower current in the back sweep.
- B. Phenomena regarding the dielectric layer, divided into: residual (quasi) ferroelectric polarisation of the dielectric inducing an electric field on charges aside from the voltage one (B1); ions moving in the dielectric (B2). Those effects cause the accumulation of excess charges at the interface, compensating the decreased potential in the back sweep and producing a higher BSC hysteresis.
- C. Charge injected into the dielectric from the gate: this effect also results in a higher BSC hysteresis [53].

Those mechanisms can be observed in figure 2.6.

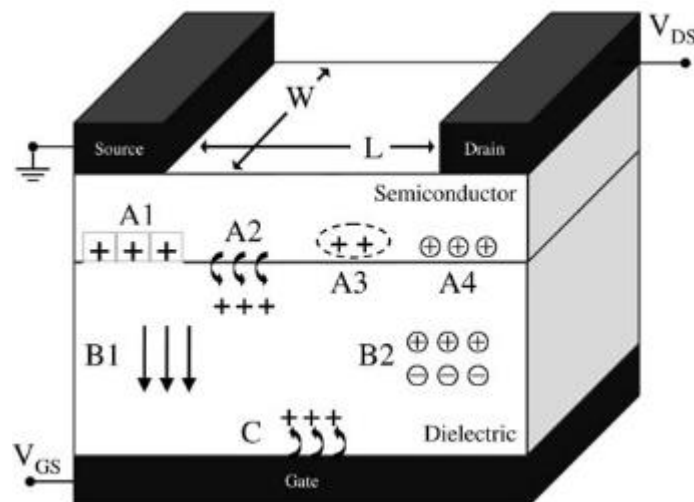


Figure 2.8 Schematic representation of the phenomena leading to BSC hysteresis [53].

Bias stress can aggravate the deviations from ideality of the transfer curve in the back sweep or switching from linear to saturation regime [54].

In order to reduce hysteresis, a few solutions are proposed: smooth semiconductor-dielectric interface decrease the number of traps [6]; low dielectric constant insulators also decrease the occurrence of hysteresis, and they also reduce threshold voltage and increase mobility [55]; the

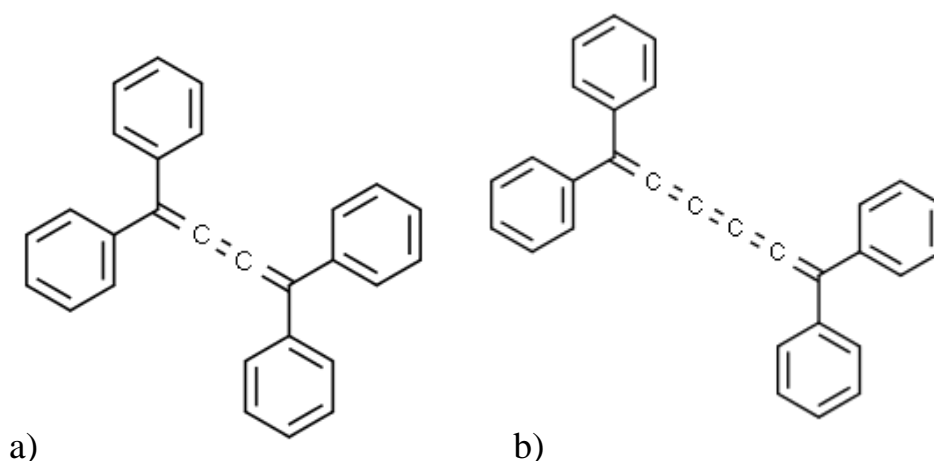
application of SAMs and dielectric materials with no OH groups can also help lowering the incidence of traps [53].

3. MATERIALS AND METHODS

3.1 Materials

3.1.1 Active layer

The active layers of the transistors studied in this thesis work are based on two organic semiconductors, namely the cumulenenic small molecules Tetraphenylbutatriene (henceforth referred to as [3]Ph, from the phenyl end-groups and the three double bonds building the central backbone) and Tetraphenylhexapentaene ([5]Ph), differing from [3]Ph for a longer central chain, made of 6 carbon atoms, instead of 4, bonded through 5 quasi-double bonds. This longer conjugation narrows down [5]Ph energy gap, and it red-shifts its absorption spectrum with respect to [3]Ph, as it will be shown in Paragraph 4.2.1. Indeed, [5]Ph is red in colour, while [3]Ph is yellow. The two molecules are depicted in Figure 3.1(a)-(d), both in 2D and in 3D.



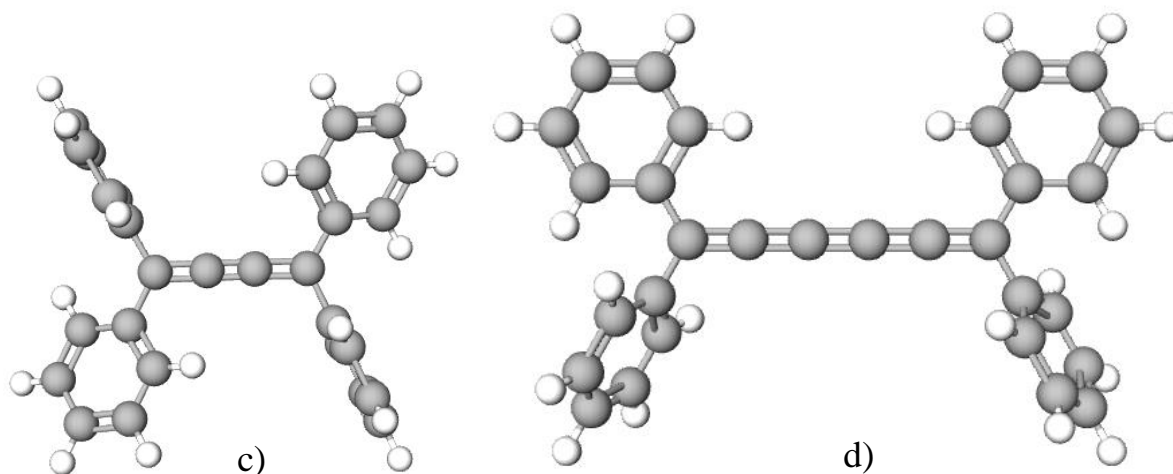


Figure 3.1 a) 2D structure of [3]Ph. b) 2D structure of [5]Ph. c) 3D structure of [3]Ph. d) 3D structure of [5]Ph.

Both [3]Ph and [5]Ph were synthesised by Prof. Rik Tykwinski and his team (University of Alberta); in particular, [5]Ph, main focus of this thesis work, was synthesised via oxidative homocoupling of a precursor, leading to the formation of a diyne diol as an intermediate product, and then to the final molecule, as shown in Figure 3.2 [7].



Figure 3.2 [5]Ph synthesis, carried out by Rik Tykwinski and his team; “Ar” represents phenyl groups [7].

The reasoning behind the choice of these two particular molecules from the families of [3]cumulenes and [5]cumulenes has to do with their stability in solid state in ambient conditions. For example, [5]Me, which is just as long as [5]Ph in terms of *sp*-chain, is highly reactive [16].

[3]Ph and [5]Ph are both stable in air at room temperature, when kept protected from light, and can be stored in fridge (at 4 °C) for months. Furthermore, they are stable and processable in common organic solvents, such as 1,2-Dichlorobenzene (1,2-DCB).

The decreased instability with respect to other equally long cumulenic molecules is due to the bulky end groups, i.e. the four phenyl groups: with their steric hindrance, they protect the central chain by preventing intermolecular interactions. By keeping the *sp*-carbon chain isolated, reactions of cycloaddition become less likely to happen.

A correlated effect of the steric hindrance of the phenyl groups is the slight distortion from planarity they enforce onto both [3]Ph and [5]Ph, which do not lie perfectly flat on a plane. The

extreme rigidity of their central cumulenic chains, constituted by double bonds, keeps the backbone almost perfectly linear, but the single bonds connecting the end groups to the *sp*-carbons allow rotations to accommodate the phenyls. This distortion might affect the properties of the molecules in many ways, but a crucial one is the packing in solid state. The specific arrangement of the molecules will not be discussed in this thesis work, but there is ongoing research studying the packing of both molecules in bulk and in thin films, since it is crucial to determine their electrical behaviour. Moreover, the aromaticity of the phenyl groups extend the conjugation of [3]Ph and [5]Ph.

In 2020, the first field effect transistor based on *sp*-carbon wires was fabricated by employing dropcasted [3]Ph as active layer in a BGBC device [12]. Since then, [3]Ph has been further optimised and thin film transistors showing mobilities up to 10^{-1} cm²/Vs have been obtained [13].

[5]Ph is less known, especially in regard to applications. At the beginning of this thesis work, only one attempt had been made at fabricating transistors based on this molecule [56], but it is catching the attention of researchers due to its potential properties.

Since its cumulenic chain is longer than that of [3]Ph, it is a more conjugated molecule, with a BLA of 0,058 ([3]Ph BLA is 0,088 [7]) and a smaller energy gap between its HOMO and LUMO. This suggests that, once optimised, it might be better at transporting charges, profiting from the higher intra-chain charge delocalisation. However, molecular packing motifs in solid-state are crucial to reach high charge mobility in organic semiconductors thin film [57]. Since predictions on the impact of the *sp*-chain length on the molecular packing have not been reported yet, it is *a priori* impossible to predict if [5]Ph will ultimately perform better than [3]Ph in OFETs. Finally, the stability of these systems is usually decreasing with increasing *sp*-chain length. In fact, the longer the cumulenic chain, the harder it is for the bulky end groups to prevent intermolecular interactions, leading to possible stability issues [7]. It should be pointed out that, even though [3]Ph and [5]Ph are stable when compared to longer cumulenes, stability issues are still a concern. In particular, both molecules show severe photosensitivity, which can hinder their performance in OFETs if this issue is not properly faced along all the fabrication process. Chapter 5 will focus specifically on [3]Ph and [5]Ph stability.

Finally, it is interesting to point out that from a single-molecule standpoint, it has been calculated that [3]Ph and [5]Ph have the same conductance – as explained in Section 1.2, cumulenes tend to have a single molecule conductance independent from the molecular length [30].

Blends with insulating polymers

As already stated in Section 2.3, a common strategy to optimise small molecule thin films in terms of structure-property relationship consists in blending them with insulating polymers [4], [38], [39].

In this thesis work, Polystyrene (PS) and Poly(methyl methacrylate) (PMMA) were both tested in blends with [5]Ph. [3]Ph:PS blends had already proved effective in OFETs [58], although its performance is lower than the one obtained with optimised pristine [3]Ph films. It is therefore interesting to further investigate and optimise the deposition of both [3]Ph and [5]Ph with PS and PMMA. Both polymers undergo glass transition around 110 °C, and both are soluble in 1,2-DCB.

PS was purchased by Sigma-Aldrich in atactic formulation, with average molecular weight of 2 000 000 g/mol. Its repeat unit can be observed in Figure 3.3(a). PMMA, shown in figure 3.3(b), was also purchased from Sigma-Aldrich and had an average molecular weight of 120 000 g/mol.

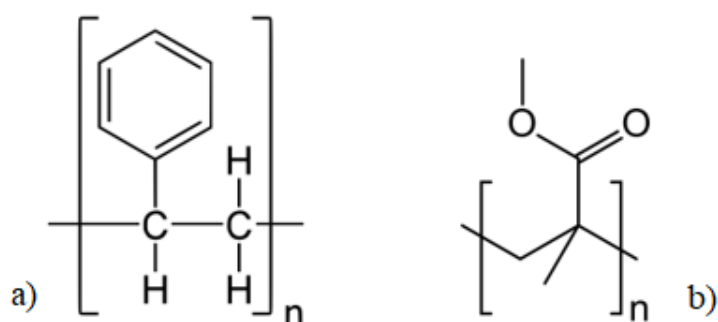


Figure 3.3 a) Polystyrene repeat unit. b) Poly(methyl methacrylate) repeat unit.

3.2 Device fabrication

Except for screening tests of solutions dropcasted onto prefabricated Fraunhofer substrates (which will be described shortly), the complete transistors structure was entirely fabricated from scratch, according to either TGBC or BGBC configurations. The detailed description of each step follows.

3.2.1 Source and drain deposition

The deposition technique of choice for source and drain interdigitated electrodes was thermal evaporation of high purity gold on top of lithographies. Gold was selected because of its high conductivity, its resistance to oxidation and most chemical attacks, and, above all, it is

compatible with [3]Ph and [5]Ph in terms of energetic levels, so that gold contacts can establish decent charge injection to the semiconductor HOMO level. Indeed, the gold work function is approximately equal to 5.1 eV (with small variations reported in literature depending on the surface treatment), while [3]Ph and [5]Ph HOMO levels are of -5.3 eV and -5.4 eV, respectively.

TGBC photolithography

The whole procedure is carried out in an ISO 6 Cleanroom.

The first step in the photolithography process is the cleaning of the glass substrates (low alkali 1737F Corning glasses), which is accomplished through a 10-minute-long sonic bath (50 Hz, 40 °C) in acetone, followed by a 5-minute-long sonic bath in isopropyl alcohol (IPA) with the same settings for frequency and temperature, and then by a drying step under nitrogen flow. Both solvents were purchased from Sigma-Aldrich.

Then, the substrate undergoes a further cleaning step in a plasma asher (PVA TEPLA 300 AL), in oxygen for 5 minutes at 500 W. Done that, it is time for the deposition of the resists. Two resists, Microresist LOR (Lift-Off Resist) 5B and Microposit “S1813” G2 (a novolak based positive photoresist), are employed to get a suitable structure, that not only allows for the precise deposition of the metal contacts, but that also favours the lift-off of the resists themselves during the stripping process. This will be thoroughly explained later on.

Both resists are spin coated (Spin Coater - Sawatec SM-150) on the clean and activated glass surface following the same recipe: the first step (velocity = 1000 rpm, acceleration = 500 rpm/s, duration = 10 s) roughly spreads the liquid resist all over the surface, the second one (velocity = 4000 rpm, acceleration = 4000 rpm/s, duration = 60 s) determines the thickness of the layer, and the last one (velocity = 6000 rpm, acceleration = 6000 rpm/s, duration = 5 s) helps getting rid of any edge defects, such as the thickening of the film. First, a 450 nm thick LOR 5B film is spin coated and is annealed at 180 °C for 7 minutes right away. Then, S1813 is spin coated to a thickness of about 1200 nm on top of the LOR layer (Figure 3.5(a)). The annealing is carried out at 120 °C for 2 minutes.

Next, a patterned mask is mounted on the mask aligner (Karl Süss MJB3). In this thesis work, two different patterns were employed: the first one, shown in figure Figure 3.4(a), is a reproduction of the source and drain patterns on the substrates produced by Fraunhofer IPMS. Those come with a doped-silicon gate, a 230 nm thick SiO₂ layer as dielectric, and gold source and drain contacts. In Chapter 2, the drawbacks of a BGBC configuration were explored, and SiO₂ is not an optimal dielectric for BGBC transistors based on [3]Ph and [5]Ph, as the presence of dangling bonds is detrimental to charge transport and its relative dielectric constant (3.7-3.9) is higher than the one of insulating polymers that are commonly employed as dielectric layers

in OFETs. So, lithographies were prepared employing the same patterns: those feature a channel width of 2 mm and channel lengths of 2.5 μm , 5 μm , 10 μm , and 20 μm .

After a few attempts at fabricating transistors based on this pattern, a different one, hereafter called CMS and shown in figure Figure 3.4(b), was preferred for lithographies. It has a channel width of 2 cm and channel lengths of 5 μm , 10 μm , 20 μm and 40 μm : the CMS longer channels lead to a higher channel resistance and so to a negligible contact resistance in comparison with the resistance of the active layer. Besides, the larger features allow for easy bar coating or spray coating of the gate in TGBC devices.



Figure 3.4 a) Schematic representation of a typical Fraunhofer pattern, with a channel width of 2 mm and channel lengths spanning from 2.5 μm to 20 μm . b) "CMS" pattern, with a channel width of 2 cm and channel lengths ranging from 5 μm to 40 μm .

Once the selected mask is mounted, the photoresist, i.e. S1813, is UV-cured for 8 seconds (Figure 3.5(b)). To estimate the exposure dose, a dosimeter with three sensors was employed. The 320 nm sensor detected a dose of 37.6 mJ/cm^2 , the 365 nm one detected 61.6 mJ/cm^2 , and the 405 nm one 141.6 mJ/cm^2 .

The final step is the developing, carried out by immersing the sample in Microposit MF-319 and gently moving it around for 30 seconds, after which the process is stopped by immersion in H_2O . During this time, the developer attacks and effectively dissolves the areas of the surface that were exposed to UV light, then it reaches LOR, that isotropically dissolves creating an undercut below S1813 (Figure 3.5(c)).

The formation of the undercut is crucial, since it prevents Cr and Au from depositing on the lateral walls of the lithography pattern during thermal evaporation. Were it not for the undercut, the metal contacts might get attached to the resists and end up stripped away along with the resists themselves.

BGBC photolithography

In this different configuration, the procedure is more or less the same, except for a few details.

First, the cleaning step is significantly less thorough with respect to TGBC configuration: the surface to be patterned is a soft Parylene layer, which would be damaged by sonic baths, so the samples are merely rinsed in acetone and isopropyl alcohol. The plasma asher step is skipped for the same reason.

LOR is spin-coated onto the Parylene layer with the usual recipe, but it is then annealed at 150 °C for 9 minutes, instead of 180 °C for 7 minutes, to avoid thermal degradation of the dielectric layer.

Subsequent steps are identical to the previous case.

Contact deposition and lift-off

This step is carried out the same way for both TGBC and BGBC configurations, except for the final cleaning through sonic bath, which is reserved to TGBC to avoid damage to the already deposited Parylene of BGBC substrates. The patterned sample is loaded into a thermal evaporator (two instruments were employed: PROvap Glovebox Integrated M-braun and Moorfield MINILAB-080), that operates in high vacuum ($P \sim 10^{-6}$ mbar). No mask is applied between the sample and the metallic sources, so that Cr and Au are evaporated all over the surface.

Cr is employed to favour the adhesion of Au, otherwise not prone to stick to glass. It is provided by a tungsten-core stick, which heats up through Joule effect (without melting) and releases atoms in vapor phase. Thanks to the high vacuum, those atoms have long mean free path and are able to reach the substrates, where they solidify. The deposited layer is 3 nm thick, and the deposition rate is 0.1 Å/s.

Next, Au wire is heated up by Joule effect, until it melts and evaporates. The atoms travel to the substrate without colliding with others thanks to the high vacuum, then they solidify on the surface. The deposited layer is 30 nm, while the deposition rate ranges from 0.1 Å/s to 0.5 Å/s (Figure 3.5(d)). Low rates ensure the formation of a good quality layer, without internal stresses or defects caused by large volume of incoming atoms in vapour phase.

Once the metal evaporation is over, it is time to remove the resists along with any excess of Cr and Au. This is achieved by leaving the sample in TechniStrip Micro D2 for at least 30 minutes or in n-methyl-2-pyrrolidone overnight. The very last step is a cleaning one, run with sonic baths in acetone, for 10 minutes, and IPA, for 5 minutes, to ensure complete removal of resists, excess metal residues and stripper (Figure 3.5(a)-(b)).

Figure 3.5(a)-(f) are the schematic representation of the whole contact deposition procedure.

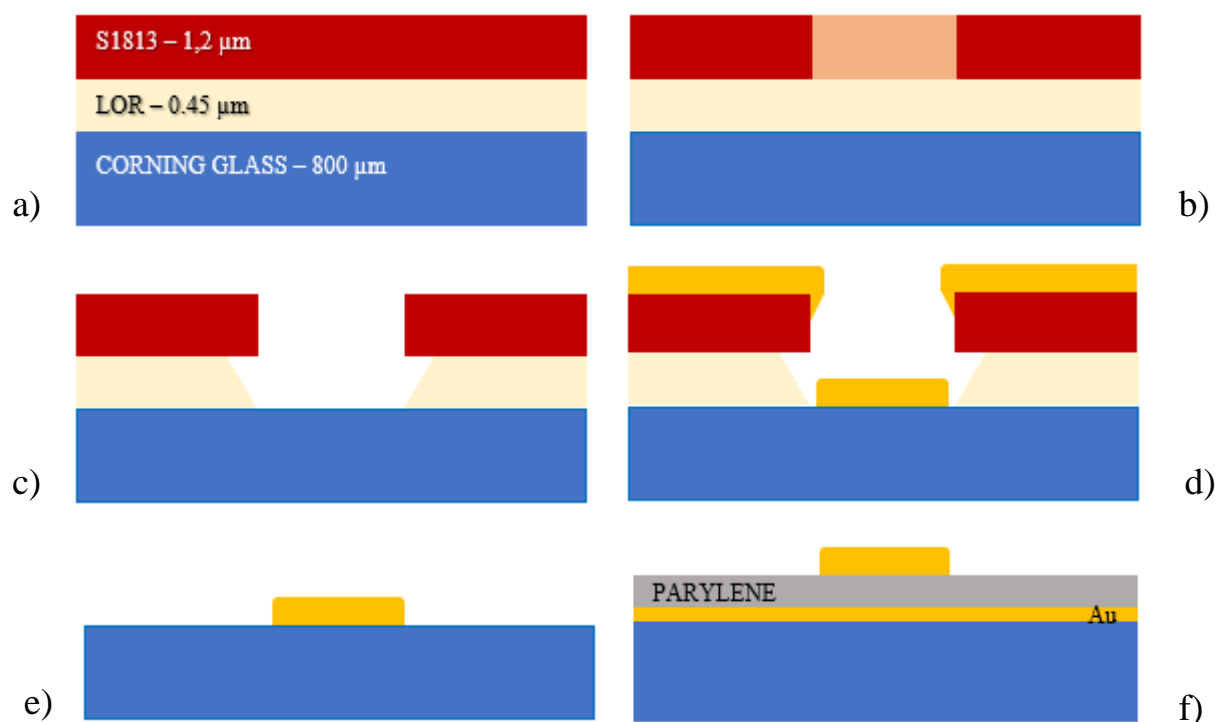


Figure 3.5 Schematic representation of the lithographic and contact deposition process for a TGBC device: **a)** spin coating of LOR and positive photoresist S1813, onto thoroughly cleaned Corning glass; **b)** UV-curing of S1813; **c)** developing step, leading to cured S1813 and LOR dissolution, and to the formation of an undercut; **d)** thermal evaporation of Gold all over the surface; **e)** removal of the resists and of excess metal during the lift-off step, leading to patterned Gold on glass substrate. **f)** Patterned gold on Parylene in BGBC configuration.

3.2.2 Active layer deposition

Early screening tests were conducted by dropcasting 12 μl from solutions containing cumulenic small molecules (4 g/l in 1,2-DCB) onto Fraunhofer substrates.

Dropcasting is a quick and easy technique to run preliminary tests, since it allows to observe bulk-like structures, and even accomplish electrical measurements, but it is not suitable to optimise thin films, due to the poor control over coverage, layer thickness, homogeneity, reproducibility.

As a better performing alternative, bar coating was picked as preferential technique to deposit and optimise films based on [3]Ph, [5]Ph and blends.

Bar coating is widely used to deposit organic semiconductors, because it allows to cover large areas quickly, granting good coverage, thickness control and uniformity. In fact, by setting several parameters, such as heating bed temperature, bar speed, bar-substrate gap, wire-wound rod diameter, it is possible to finely tune the deposition, and obtain easily reproducible films [59]–[61].

The instrument employed during this thesis work is a TQC Sheen Automatic Film Applicator AB4400, mounting a homemade system to control the bar-substrate gap at a micrometric scale, and a nitrogen flow system to accelerate solvent evaporation, if needed. The bar coater sits under a fumehood.

The procedure of bar coating a film starts with the cleaning of the substrate.

During this thesis work, semiconducting films were bar coated on a number of surfaces: low alkali 1737F Corning glass (from Prazisions Glas and Optik GmbH), with and without gold interdigitated electrodes on top, silicon wafers, glass microscope slides, and Parylene C layers. Except for the latter, which is a soft surface that might be damaged by aggressive cleaning, all the other substrates were sonicated in acetone for 10 minutes, in IPA for 5 minutes, and then, after a drying step assisted by nitrogen, they underwent a surface activation treatment in a plasma asher (Diener Electronic Femto Plasma) for 5 minutes, at 100 W of power and 40 mbar of pressure. Substrates with Parylene C already on, were simply rinsed in acetone and IPA.

The wire-bar also needs to be cleaned before (and after) bar coating a new film to ensure the removal of any residues from previous depositions, and any other form of contamination from the environment, since bars are stored outside the cleanroom.

Next, the substrate is placed on the heating bed, and the bar is brought above the front edge of the substrate. Then, it is time to set the deposition parameters. The effect of temperature and nitrogen flow will be discussed in Chapter 4. As for the gap between the bar and the substrate, it should be carefully set. In fact, if the bar sits too low, effectively in contact with the sample itself, the solution will be dragged onto the surface by the bar, rather than the surface tension, loosing uniformity in coverage and thickness. Also, damage could be caused to the surface underneath. If the bar sits too high, it will be harder to form a meniscus, which is fundamental in the working principle of this technique. The solution is dropcasted onto the bar itself.

By capillarity and due to the surface tension gradient, which is established in the system, the liquid will be driven to form a meniscus between the bar and the substrate (Figure 3.6(b)). A mass flow, triggered by a gradient in surface tension: this is called Marangoni effect; in particular, the mass will flow from the lower surface tension region to the higher one [59], [60].

Crystallisation will take place beneath the bar, which will move forward and will assist the phase transformation across the surface, while the solvent evaporates (Figure 3.6(a)). If the bar sits too high and a meniscus is not formed, the solution will be merely spread onto the surface, and it will crystallise less uniformly.

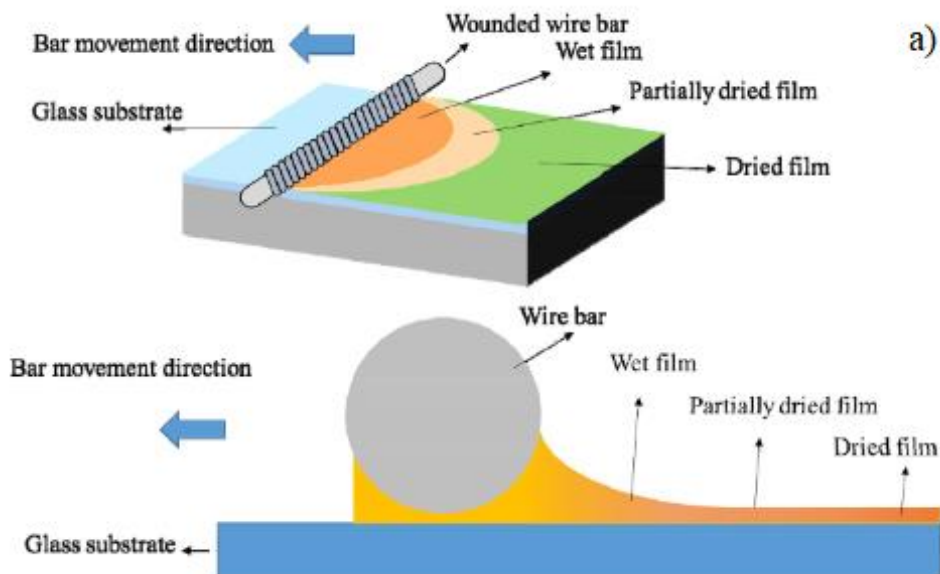
Indicatively, the bar should stand a few tens of micrometres above the substrate to effectively deposit [3]Ph and [5]Ph, with the former preferring a slightly narrower gap than the latter,

although this might be due to the different wire-bars employed, 6 μm for [3]Ph and 10 μm for [5]Ph.

Unlike dropcasted films, bar coated ones are less likely affected by the coffee ring effect.

The bar speed also plays an important role in the deposition process, as the thickness of the film strongly depends on it. Indeed, the relation between bar speed and film thickness follows a power law: $t \propto v^\alpha$, where t represents the bar coated thickness, v is speed and α is a coefficient. As Figure 3.6(c) shows, $\alpha = -0.95$ in evaporation regime, i.e. when bar speed is below 1 mm/s, meaning that the thickness decreases by increasing the speed. On the contrary, when the bar speed rises above 1 mm/s, $\alpha = 0.64$, and the thickness increases with the bar speed: this is Landau-Levich regime [60].

Finally, the solvent can also affect the deposition, especially in conjunction with temperature: indeed, some solvents decrease their surface tension when the temperature increases, potentially leading to loss of coverage and film uniformity [59].



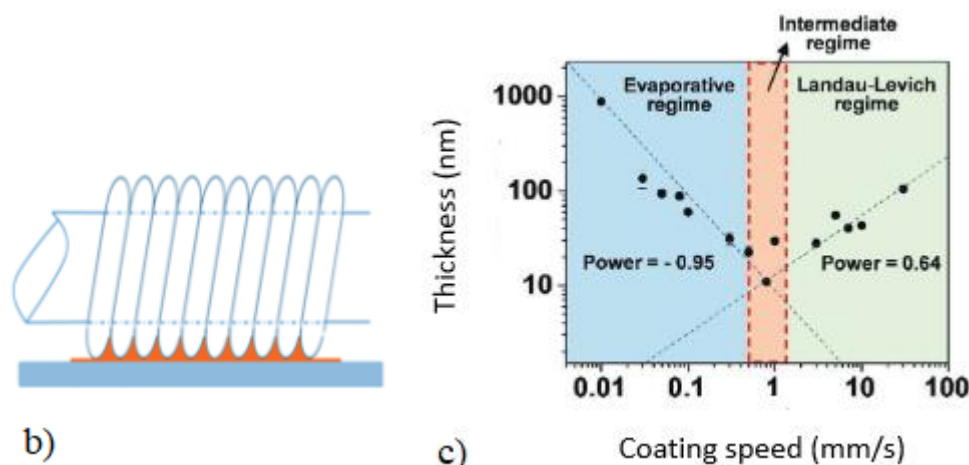


Figure 3.6 a) Schematic representation of the bar coating process [62]. b) Representation of a wire-bar creating a meniscus [61]. c) Regimes of deposition and thickness trends according to the bar speed-thickness relation [60].

3.2.3 Dielectric deposition

Parylene C was selected for the dielectric layer of the transistors studied in this thesis work.

The reasoning behind this choice is twofold: one has to do with the material characteristics, the other one with the deposition technique.

Parylene C, whose repeat unit is shown in Figure 3.7, deposits conformally to the substrate underneath, especially when evaporated at very low pressure, creating a pin-hole free barrier. Its low permeability to oxygen and other gases makes it effective in stabilising reactive layers underneath it. Parylene C is commonly used as dielectric material in OFETs, its dielectric constant being 2.95 [63]. Such low value is favourable for field effect transistors, as mobility μ is linked to the dielectric layer capacitance through the following relation in both linear and saturation regime: $\mu \propto \frac{1}{C}$. Capacitance is in turn directly proportional to the material dielectric constant ($C \propto \epsilon_r$): so a low dielectric constant causes higher mobilities.

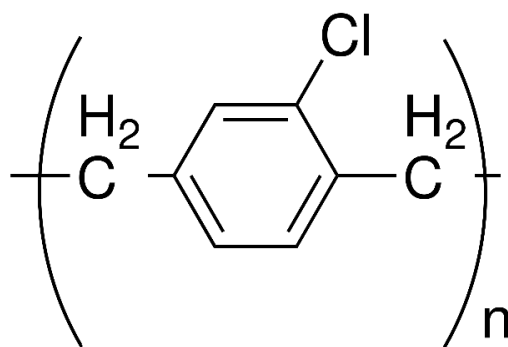


Figure 3.7 Parylene C repeat unit.

The second reason supporting the selection of Parylene C as dielectric material has to do with it being deposited by chemical vapour deposition (CVD), a technique that does not involve solvents or annealing, both potentially harmful for the cumulenes layer.

Some drawbacks of this material are related to its mechanical properties. It is a soft material, easily indented and damaged, and, although it is usually flexible, it can become slightly more brittle when deposited at very low pressures, i.e. when it is less amorphous. Similarly, exposing Parylene to thermal treatments might induce some degree of crystallisation, hardening the material and making it more brittle [63].

The instrument used to deposit Parylene C is Speciality Coating System PDS 2010.

The procedure is as follows. Dichloro-di-p-xylylene, the dimer precursor, is loaded into a vaporiser, which is connected to a furnace, set at 720 °C. Pyrolysis occurs and the resulting monomer, in vapour phase, travels to the main chamber of the instrument, where samples are kept in vacuum. When the monomer molecules reach the substrate surface, they polymerise, forming a compact layer.

The thickness of the layer varies according to the needs, but an average of 400 nm was deposited for the transistors presented in this work. A thicker layer makes for a more effective barrier from oxygen and water, and reduces the risk of a damaged dielectric layer, so short circuits. On the other hand, thinner Parylene C layers lead to higher currents. In addition, depositing a large amount of Parylene C at low pressure can be very time consuming, so a thinner layer is more efficient.

Parylene C can also be employed as an encapsulant, to protect the finished device from the environment. In this case, a layer of 1000 nm is deposited to ensure a thick barrier.

To measure the thickness of the deposited Parylene C layers, a mechanical profilometer (Alpha-Step IQ surface profilometer) was employed.

3.2.4 Gate deposition

Different gate strategies were actuated.

Starting from BGBC configuration, the gates were made of thermally evaporated gold. The exact same procedure described in paragraph 3.2.1 is valid.

In this case, gold was evaporated either on the entire substrate surface, for Fraunhofer-like patterns, or selectively through a mask, for CMS patterns.

As for TGBC devices, the main gating technique involved ink-jet printing a Poly(3,4-ethylenedioxythiophene):Poly(styrenesulfonate) ink (PEDOT:PSS, Clevios PJ700, purchased from Heraeus).

PEDOT:PSS, in Figure 3.8(a) is a widely used organic conductor, due to its appreciable conductivity, its flexibility, and its versatility [64].

In the specific context of this work, PEDOT:PSS was selected because its water-based formulation does not risk to damage the underneath layers. Moreover, it can be ink-jet printed at low temperatures, even at room temperature. No wettability issues were ever detected, when printing PEDOT:PSS on top of Parylene C.

PEDOT:PSS was ink-jet printed from a SAMBA 12-nozzle cartridge (from Fujifilm Dimatix) using a Fujifilm Dimatix DMP2831 printer.

Ink-jet printing is a deposition technique that provides high resolution, and good versatility, as virtually any design can be printed. These technologies can be classified as either continuous or drop on demand, and the latter can be based on the local vaporising of the ink in the jet chamber (thermal ink-jet printing), or on piezoelectricity, which is the most common [64]. The Dimatix printer employed in this thesis work belongs to the piezoelectric category. When a voltage is applied, the piezoelectric piece deforms, and in doing so, it mechanically pushes the ink outward, as shown in Figure 3.8(b).

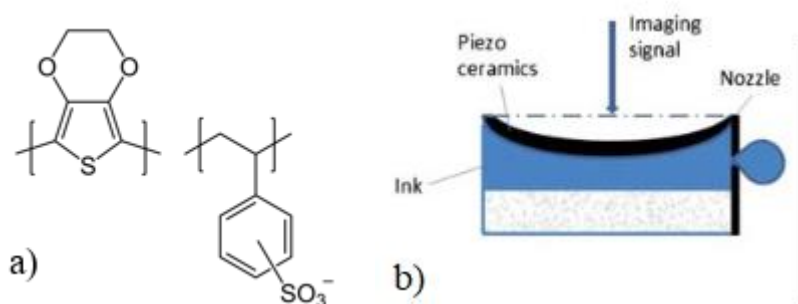


Figure 3.8 a) PEDOT and PSS repeat units. b) Schematic representation of the piezo-ceramic in an ink-jet printer cartridge [64].

The second strategy attempted to deposit gates still involves PEDOT:PSS, in the same formulation as before, but the electrode was bar coated instead of printed. The description of the bar coating technique explained above does not really apply in this case, as the achievement of a homogeneous, uniformly covering layer is not the goal. Instead, the bar acts simply as an applicator, and the substrate-bar gap is set significantly larger than usual, to prevent the ink from spreading beyond the channel region of the devices. A 20 μm bar is used, and the PEDOT:PSS solution is dropcasted directly on the sample rather than on the bar.

The third and last technique employed for gating is the spray coating of an ink based on activated carbon (AC), with ethanol as a solvent. Said ink is currently the subject of a work soon to be published and patented, which is the reason why very few details will be given about the binder, the ink preparation, and the ink deposition. A regular airbrush was the instrument employed to spray coat the AC ink onto the substrate, selectively on the channel regions, through a mask.

Finally, Figure 3.9 depicts the schematic representations of a) a completed TGBC, and b) a completed BGBC device.

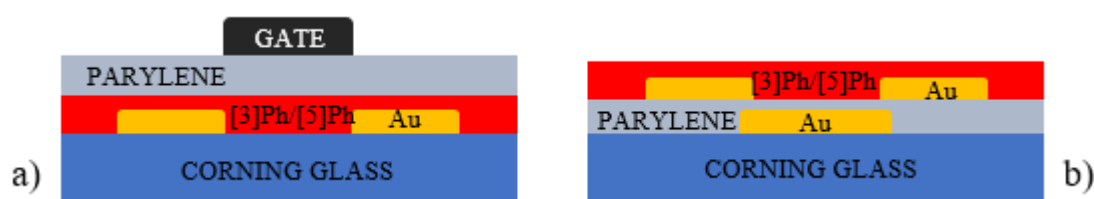


Figure 3.9 a) Schematic representation of a TGBC device. b) Schematic representation of a BGBC device.

3.3 Characterisation techniques

Several characterisation techniques were employed to study the cumulenenic molecules included in this thesis work.

Polarised light optical microscopy and atomic force microscopy were used to observe the morphology and the topography of the semiconducting films, UV-Vis spectroscopy was dedicated to detecting signs of degradation, and Semiconductor Parameter Analyser was employed to study the behaviour of the devices based on [3]Ph, [5]Ph and blends.

3.3.1 Polarised optical microscopy

Polarised light optical microscopy (POM) is a quick and easy technique to observe the morphology of a film, including bulk-like and thin film crystalline structures, shape and size of grains, coverage and homogeneity, degradation symptoms. It is a microscopy mode efficient when observing crystalline materials: they can be defined as birefringent, meaning that their refractive index depends on the polarisation of light.

The instrument used is a Zeiss Axio Scope A1, equipped with a polariser.

The polariser filters the light so that only the component oscillating in one direction gets through to the sample. When polarised light hits a crystalline, anisotropic sample, it is split into two waves. Those will travel at a different speed, due to the above-mentioned difference in the

refractive index along the two different directions (birefringence), so that they will end up being out of phase with each other.

The result of the constructive or destructive interference between the two out of phase waves is what gets reflected back to the analyser. This will give back an image with enhanced contrast.

This analysis can be exploited to tell apart crystalline and amorphous films, as well as isotropic and anisotropic materials. Amorphous and anisotropic materials will appear black, since amorphous materials are not birefringent, and isotropic ones only give rise to destructive interference, as the two waves travel with the same phase.

[3]Ph and [5]Ph films are both crystalline and anisotropic, so this characterisation technique is effective.

On the other hand, those materials are severely photosensitive: POM imaging can only be resourced to after deposition tests, or after other analysis techniques, to prevent light degradation from altering the results.

Figure 3.10(a) and 3.10(b) show what happens to films of [3]Ph and [5]Ph, respectively, after 60 seconds of exposure to the microscope light. In particular, in Figure 3.10(b), it is possible to compare a pristine region with one that underwent photodegradation.

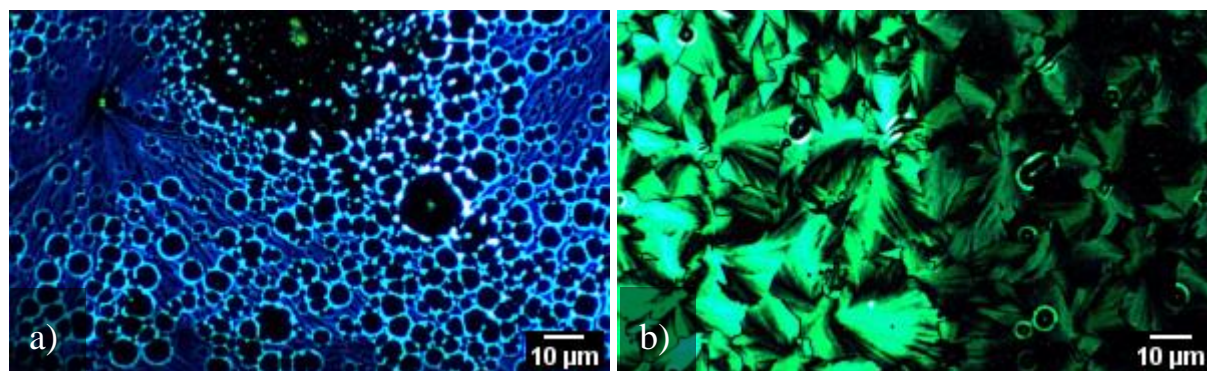


Figure 3.10 a) POM image of a [3]Ph film, after being exposed to the light of the microscope for 60 seconds, 90° polarisation. b) POM image of a [5]Ph film, split into a undegraded region and a region exposed to the light of the microscope for 60 seconds; 90° polarisation.

3.3.2 UV-Vis spectroscopy

UV-Vis spectroscopy is a fairly straightforward characterisation technique, which can produce important information about the analyte, such as optical band gap, from the absorption onset, degradation or transformation events, from the alteration in the shape of the spectrum, transitions, from the location of the peaks.

Both thin films and solutions (in quartz cuvettes) can be analysed, provided that a baseline is acquired, to exclude from the resulting spectra the influence of the background, i.e. air, external light, the substrate or the solvent.

The instrument employed was a Perkin Elmer Lambda 1050 UV/Vis/NIR spectrophotometer, and it was used to detect degradation as well as to extract information about electronic transitions.

A grating monochromator selects wavelengths from the deuterium and tungsten halogen sources, with a resolution up to 1 nm, starting from the lowest energy wavelength. Wavelength by wavelength, the monochromatic light hits the sample, which absorbs some light. The residual light reaches the detector, which reads the transmitted light intensity at each frequency. Due to the detector sensitivity and the high molar extinction coefficient of the cumuleninic molecules, it was necessary to dilute the solutions to 0.01 g/l in order to get a significant spectrum.

Another setup was exploited to run stability tests on those two materials, and it can be observed in Figure 3.11. In this case, the aim is to detect simultaneously absorbance variations along the full spectral range, at the cost of a lower wavelength resolution.

White light, emitted by a deuterium-halogen lamp (Avantes AvaLight-D(H)-S) was used as a probe during the measurements. The transmitted light intensity was collected by a spectrometer (Avantes AvaSpec-HS2048XL-EVO) in transmission, being then elaborated and turned into absorption spectra. In addition to the white light, LEDs emitting at different wavelengths, i.e. 660 nm (Thorlabs M660L4-C5), 530 nm (Thorlabs M530L4-C5), 470 nm (Thorlabs M470L5-C5), 405 nm (Thorlabs M405LP1-C5), 365 nm (Thorlabs M365L3-C5), were shined on the sample one at a time for 30 seconds each, starting from the red one and proceeding by decreasing the emitted wavelength. The LED light was impinging on the samples perpendicularly to the transmission line, so to induce photodegradation without being collected by the detector. The integration time for all measurements was set at 2.5 milliseconds, and the power density associated to the LEDs was about 40 mW/cm².

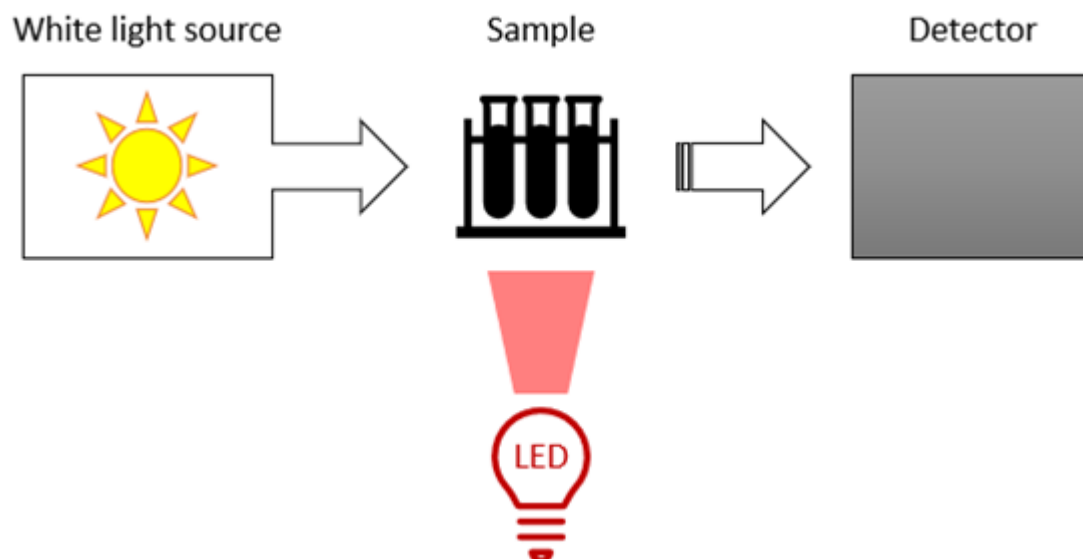


Figure 3.11 Setup for photodegradation analysis, involving a white light source and a LED.

3.3.3 Electrical characterisation (Semiconductor Parameter Analyser)

Semiconductor parameter analyser (SPA) is an instrument used to investigate the electrical behaviour of semiconducting materials, mainly by measuring IV characteristics to extract the conductivity in two electrodes devices, along with transfer and output curves in working transistors to extract the charge mobility and other relevant parameters.

The measurements were run through an Agilent B1500A Semiconductor Device Analyzer, on a 4 probe stage, equipped with a microscope, from Wentworth Laboratories. Tests were carried out both in air and in nitrogen atmosphere, the latter being the preferential route, since in a glovebox the oxygen and water content is below 0.1 ppm, which ensures better stability to the devices.

From an operative point of view, the measurements proceed as follows: 3 of the 4 probes are contacted to the electrodes of the devices, i.e. source, drain and gate. The microscope is only turned on for brief intervals of time, in order to effectively contact the transistors, and then it is switched off to avoid degradation from light, especially when the material is active.

In relation to this work, two types of curves were obtained by SPA, the transfer curve and the output curve.

The transfer curve is obtained in a two-step analysis, each carried out at a fixed drain voltage (V_D), where drain current (I_D) is measured while varying the gate voltage (V_G). The first step occurred at $V_{D,lin} = -5$ V, that is a low, negative voltage, which establishes a linear regime in p-type semiconductors, such as [5]Ph and [3]Ph: a forward and reverse I/V sweep are performed

from $V_G = 10$ V to $V_G = -40$ V, while I_D , I_s , I_G (i.e., the leakage current, produced by charges piercing through the dielectric layer) are measured.

The second step takes place at $V_{D,sat} = -40$ V, which is a substantially negative voltage driving the device into the saturation regime. Again, V_G varies from 10 V to -40 V, and back, while the above-mentioned currents are measured.

It is worth pointing out that the range of V_G should be picked, taking a few points into consideration. If transistors switch on late, they need higher voltages to get past the threshold voltage, after which the currents weakly depend on V_G . On the other hand, high voltages are associated to thermal degradation, thermal shocks, bias stress, and trap formation, so it is not advisable to set too intense voltages, whether they are negative or positive.

[3]Ph and [5]Ph were also tested in n-transfer mode, meaning that the applied biases were positive, to extract and transport electrons instead of holes. The tests confirmed that both materials work as unipolar semiconductors.

From the transfer curve, a few important parameters can be calculated through a MATLAB (MathWorks) script, written by Stefano Pecorario.

- The field effect mobility, in both linear and saturation regime, was extracted by applying Eq. (1) and (2). Here, L is the channel length, W the channel width, C is the dielectric capacitance per unit area, V_G is the gate voltage, $V_{D,lin}$ is the drain voltage in linear regime, $I_{D,lin}$ and $I_{D,sat}$ are the drain currents, respectively in linear and saturation regime. It should be underlined that the calculated value does not correspond to the intrinsic mobility of the material. Rather, it is a device property, since the contact resistance and leakage current also play a role. Indeed, saturation mobility is usually considered more reliable than linear mobility, because in saturation the leakage is usually more negligible.

$$\mu_{lin.} = \frac{L}{WCV_{D,lin.}} \left| \frac{\partial |I_{D,lin.}|}{\partial V_G} \right| \quad (1)$$

$$\mu_{sat.} = \frac{2L}{WC} \left(\frac{\partial \sqrt{|I_{D,sat.}|}}{\partial V_G} \right)^2 \quad (2)$$

- The threshold voltage, V_{th} , is the voltage, past which the drain current stops depending on the gate voltage. It was extracted by fitting I_D as a function of V_G in the linear regime and then finding the intersection with the voltage axis, while in saturation it was the square root of I_D to be fitted in the same way and intersected with the voltage axis.

- I_{on}/I_{off} is the ratio of the maximum detected current over the minimum one.
- The subthreshold slope is an indication of how fast the device switches from being off to be on. It was obtained by linearly fitting the I_D curve in logarithmic scale when $V_G < V_{th}$, and then by calculating the reciprocal value of the slope.
- V_{on} is the voltage, after which the transistor starts switching on. It can be located in the point when the slope of I_D in logarithmic scale starts to increase, until it reaches V_{th} .
- The reliability factor is an esteem of the ideality of the device, from the transfer curve. The closer it is to 1, the more reliable the extraction of the above-mentioned values is. It is calculated by applying Eq. (3) and (4).

$$r_{sat.} = \left(\frac{\sqrt{|I_{D \max.}|} - \sqrt{|I_{D(V_T)}|}}{|V_{G \max.} - V_{Tsat.}|} \right)^2 \bigg/ \left(\frac{WC}{2L} \mu_{sat.} \right) \quad (3)$$

$$r_{lin.} = \left(\frac{|I_{D \max.}| - |I_{D(V_T)}|}{|V_{G \max.} - V_{Tlin.}|} \right) \bigg/ \left(\frac{WC V_{D \ lin.}}{L} \mu_{lin.} \right) \quad (4)$$

Examples of transfer curves are presented in Chapter 6.

The other curve obtained by means of SPA is the output curve. During each step of measurement, the gate voltage is kept fixed, while the drain voltage varies from 0 V to -40 V in a forward sweep. At each step, the gate voltage negatively increases by 10 V, until it reaches -40 V. The collected data is the drain current.

The most important information that can be inferred from an output curve is the efficiency of the charge injection from metal contacts to the active layer. In an ideal device, at voltages close to 0, the drain current in logarithmic scale should be linearly dependant on the drain voltage, like in an ohmic junction.

If injection issues take place, that region of the curve bends to resemble an “S” shape. An example of this will be offered in Chapter 6.

3.3.4 Atomic force microscopy

Atomic force microscopy (AFM) is a highly refined technique to investigate surface metrology with atomic resolution, relying on a scanning probe, which runs across the surface, line by line, and collects data regarding topography, thickness measurements, but also mechanical and electrical properties.

The AFM probe is typically a sharp tip, made of micromachined silicon, and it is mounted on a cantilever that can oscillate. As the probe approaches the sample and establishes an interaction force with it, the cantilever bends. The deflection is detected by a photodiode, which collects the signal of the laser diode focused on the cantilever, as represented by Figure 3.12.

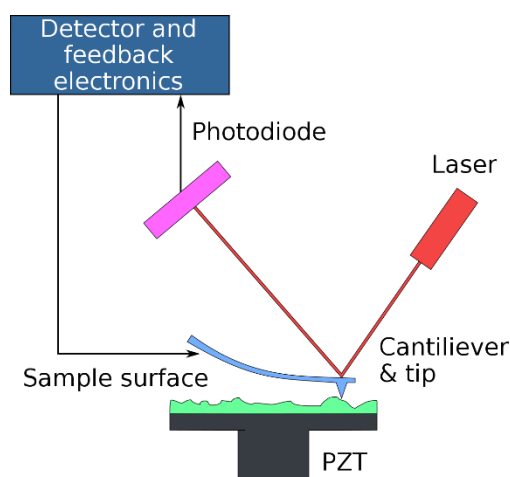


Figure 3.12 Schematic representation of the working principle of an AFM.

The microscope can operate in either contact or tapping mode.

The contact mode involves the tip being pressed onto the sample. This can cause damage to both the analyte and the tip.

The tapping mode works with the tip in very close proximity to the substrate, vibrating around the resonance frequency: the attractive and repulsive forces generated by the interactions between the sample and the tip itself damp the motion.

Data are collected in the form of 2D images of the topography, amplitude and phase, but 3D images can be obtained, as well as several parameters, such as root mean square (RMS) roughness.

The instrument employed in this thesis work was a Keysight 5699LS in tapping mode, while the data were elaborated through the software Gwyddion.

4. EXPERIMENTAL RESULTS – FILM DEPOSITION AND CHARACTERISATION

4.1 [5]Ph optimisation

The ultimate goal of this thesis work was the fabrication of field effect transistors based on thin films of [5]Ph. With this regard, it is of paramount importance to optimise the thin film deposition, which is essential to achieve the best charge transport possible. Furthermore, it is important to identify a suitable semiconductor-dielectric interface and establish the most favourable transistor architecture.

Being similar to [3]Ph, the optimisation process of [5]Ph thin films started from the conditions that had already proved to allow for a good [3]Ph deposition, but then several changes to certain parameters were tested out. Optimised [3]Ph thin films were previously achieved by wire-bar coating from 10 g/l in 1,2-DCB solutions, using a 6 μm bar moving at 30 mm/s, with bed temperature of 80 °C, and N_2 flow on. Solutions are stirred at 50 °C for at least one hour before deposition, and all the process are performed in air, in a yellow-room.

When deposited according to the optimised conditions listed above, [3]Ph molecules arrange in homogeneous, polycrystalline thin films, about 20 nm thick and made of few-micrometres large crystalline grains, with low roughness and absence of defects. In this arrangement, the molecules are aligned with the cumulenenic chains quasi-parallel to the substrate (Figure 4.1), so that the π -stacking also occurs parallel to the substrate, leading to an anisotropic charge transport: it is more efficient in the horizontal direction, i.e. parallel to the substrate, rather than vertically [13].

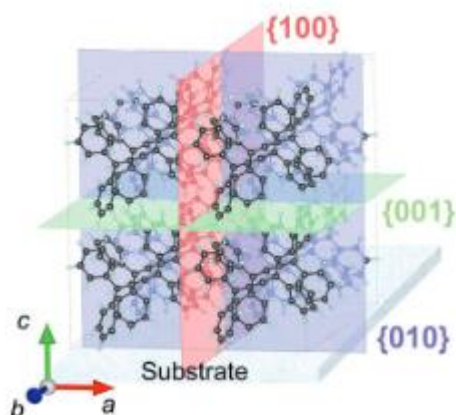


Figure 4.1 Arrangement of [3]Ph, whose chains are quasi-parallel to the substrate [13].

Having large structures means less grain boundaries, which are typically poorly ordered areas that hinder charge transport, although grain size is not the only factor influencing it. Indeed, the optimised conditions are not the ones inducing the formation of the largest grains, but the optimised film also features other desirable characteristics: the surface smoothness reduces the presence of traps at the semiconductor-dielectric interface, and the absence of intra-grain defects reduces internal traps.

As a first step, a similar morphology was pursued for [5]Ph thin films, too.

4.1.1 Solution formulation

1,2-DCB was the solvent of choice for [3]Ph, mainly because the small molecule shows good solubility in it and because of its boiling point at 180 °C, ensuring solvent stability over a broad range of temperature.

Actually, [5]Ph is even more soluble in 1,2-DCB, making the solution preparation step much quicker, and effective even when stirring at low temperatures (for example, 35 °C). The latter advantage is crucial for reasons related to thermal degradation, but the subject will be explored in detail in the next chapter.

Toluene was also tried out, but its lower boiling point (110 °C) accelerated the solvent evaporation after bar coating, with respect to 1,2-DCB, and prevented [5]Ph from creating a homogeneous film with a good coverage. Indeed, if evaporation kinetics is too fast, crystallisation nuclei do not have sufficient time to grow and arrange in a convenient morphology. So, 1,2-DCB was confirmed as solvent of choice for [5]Ph deposition, as well.

There were attempts at bar coating [5]Ph both from cool (35 °C – 40 °C) and hot solutions. In this context, “hot” means as hot as the deposition temperature: after the stirring process, vials

were left on the coater bed, already set to deposition temperature, for a few minutes to thermalise, before moving on to bar coating. Cool solutions behaved better, probably due to thermal stability reasons (see Chapter 5).

Moreover, the first bar coated samples came from solutions stirred for a few hours at 50 °C, according to the procedure employed for [3]Ph. Thermostability tests (see Chapter 5) revealed that such a long stirring at that temperature was enough to damage the solution, and so that particular step was eventually shortened to 30 minutes at 35 °C for 10 g/l solutions. In fact, for less concentrated solutions, such as 1 g/l or 5 g/l, stirring at room temperature for 30-60 minutes was sufficient.

Such low concentrations, though, did not produce particularly good films. Small crystals with high aspect ratio were the main structure. Good results, i.e. compact, homogeneous films with larger grains, were obtained by bar coating solutions at 10 g/l, 20 g/l and 30 g/l. To avoid overusing the material, a concentration of 10 g/l was then picked as the one to be optimised.

Figure 4.2 (a) and 4.2(b) show two films of [5]Ph, wire-bar coated from 1,2-DCB solutions at concentration of 5 g/l and a 20 g/l solution, respectively. All the other parameters were kept fixed for this test: deposition temperature at 60 °C, bar speed at 45 mm/s, with N₂ flow off, in yellow room.

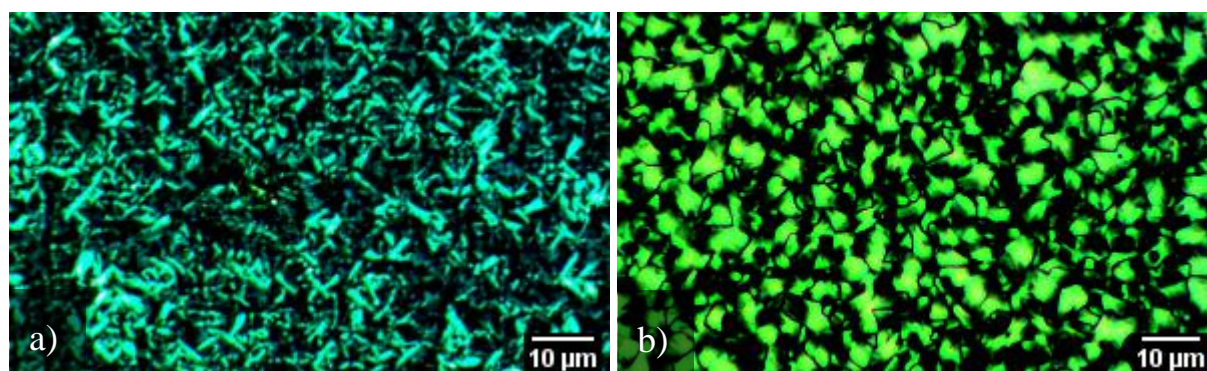


Figure 4.2 a) POM image of a [5]Ph film, wire-bar coated at $T = 60$ °C, with bar speed $v = 45$ mm/s, with N₂ flow off, in dark conditions, in air, from a 5 g/l in 1,2-DCB solution, taken with 90° polarisation. b) POM image of a [5]Ph film, wire-bar coated at the same conditions, but from a 20 g/l solution, taken with 90° polarisation.

Solutions of “C6-5”, a cumulenenic molecule very similar to [5]Ph, but featuring alkyl chains bonded to the phenyl end-groups, were also deposited, but with no satisfactory results, since it was impossible to get a film from that molecule using deposition conditions similar to [3]Ph and [5]Ph.

More solutions were prepared that were based on blends of [5]Ph and insulating polymers, namely PS and PMMA, in 1,2-DCB. The stirring process for those solutions would happen in two steps: 30 minutes at 40 °C for each unblended, pristine solution ([5]Ph and the polymer), then another 30 minutes of stirring at the same temperature for the final blend solution, to ensure adequate solvation of both chemical species.

The addition of the polymers did alter the morphology of the films, as new structures appeared, but it also made the films less homogeneous, with significant differences within the same sample.

Figure 4.3(a) depicts a [5]Ph:PS film, wire-bar coated from a 1:1 10 g/l solution in 1,2-DCB, at 80 °C, with a bar speed of 30 mm/s, with no nitrogen flow on, in yellow room, in air. Fibre bundles appear to be dominant in the morphology, with significant variability in size and orientation. With this kind of morphology, charge transport could be efficient along the axis of each fibre or sheaf, but not in the perpendicular direction to that, as the structures are separated by amorphous regions and voids. Besides, it was not possible to arrange the fibres so that they would be equally oriented, to exploit their anisotropic charge transport.

The film based on [5]Ph:PMMA blend (1:1, 10 g/l in 1,2-DCB), wire-bar coated at the same conditions, is shown in Figure 4.3(b): this blend arranges in more defined and overall larger crystalline grains, although some fibres are still present.

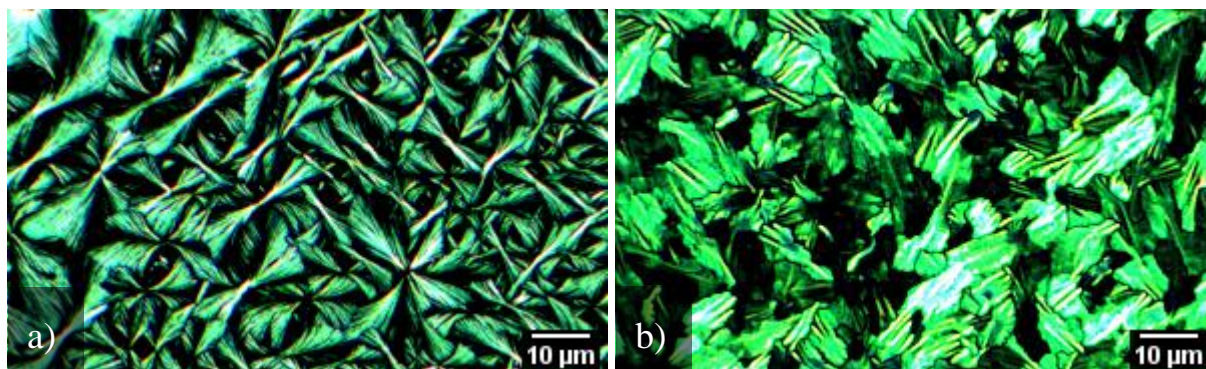


Figure 4.3 a) POM image of the main structure in a [5]Ph:PS film, taken with 90° polarisation. b) POM image of the main structure in a [5]Ph:PMMA film, taken with 90° polarisation.

Small molecule-polymer ratios of respectively 1:1 (10 g/l) and 1:3 (5 g/l : 15 g/l) were tested: for both polymers, the latter produced better films locally, but much more variability across the same sample. In particular, whole areas were completely amorphous, suggesting that [5]Ph was not present uniformly all over the surface, the size and shape of the structures varied a lot, and

defects were quite common. So, the former ratio was deemed more efficient to fabricate large-area transistors.

Figure 4.4(a) shows a film based on the blend [5]Ph:PS (5 g/l : 15 g/l in 1,2-DCB), wire-bar coated at $T = 80\text{ }^{\circ}\text{C}$, with bar speed of 30 mm/s, with no nitrogen flow. Together with the typical fibre bundles, there are also longer, oriented fibres: those usually form on the border of the samples, while in this case this kind of defect was present in several regions of the film.

Figure 4.4(b) depicts a film of [5]Ph:PMMA (5 g/l : 15 g/l in 1,2-DCB), deposited at the same conditions just described. This time, amorphous spots can be observed as well as grains of many different sizes and shapes.

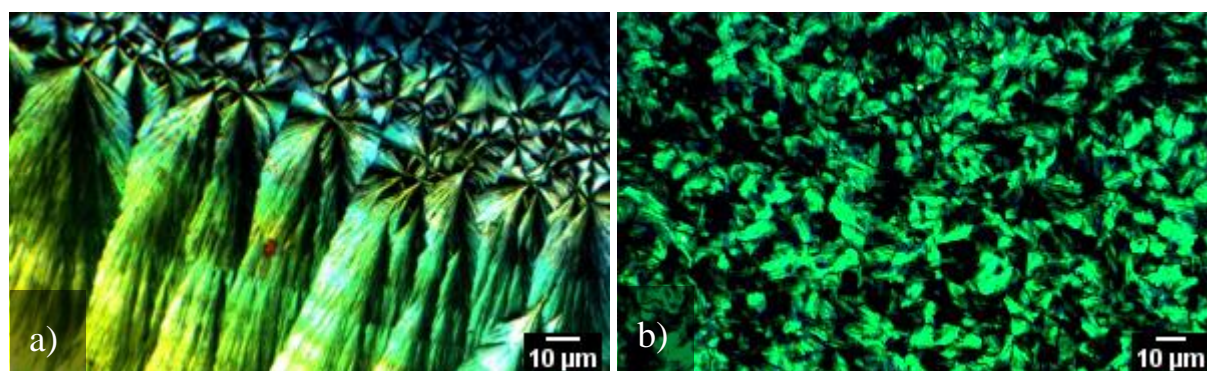


Figure 4.4 a) POM image of a film based on the blend [5]Ph:PS (5 g/l : 15 g/l in 1,2-DCB), wire-bar coated at $T = 80\text{ }^{\circ}\text{C}$, with bar speed of 30 mm/s, with no nitrogen flow, in dark conditions, in air; picture taken under 90° polarisation. b) POM image of a film based on the blend [5]Ph:PMMA (5 g/l : 15 g/l in 1,2-DCB), wire-bar coated at the same conditions as before.

Ultimately, films based on [5]Ph on its own looked better under POM and they also worked better in transistors, as it will be shown in Chapter 6. The blends did not produce repeatable enough films: complete surface coverage was not always achieved, and there was a lot of variability in the size and shape of the structures, leading to very unpredictable results when bar coating aforementioned solutions.

4.1.2 Deposition temperature

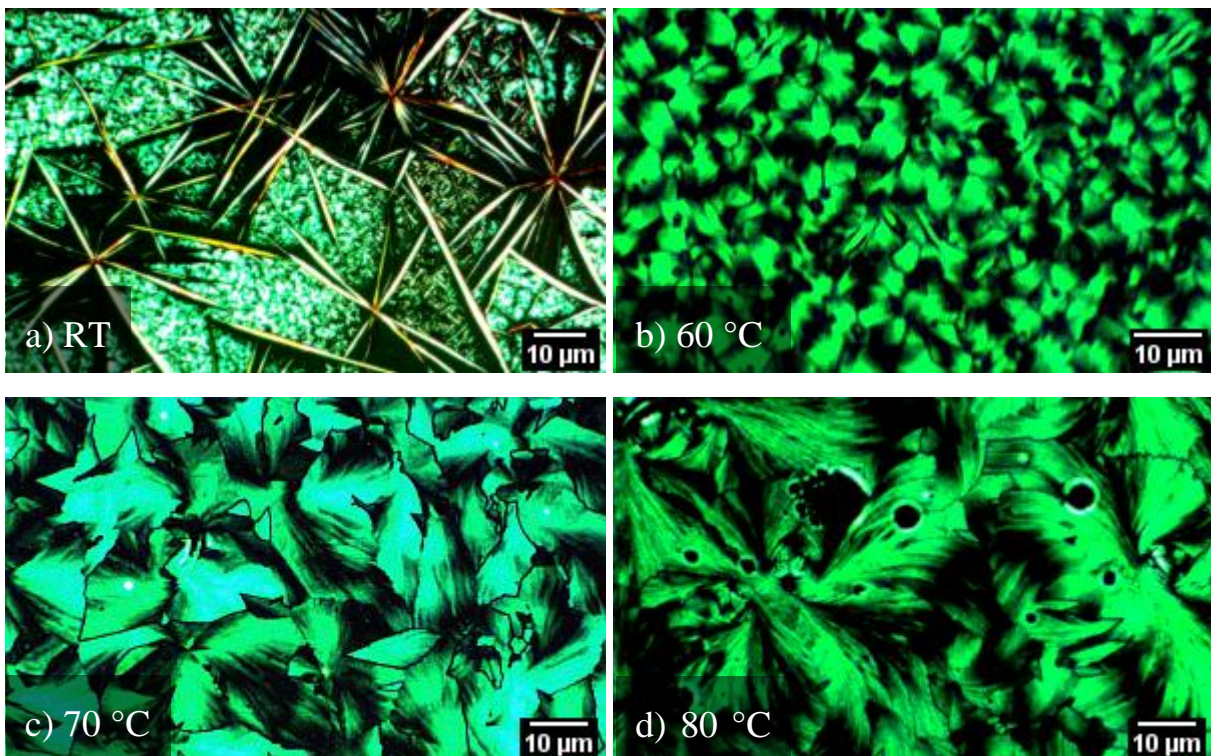
The deposition temperature is a crucial parameter since it strongly influences the kinetics of the solvent evaporation and film formation. For instance, it affects both the nucleation and crystal growth rates. Furthermore, small molecules films formed at different temperatures might display polymorphic structures other than the bulk one [65]. Finally, too high deposition

temperature might damage the film by thermally activated transformations or by thermal shock while cooling.

Several deposition temperatures were tested for solutions of [5]Ph, [5]Ph:PS and [5]Ph:PMMA, and it should be noted that samples stayed on the bar coater plate for under a minute, after the deposition, merely to ensure solvent evaporation. Bar speed was set to 45 mm/s, and nitrogen flow was off.

Starting with pristine [5]Ph, it is possible to see that at room temperature (Figure 4.5(a)) randomly oriented needle-like structures were predominant. In between those, a film made of very small crystalline grains was observed. This morphology can lead to a very inefficient charge transport, so room temperature for deposition was ruled out. At 60 °C (Figure 4.54.4(b)) the films appeared more homogeneous, and coverage was good, but grains were quite small and grain boundaries somewhat thick. At 70 °C (Figure 4.5(c)), crystalline grains were enlarged, although grain boundaries still showed up. At 80 °C grains were even larger, but signs of degradation started appearing: Figure 4.5figure 4.4(d) depicts a region, affected by thermal damage. At 110 °C the films showed major signs of thermal degradation in several regions, with voids opening across the samples, as visible in Figure 4.5(e).

70 °C ended up being a good compromise: the films deposited at that temperature were homogeneous, they showed great coverage and decently sized grains.



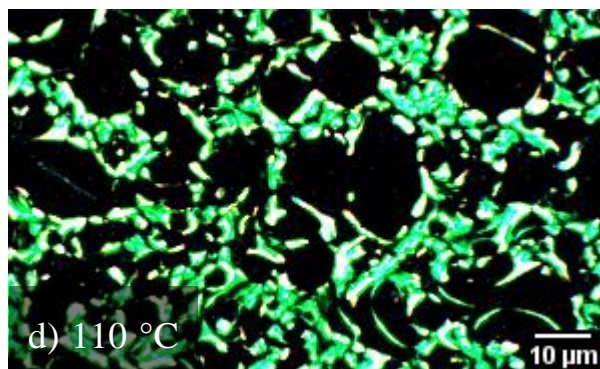


Figure 4.5 POM images (90° polarisation) of [5]Ph film wire-bar coated at **a)** room temperature, **b)** 60 °C, **c)** 70 °C, **d)** 80 °C, **e)** 110 °C. **f)** POM image of the arched, fibre-like structures, commonly present as defects in [5]Ph films.

Similar tests were run on solutions of [5]Ph:PMMA with a small molecule-polymer ratio of 1:1 (10 g/l in 1,2-DCB).

The fixed parameters were bar speed of 30 mm/s, no nitrogen flow, dark conditions, in air. The samples bar coated at 60 °C, which Figure 4.6(a) is an example of, displayed smaller grains with respect to those bar coated at 80 °C (Figure 4.6(b)). Besides, the shape of the grains seemed to be slightly different between the two: the structures formed at 60 °C were less smooth, featuring thin ridges that were less commonly observed in the higher temperature films.

When a deposition temperature of 110 °C was set, degradation of the film was obvious, and in a larger extension with respect to [5]Ph films. Indeed, 110 °C approaches PMMA glass transition, that ranges from 105 °C to 120 °C, depending on synthesis and average molecular weight [66]. This might explain why [5]Ph:PMMA films turned out to be more sensitive to high temperature than [5]Ph ones.

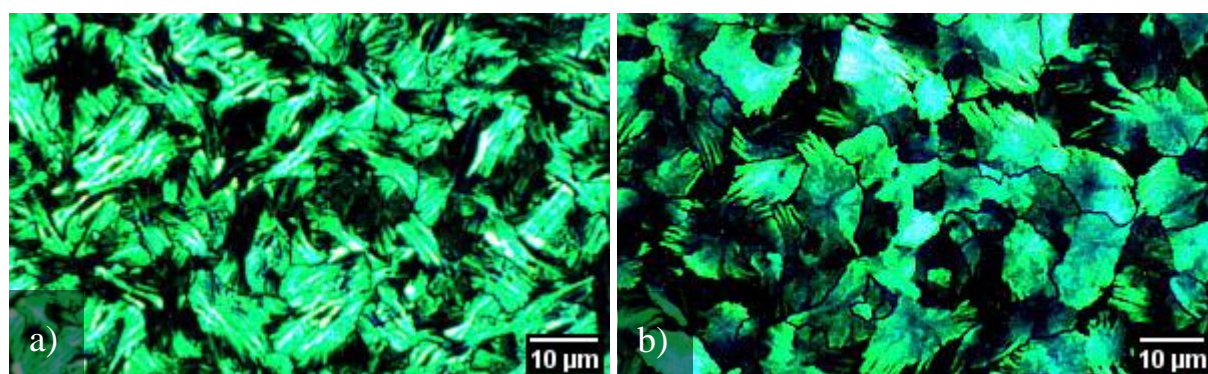


Figure 4.6 POM images (90° polarisation) of films bar coated from [5]Ph:PMMA (1:1, 10 g/l in 1,2-DCB) solutions **a)** at 60 °C and **b)** at 80 °C.

As for [5]Ph:PS, tests were only conducted at 60 °C and 80 °C, since it was clear that 110 °C was an excessive temperature for depositing [5]Ph-based solutions, at that point. Deposition conditions were identical to the tests carried out on [5]Ph:PMMA.

At 60 °C (Figure 4.7(a)), randomly oriented thin structures were embedded in an amorphous matrix. On the other hand, which packing became more compact in samples deposited at 80 °C, like shown by Figure 4.7(b): there was a remarkable variability in the sizing of the structures, but overall the amorphous regions were reduced, and the sheaves of fibres increased in size.

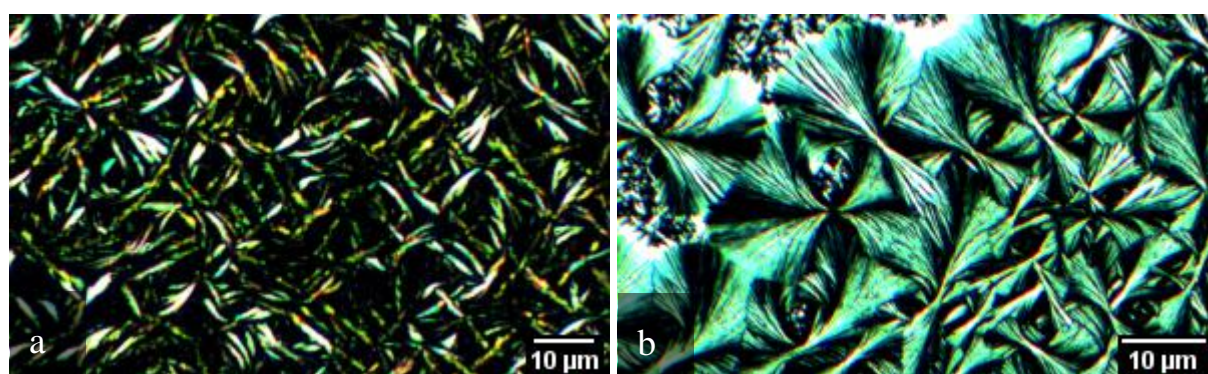


Figure 4.7 POM images (90° polarisation) of films bar coated from [5]Ph:PS (1:1, 10 g/l in 1,2-DCB) at **a)** 60 °C and **b)** 80 °C.

4.1.3 Nitrogen flow

Crystallisation is a process heavily dependent on kinetics and thermodynamics [67].

Also post-deposition treatments are important for controlling the structural and charge transport properties of organic semiconductors films. We decided not to anneal the films, both regarding [3]Ph and [5]Ph, because it increases the risk of thermal degradation, as demonstrated in Chapter 5.

Still, regarding the deposition of [3]Ph, it was noticed that fluxing N₂ onto the films, immediately after the passage of the bar, reduces the drying time of the films. This resulted in more homogenous films, as testified by lower statistical variability in the performance of transistors based on films deposited with the same conditions. Furthermore, we might speculate that N₂ flow "freezes" the film in a favourable out-of-equilibrium structure, since it accelerates the solvent evaporation.

The same strategy was attempted during [5]Ph bar coating. It turned out that the N₂ flow had a detrimental effect on [5]Ph films formation, since this material has a different crystallisation kinetics.

It happened consistently throughout the tests, carried out on different solutions, deposition temperatures and bar speed, that N₂ flow led to more isolated structures, which are not efficient at transporting charge.

The consistency of the results was such that optimised [5]Ph is now deposited without N₂ flow on.

4.1.4 Bar parameters

Bar parameters turned out to be less relevant, with respect to the above-mentioned ones.

Bar speed of 0.5 mm/s, 15 mm/s, 20 mm/s, 30 mm/s, 45 mm/s, 60 mm/s were tested. Once all the other parameters were fixed, there were not remarkable differences in the morphology among samples deposited at different speed, except for the trials at 0.5 mm/s, which were not successful: at room temperature, crystallisation kinetics is too slow, at higher temperatures the solvent evaporates before the bar coating step is completed.

45 mm/s was selected as best speed, since a quicker deposition reduces the time that the samples spend on the heating plate of the bar coater. Higher bar speeds resulted in too thick films, in accordance with the speed-thickness relation explained in Section 3.2.2, and less desirable morphologies. Indeed, the best transistors so far were fabricated by bar coating [5]Ph at 45 mm/s (Chapter 6).

4.2 Thin film characterisation

Thanks to the strong birefringence of films of cumulenes, polarised optical microscopy is a valuable and rapid tool to qualitatively assess the film formation and its morphological characteristics (for instance the size and shape of crystalline grains) as discussed in the previous section. However, its resolving power is limited, and only the surface can be observed. Hence, other techniques, such as UV-Vis spectroscopy, Atomic Force Microscopy, and Ultraviolet Photoemission Spectroscopy, were employed to get insights on degradation symptoms, electronic transitions, surface topography, film thickness, and energy levels.

4.2.1 UV-Vis spectroscopy

At first, UV-Vis spectra of [5]Ph were acquired on 0,01 g/l in 1,2-DCB solutions, as shown in Figure 4.8. At this level of dilution, it is reasonable to exclude the presence of aggregates in the solution. Therefore, this measure is regarded as the absorption spectrum of isolated molecules.

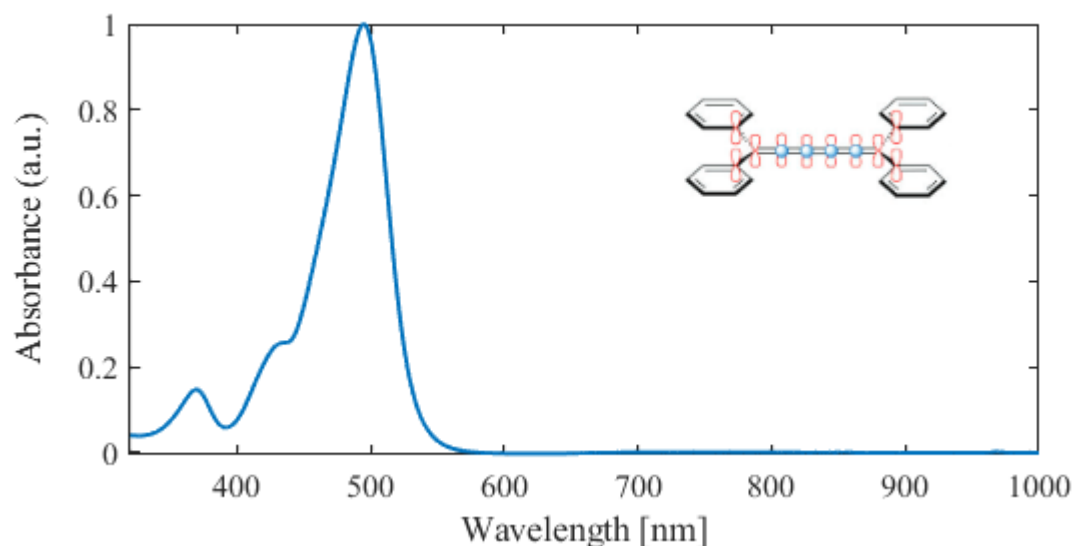


Figure 4.8 Absorption spectrum of a [5]Ph solution (0,01 g/l in 1,2-DCB). The inset, from [16], represents the molecular orbitals of [5]Ph, specifically its two π -systems.

The absorption spectrum is in perfect agreement with previous reports [33].

We can distinguish three main peaks, and in order to assign them to specific electronic transitions, it should be explained that [5]Ph displays two π -systems: one of them extends the conjugation from the central cumulenenic chain to the phenyl groups, lying somewhat out of the molecule plane, the other one is limited to the 4 orbitals of the cumulenenic sp-carbons. According to density functional theory (DFT) calculations, the main peak as well as the less energetic one, located at 496 nm, is associated to the HOMO (highest occupied molecular orbital) to LUMO (lowest unoccupied molecular orbital) transition, involving the first π -system. The other two, at 440 nm and 370 nm, are respectively referred to HOMO – 3 to LUMO transition, and to either HOMO – 1 to LUMO or HOMO to LUMO + 1: they are linked to transitions from the second π -system to the first one [7], [33].

Moving on to the thin film spectrum, in Figure 4.9(a) it is possible to notice the appearance of a peak at 510 nm, associated to solid state aggregates. The higher this peak with respect to the one at 475 nm, the better the film seems to be in terms of charge transport, based on experimental data. Indeed, [3]Ph thin film spectrum displays a very high solid state peak (Figure 4.9(b)).

The spectra in Figure 4.9(a) and 4.9(b) are all normalised to their maxima and the thin films were deposited according to their optimised conditions: both from 10 g/l in 1,2-DCB solutions, in a yellow room and in air, [5]Ph at 70 °C, with a bar speed of 45 mm/s and no nitrogen flow

on, [3]Ph at 80 °C, with 30 mm/s of bar speed and nitrogen flow on. [5]Ph solution was stirred at 35 °C for half an hour, while [3]Ph at 50 °C for a couple of hours.

It is interesting to notice that the [5]Ph thin film spectrum red shifts less, in comparison to its solution spectrum, than [3]Ph.

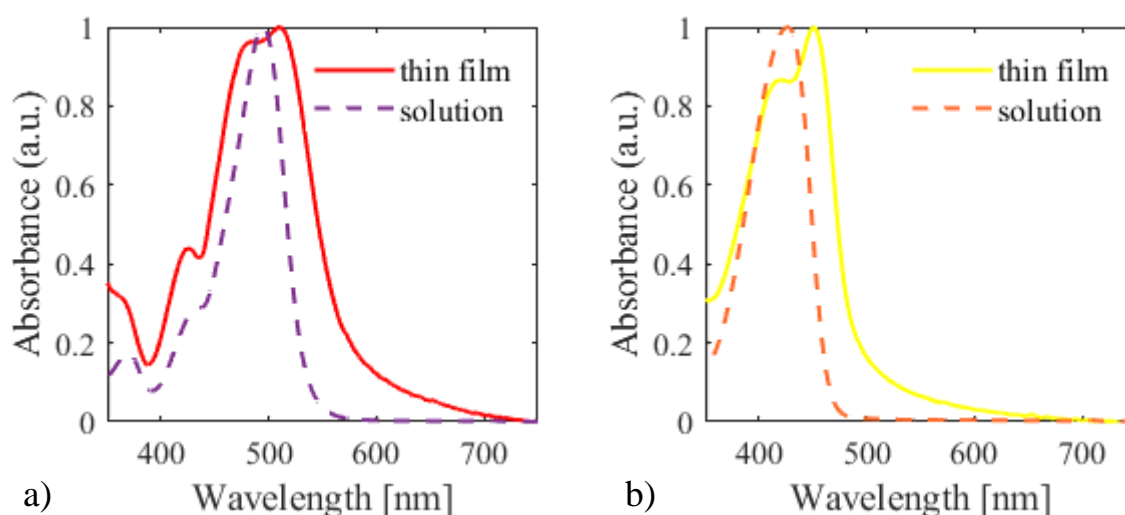


Figure 4.9 a) Absorption spectra of [5]Ph in optimised thin film and in solution (0,01 g/l in 1,2-DCB), each normalised to their maxima. b) Absorption spectra of [3]Ph in optimised thin film and in solution (0,01 g/l in 1,2-DCB), each normalised to their maxima.

Absorption spectra were mainly employed to check for degradation in films and solutions for both [5]Ph and [3]Ph, since a decreased intensity of the peaks or alterations in the spectrum shape can be interpreted as transformations in the material.

4.2.2 Atomic force microscopy

AFM was employed to analyse the surface of the samples, to extract the roughness, as well as to measure the thickness of the films.

As already mentioned, a smooth surface with low amount of defects leads to optimal conformal adhesion of the dielectric layer in TGBC devices, which reduces the presence of traps at the interface. A high degree of energetic and structural order of the film is beneficial to charge transport.

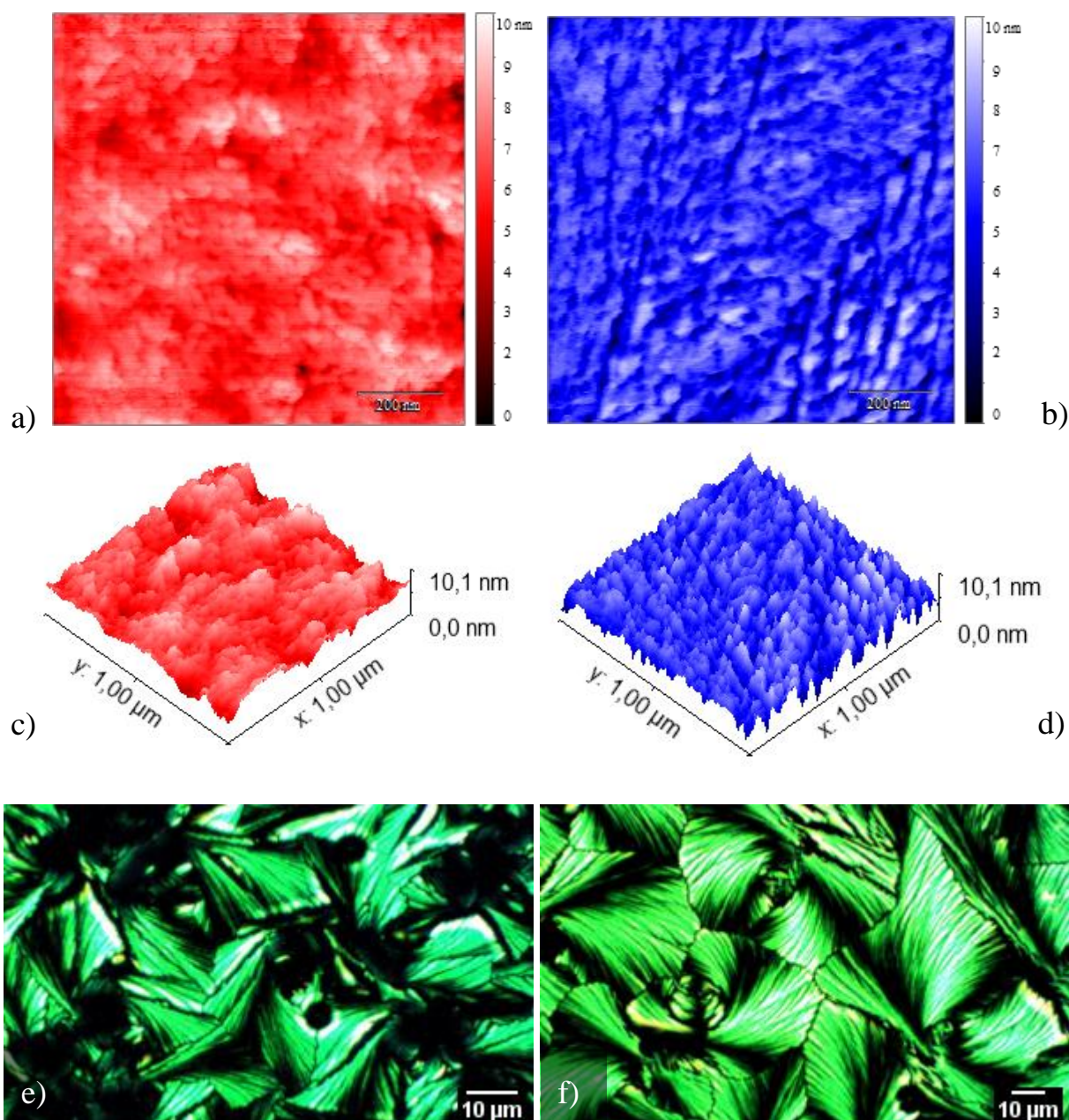


Figure 4.10 AFM 2D images of [5]Ph films, bar coated from a 10 g/l solution in 1,2-DCB, at 70 °C, in dark conditions, without nitrogen flow, in air **a)** at bar speed equal to 15 mm/s, and **b)** at bar speed equal to 45 mm/s. **c)** AFM 3D image of the same sample as **a)**. **d)** AFM 3D image of the same sample as **b)**. **e)** POM image of the same sample as **a)**-**c)**, taken under 90° polarisation. **f)** POM image of the same sample as **b)**-**d)**, taken under 90° polarisation.

Figure 4.10(a)-(b) depict AFM topographic images of two samples, that were bar coated at the same conditions, except for the bar speed: 70 °C, no nitrogen flow, in dark conditions, in air, from 10 g/l in 1,2-DCB solutions stirred at 35 °C for half an hour, but (a) was deposited with a bar speed equal to 15 mm/s, while (b) was deposited at 45 mm/s. Provided that each sample

was fairly homogeneous across its surface, it is possible to notice a difference in the topography, as (b) showed much more asperities, even though the height range of the features was exactly the same. In a way, the samples bar coated at a faster speed displayed more ordered asperities, as underlined by figures 4.9(c)-(d), which are the 3D image respectively referred to (a) and (b). As a reference, figures 4.9(e)-(f) are POM images of the very same samples, taken under 90° polarisation.

The 15 mm/s sample showed a smoother texture, as its root mean square roughness (RMS) is equal to 0,997 nm, while the 45 mm/s sample stands at 1,211 nm. Overall, it is fair to conclude that [5]Ph samples are sufficiently smooth, since their RMS roughness is comparable to those of optimised [3]Ph [13].

AFM was also employed to esteem the thickness of [5]Ph films. In order to do so, a film was bar coated at 80 °C: the structures at that specific temperature are quite similar to those forming at 70 °C, but some defects are more common at a higher temperature. These defects were exploited as indentations in the film, without having to manually scratch the sample, which would have led to accumulation of material at the edges of said scratch.

The other deposition conditions were kept identical, so 45 mm/s of bar speed, no nitrogen flow, dark conditions, air atmosphere. It is established that the bar speed is the main parameter that determines the film thickness.

Figures 4.10(a)-(b), respectively 2D and 3D images obtained by AFM, show the results of the test: the measured film had a thickness of about 20 nm. As a matter of fact, mechanical profilometry was not able to reliably measure the thickness of [5]Ph films, given the limited spatial resolution of this technique. In addition, [3]Ph films also show comparable thicknesses, ranging from 15 nm up to 30 nm [13].

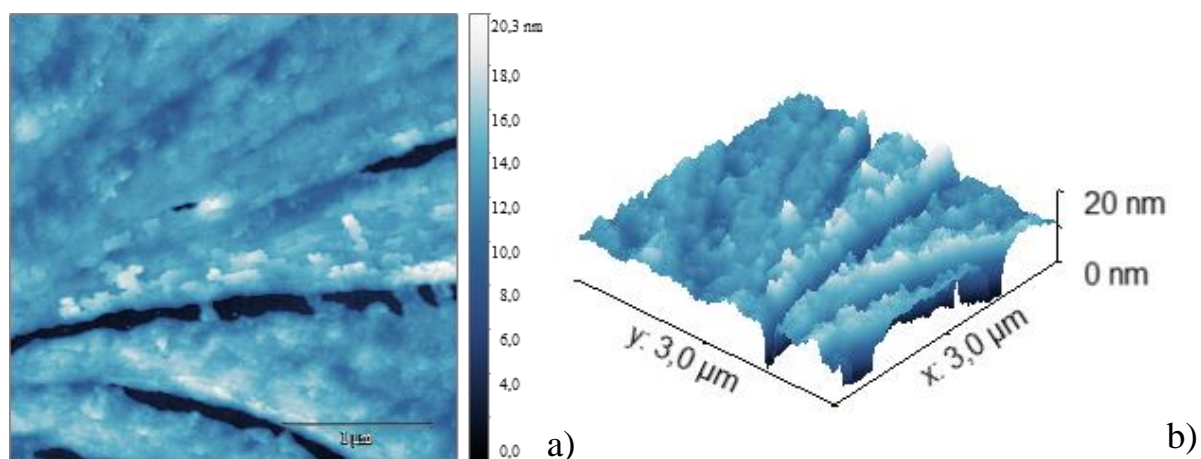


Figure 4.11 AFM images of a [5]Ph film, bar coated at 80 °C, 45 mm/s, in dark conditions, in air: a) 2D and b) 3D.

4.2.3 Ultraviolet photoelectron spectroscopy

Ultraviolet Photoelectron Spectroscopy (UPS) is a widely employed technique to extract the work function and the HOMO of materials [68]

Briefly, its working principle is based on the photoelectric effect, induced in the analyte by ultraviolet radiation. The radiation is typically generated by gas discharge, and the most common gas employed is helium, emitting photons with 21.2 eV of energy. When the radiation hits the sample, electrons are emitted. Resolutions of 0.1 eV can be achieved. This technique is suitable for valence band only. Indeed, core levels would require higher energy photons (x-rays), while the conduction band can be probed by inverse photoemission spectroscopy (IPES).

Before getting to the analysis discussion, it is worth explaining a few terms. Figure 4.12(a) is a graphic representation of the band structure of a semiconductor. For intrinsic semiconductors (excluding doping effects), the Fermi level can be assumed to lie right in the middle of the energy gap, which is the gap between the HOMO and the LUMO in organic materials. In particular, it has been proved that the single-molecule conductance of [5]cumulenes (and [3]cumulenes) is weakly dependent on the applied voltage, meaning that the Fermi level is likely far from any molecular level; from this, it is possible to infer that the Fermi level lies in between the HOMO and the LUMO [30]. The work function is the energy required to draw an electron from a solid and take it infinitely far away from it (the vacuum level), while the binding energy is the energy needed to extract an electron from its state.

For UPS analysis, samples were prepared by wire-bar coating a 10 g/l [5]Ph solution at 80 °C, at 20 mm/s, with nitrogen flow off, in dark conditions, in air, after 30 minutes of stirring at 35 °C, onto silicon substrates. Then, the samples were shipped at the Materials Characterization Facility of the Istituto Italiano di Tecnologia in Genoa, where Dr. Mirko Prato run the UPS analysis.

Figure 4.12(b) displays the resulting UPS spectrum, binding energy vs detected intensity, and we are assuming that 0 eV corresponds to the Fermi level. The high binding energy onset is at 16.8 eV: by subtracting this value from the incoming photon energy (21.2 eV), a work function of 4.4 eV is obtained. The low binding energy onset is at 1,0 eV: by combining this value with the work function, a HOMO equal to -5.4 eV is calculated. In comparison with [3]Ph, whose HOMO sits at -5.3 eV, [5]Ph has a deeper HOMO, suggesting that it might be less prone to oxidation. In addition, by assuming that the Fermi level lies right in the middle of the HOMO-LUMO gap, it is possible to evaluate the energy gap as equal to 2.0 eV.

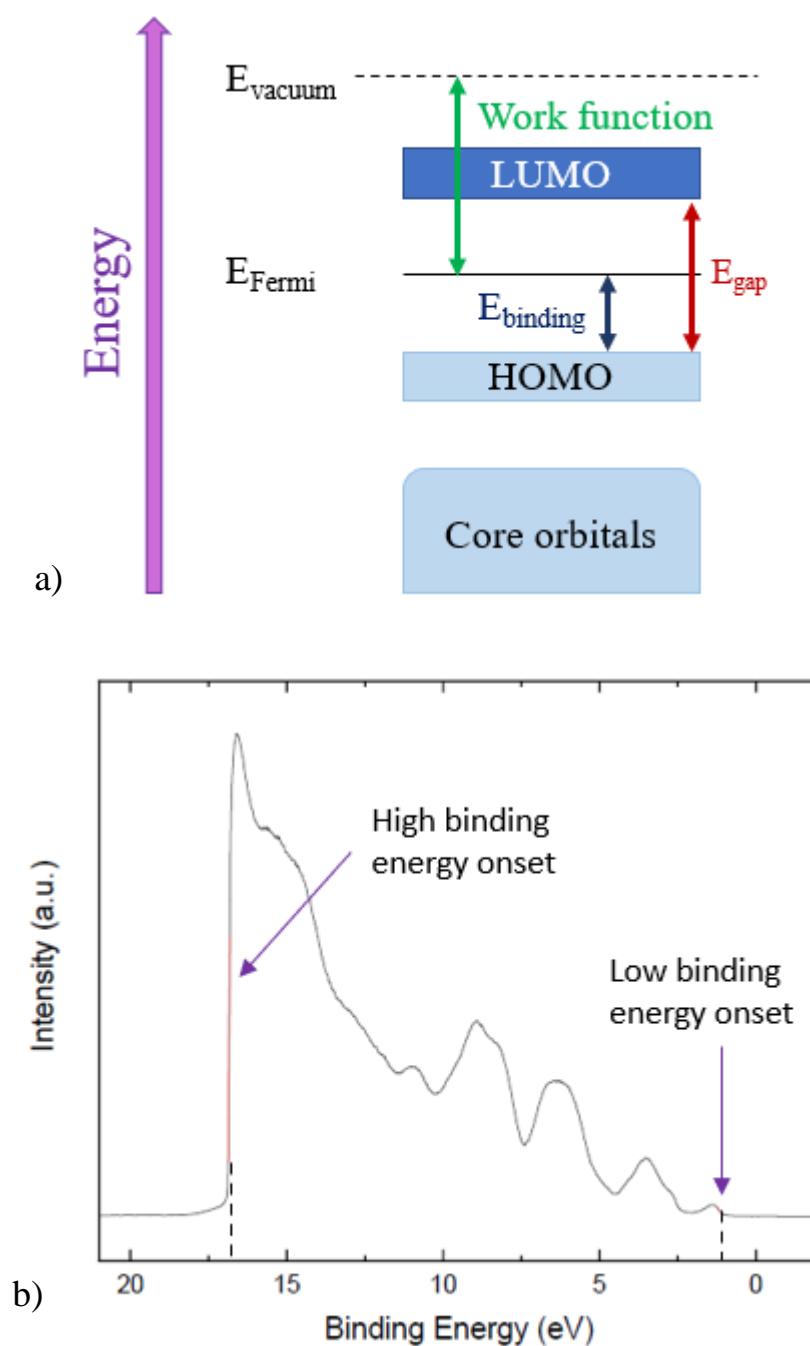


Figure 4.12 a) Band structure diagram, representing the values extracted by UPS analysis. b) UPS spectrum acquired on [5]Ph film by Mirko Prato, at MCF@IIT.

By looking at the UV-Vis absorption spectrum in figure 4.12, the value of the absorption onset can be extracted at 2.16 eV (575 nm), although the shallow slope of the curve does not allow a precise evaluation of it.

Supposing that 2.16 eV is a correct estimate, it represents the optical gap, which is the minimum energy for a photon to be absorbed.

The discrepancy between the electronic band gap, at 2 eV, and the optical band gap is apparent. This is not uncommon in organic semiconductors, but more studies are needed to properly understand the behaviour of [5]Ph in regard to transitions and band structure.

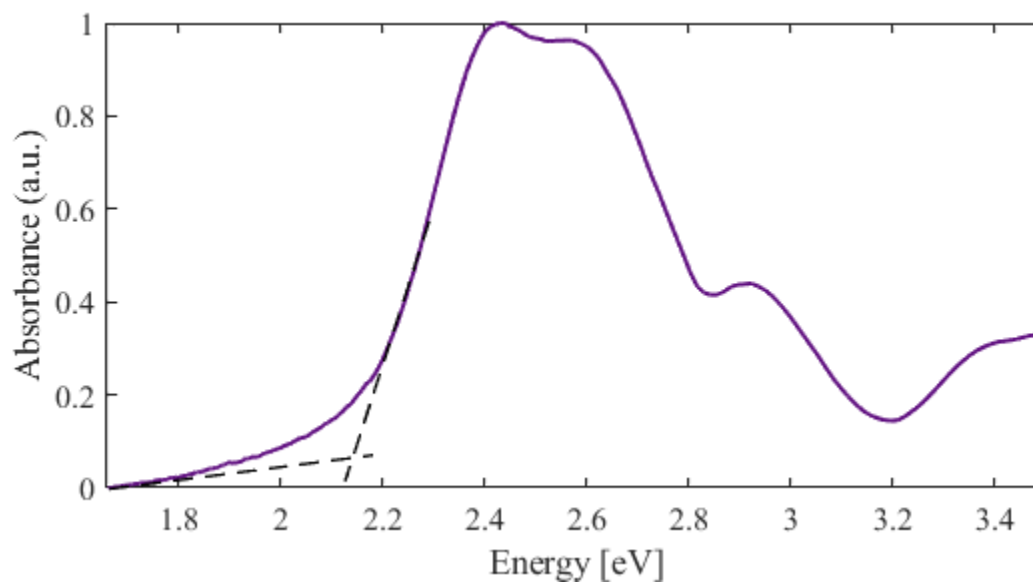


Figure 4.13 UV-Vis absorption spectrum of an optimised [5]Ph film, showing the onset of the peak associated to the HOMO-LUMO transition.

5. EXPERIMENTAL RESULTS – STABILITY

As mentioned in previous chapters, stability is a concern when it comes to cumulenic structures. The sp hybridisation is not an energetically favourable state for carbon, with respect to sp^2 or sp^3 , so it was crucial to establish the conditions that could allow to work with [3]Ph and [5]Ph without incurring into degradation issues. It was soon apparent that, as similar as these two molecules are to each other in terms of chemical structure, they display different behaviour in relation to certain stimuli.

A series of experiments was set-up to isolate the impact of light and heat on the degradation of cumulenes in solution and in thin-film. Photospectroscopy was the principal technique employed to characterise the samples.

5.1 Stability in air and ageing

[3]Ph and [5]Ph powders are considered stable in air. Solutions are prepared in air and thin film deposition by wire-bar coating is also carried out in air.

However, degradation of [5]Ph solutions (in 1,2-DCB and in toluene) was observed over a few days long period of time, even when those were exposed to neither light nor heat, except for the initial stirring step at 35°C or 40°C for 30 to 60 minutes.

Figure 5.1(a) shows the results of two absorption measurements run on a 0,01 g/l [5]Ph in DCB solution, 10 days apart from each other: the main peak, located at 495 nm, of the absorbance spectrum clearly decreases in intensity, while the higher energy peak at 370 nm, which might be linked to degradation, stays the same, meaning that it increases in comparison to the main peak. On top of that, optical microscopy reveals that the old solution is not able to deposit a good, homogeneous film (Figure 5.1(b)). It should be underlined that during those 10 days the solution was kept in the dark in a fridge at 4°C.

Although more tests should be conducted to properly assess the origin of this degradation process, it is possible that air might have something to do with it, as oxygen and moisture are known to promote (electro)chemical reaction, so degradation, of OSCs.

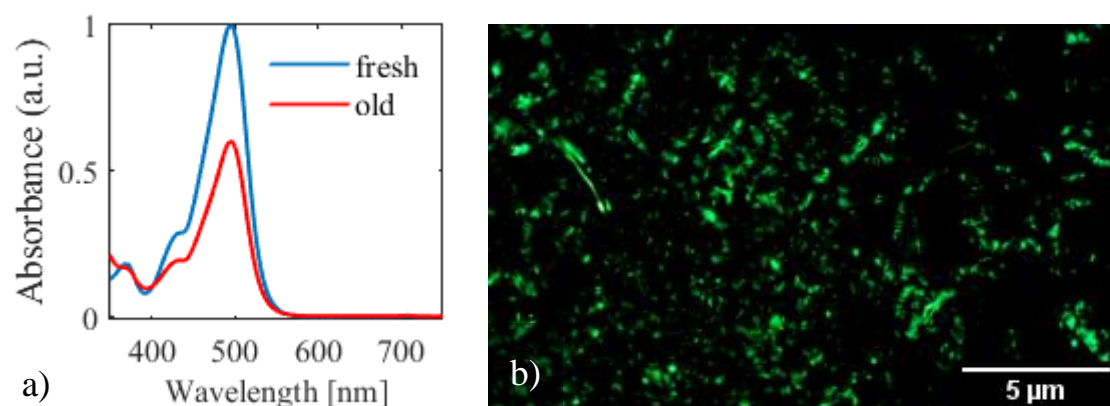


Figure 5.1 a) UV-Vis absorbance spectra of a [5]Ph in 1,2-DCB solution (0.01 g/l); the spectra are normalised to the peak of the fresh solution. b) POM picture of a thin film deposited from the old [5]Ph solution.

Thin films of [5]Ph don't seem to show this behaviour, as they remain identical even 10 days after deposition, if not exposed to light or heat. On the other hand, electrical measurements of [5]Ph-based transistors run in air return slightly decreased performance compared to measurements run in nitrogen atmosphere, but this subject will be more thoroughly explained in the next chapter.

As for [3]Ph, it doesn't seem to be affected by air, nor in solution nor in solid state, and old solutions are not degraded.

[5]Ph has a deeper HOMO level than [3]Ph, so it is supposed to endure better against oxidation, but more tests are needed before drawing any conclusions.

5.2 Photosensitivity

The photosensitivity of [3]Ph and [5]Ph is definitely one of the major challenges faced when studying these molecules – even more so when fabricating transistors based on cumulenes. The aim of the following tests was to quantify the impact of photodegradation on these materials.

5.2.1 Photosensitivity in solution

The experiments were run according to identical methodology for both [3]Ph and [5]Ph. Both materials were dissolved in 1,2-Dichlorobenzene, at a concentration of 0,01 g/l to compensate the low sensitivity of the detector, which cannot efficiently collect the signal if the sample absorbs too many photons. The quartz cuvettes employed for the measurements have a 10 mm long optical path.

Each solution underwent the same procedure according to the set-up described in Paragraph 3.3.2. White light was shined through the sample for 30 seconds, during which absorption data were acquired, to create a baseline. After that, in addition to the white light, LEDs emitting at different wavelengths, i.e. 660 nm, 530 nm, 470 nm, 405 nm, 365 nm, were shined on the sample one at a time for 30 seconds each, starting from the red one and proceeding by decreasing the emitted wavelength. Except for the white light source and the LED, no other light was on during measurements and the solutions were never exposed to heat.

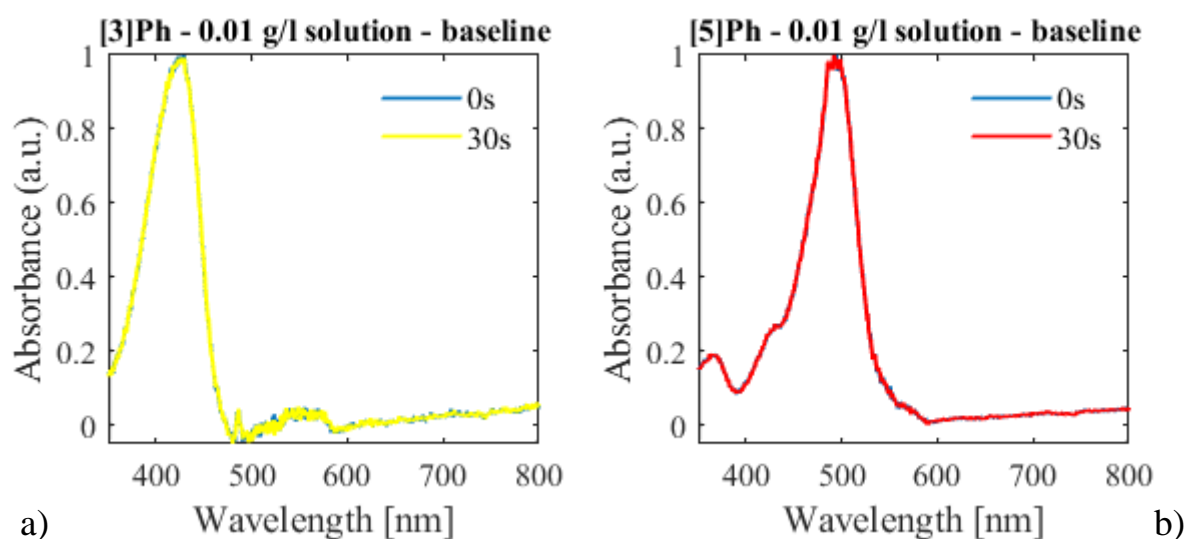


Figure 5.2 Absorbance spectra before and after 30 seconds of white light stimulation for a) [3]Ph (0.01 g/l in 1,2-DCB) solution, and b) [5]Ph (0.01 g/l in 1,2-DCB) solution.

Figure 5.2(a) and 5.2(b) show the response of the two materials to the low intensity white light. Both solutions proved to endure well this kind of light stimulation, as their absorption spectra didn't change throughout the measurement. In particular, [3]Ph and [5]Ph main peaks, at 425nm and 495nm respectively, did not change neither shape nor intensity.

Moving on to the actual test, Figure 5.4(a)-(e) show the response of the [3]Ph solution to more intense light stimulation, i.e. to LEDs, every 6 seconds up to 30 seconds. There is not any significant difference in the absorbance spectrum across the measurements, meaning that the material is not particularly photosensitive when in solution. 30 seconds under UV light (365 nm) did not affect too much the material and there is not much difference between the spectrum at the very start of the experiment, before the sample was exposed to any source of light, and the one at the end, as reported by Figure 5.4(f).

Some minor differences in the spectra can be noticed in the near-Infrared, but it could be due to background noise.

As for [5]Ph, Figure 5.5(a)-(e) showcase the effect of the LEDs on the solution. The interval associated to 470 nm light seems to have affected the material the most, which could be explained by the fact that the material absorption peak is at 495 nm, meaning that [5]Ph absorbs the most photons at that wavelength. However, in the next spectra that variation appears recovered. In fact, Figure 5.55(e) proves that there is little to no difference in the absorbance spectra before and after the whole experiment, so it can be speculated that the fluctuations in the spectra in Figure 5.5(c) might be due to external noise.

Overall, we can conclude that [3]Ph and [5]Ph in solution display a similar behaviour, regarding to light, as visible from Figure 5.3. [5]Ph absorbs slightly more in the visible, but it is less affected by UV light.

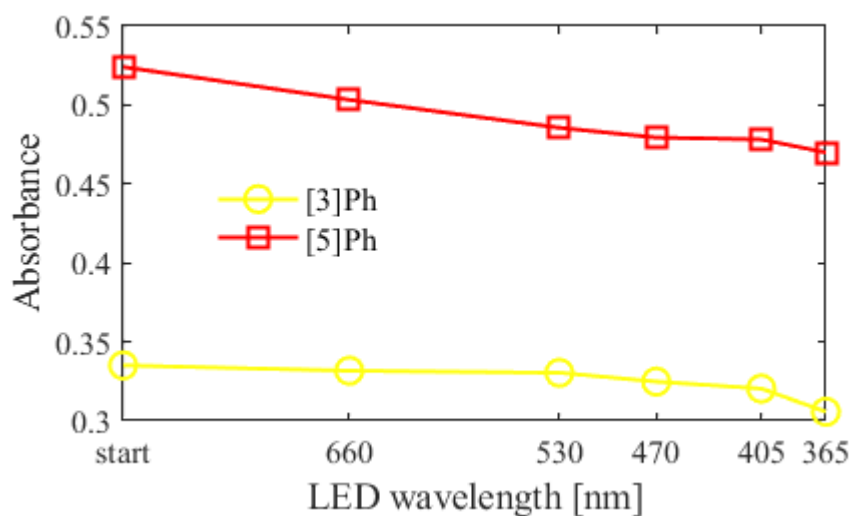


Figure 5.3 Trend of the absorption peak of [3]Ph and [5]Ph 0.01 g/l solutions during the test at different wavelengths.

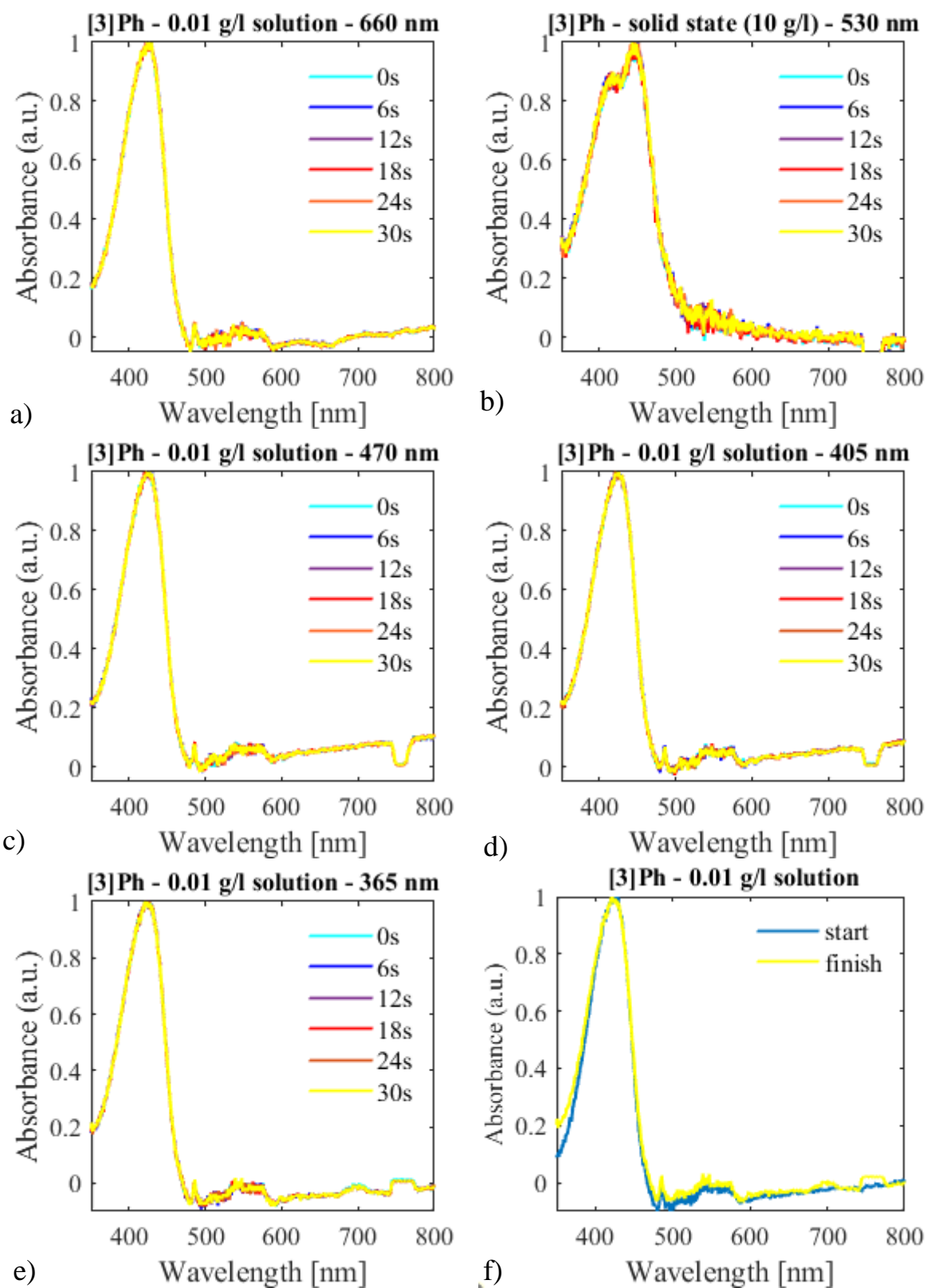


Figure 5.4 a-e) Absorbance spectra of the [5]Ph solution (0.01 g/l in 1,2-DCB) during 30-second long intervals of irradiation at 660 nm, 530 nm, 470 nm, 405 nm, 365 nm. **f)** Absorbance spectrum before and after the test.

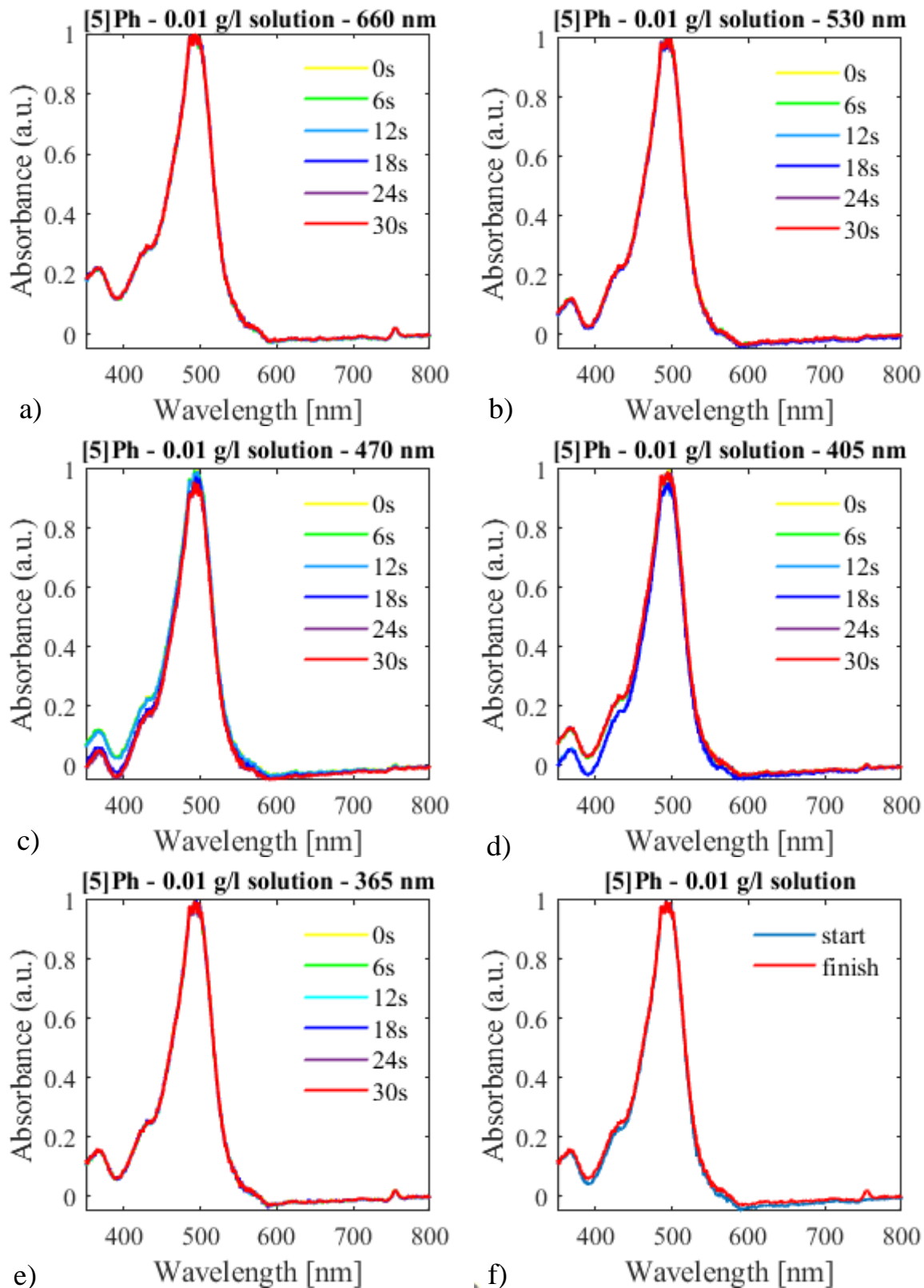


Figure 5.5 a-e) Absorbance spectra of the [5]Ph solution (0.01 g/l in 1,2-DCB) during 30-second long intervals of irradiation at 660 nm, 530 nm, 470 nm, 405 nm, 365 nm. **f)** Absorbance spectrum before and after the test.

5.2.2 Photosensitivity in solid state

Samples were prepared by bar coating previously stirred 10 g/l solutions of [3]Ph and [5]Ph in 1,2-DCB onto clean corning glass right before the photosensitivity tests. For [3]Ph, deposition conditions were the following: plate temperature at 80 °C, bar speed at 30 mm/s, nitrogen flow on, bar groove width of 6µm. As for [5]Ph: plate temperature at 70 °C, bar speed at 45 mm/s, no nitrogen flow, bar groove width of 10 µm.

To test photosensitivity in solid state, the same set-up employed for solutions was kept, and so the experiment was carried out with the same approach as before.

A baseline was acquired by only switching on the white light source and Figure 5.6(a) and 5.6(b) show the results: again, 30 seconds of low intensity white light did not affect the two samples.

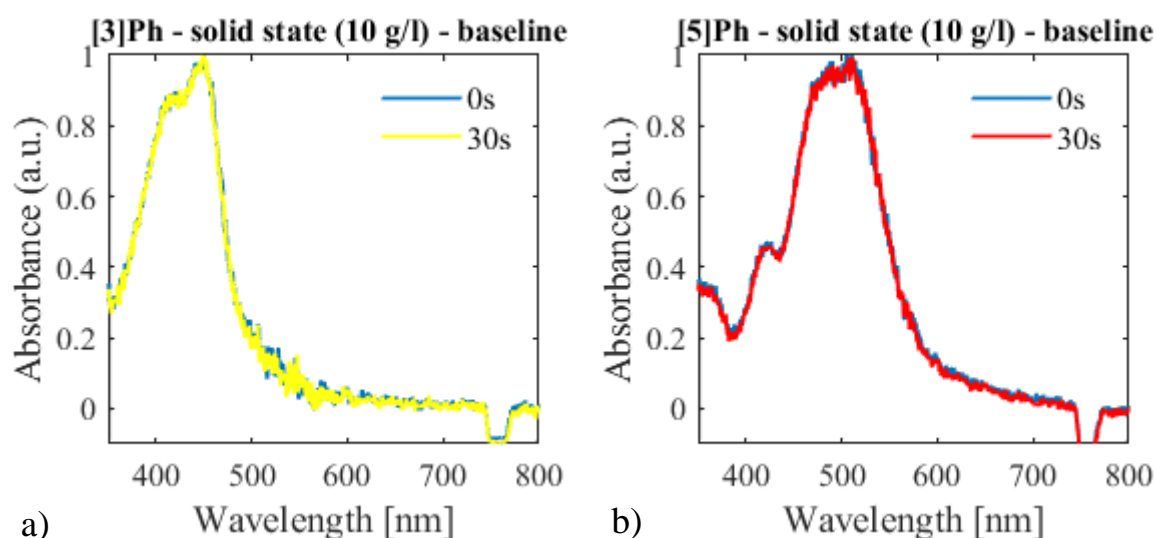


Figure 5.6 Absorbance spectra under white light of thin films of **a)** [3]Ph, and **b)** [5]Ph.

[3]Ph thin films turned out to be particularly sensitive to light, as Figure 5.8(a)-(f) prove.

The first interval under the 660 nm LED did not change much the material spectrum, but starting with the next LED, the green one, a slight decrease in the intensity of the solid state peak at 450 nm compared to the material peak at 425 nm occurred. The subsequent intervals further degraded the sample. As it was expected, the highest energy LED, emitting at 365 nm, was the one causing the most damage to the material.

[5]Ph is somewhat more resistant to light than its counterpart. Figure 5.9(a)-(f) display the results of the test, and although the solid state peak at 510 nm instantly decreased under the 530

nm LED, the overall shape and intensity of the absorbance spectrum did not change too much throughout the experiment.

It is interesting to notice that for both materials a significant amount of degradation happens immediately upon the application of the light stimulus, but it does not aggravate to much during each interval. As a result, there is not much difference between the absorbance spectra at 0 seconds and the ones at 30 seconds.

More importantly, from the results regarding solutions and solid state, we can infer that light disrupts the packing, so the arrangement in solid state, of the molecules more than it does the actual molecules.

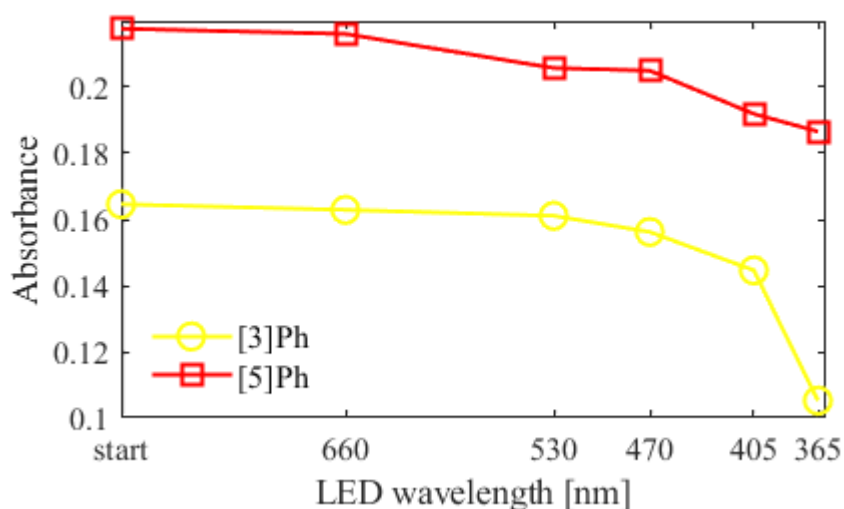


Figure 5.7 Trend of the absorption peak of [3]Ph and [5]Ph 0.01 g/l solutions during the test at different wavelengths.

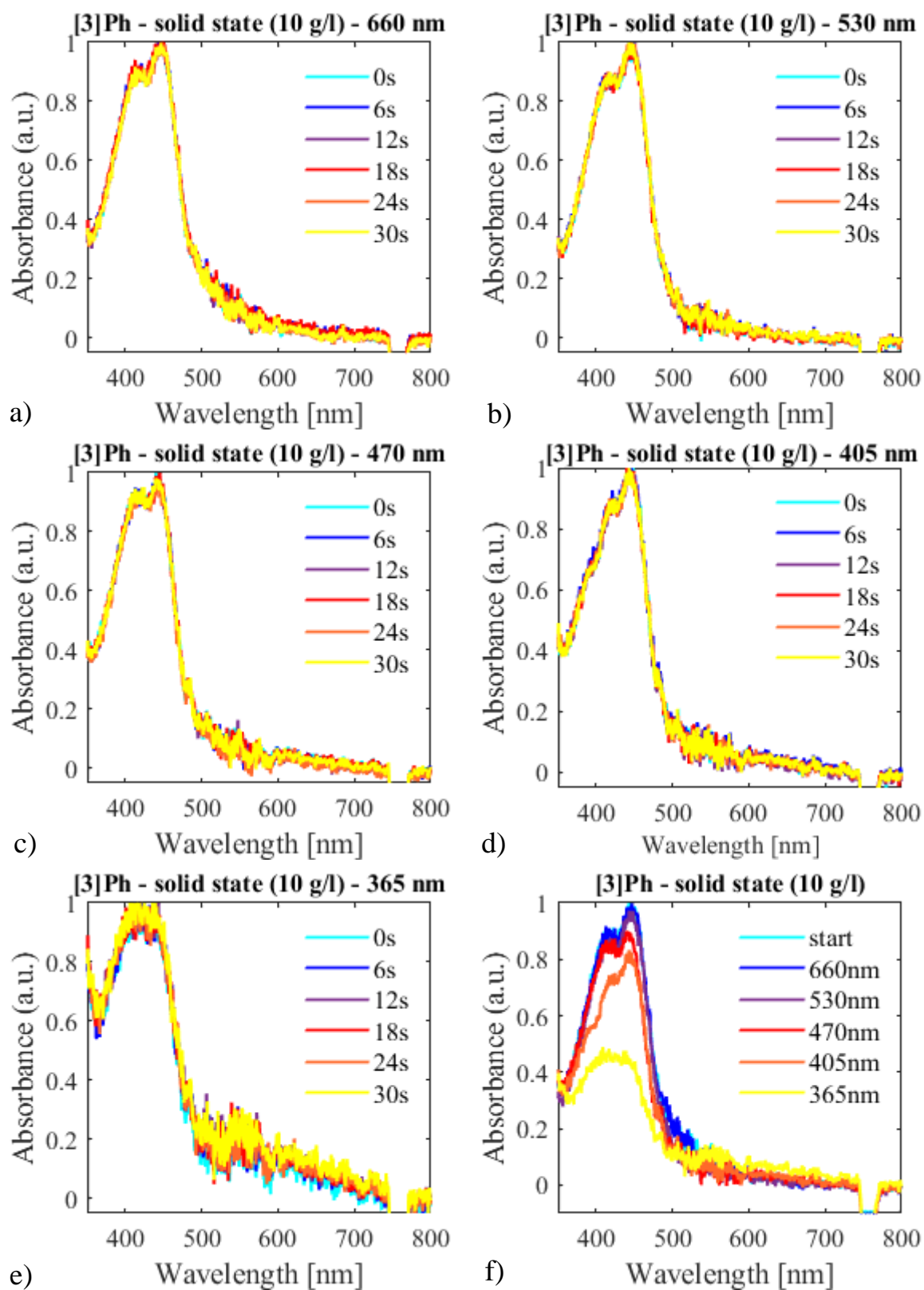


Figure 5.8 Evolution of the absorption spectrum of [3]Ph films during irradiation for 30 seconds with light having wavelength a) 660 nm, b) 530 nm, c) 470 nm, d) 405 nm, e) 365 nm. f) Absorbance spectra after each interval.

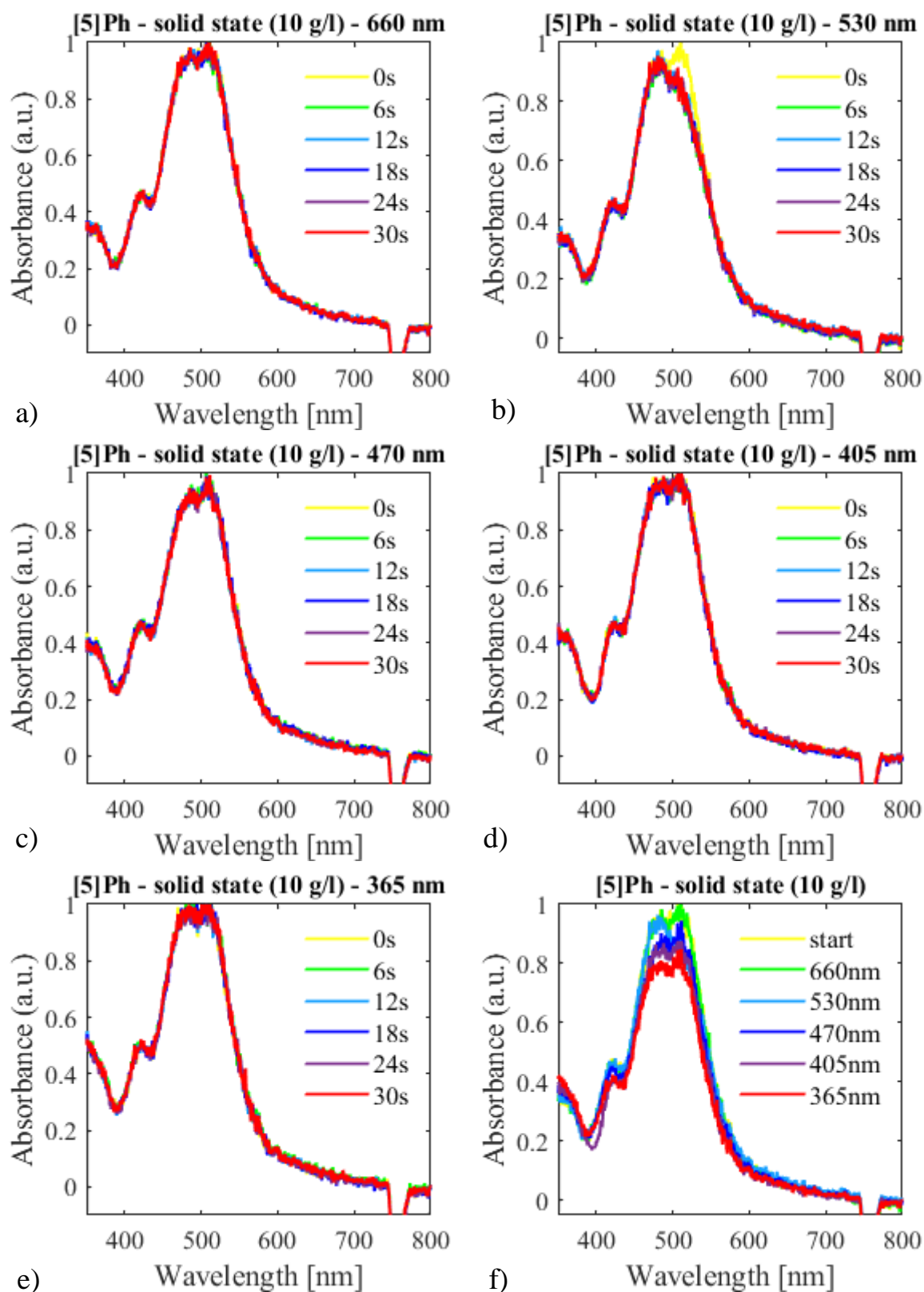


Figure 5.9 Evolution of the absorption spectrum of [5]Ph films during irradiation for 30 seconds with light having wavelength a) 660 nm, b) 530 nm, c) 470 nm, d) 405 nm, e) 365 nm. f) Absorbance spectra after each interval.

After the photosensitivity tests, the samples were observed under POM and compared to pristine samples, which were deposited with the same conditions and at the same time of the degraded ones. Figure 5.10(a)-(d) showcase the noticeable differences between the films.

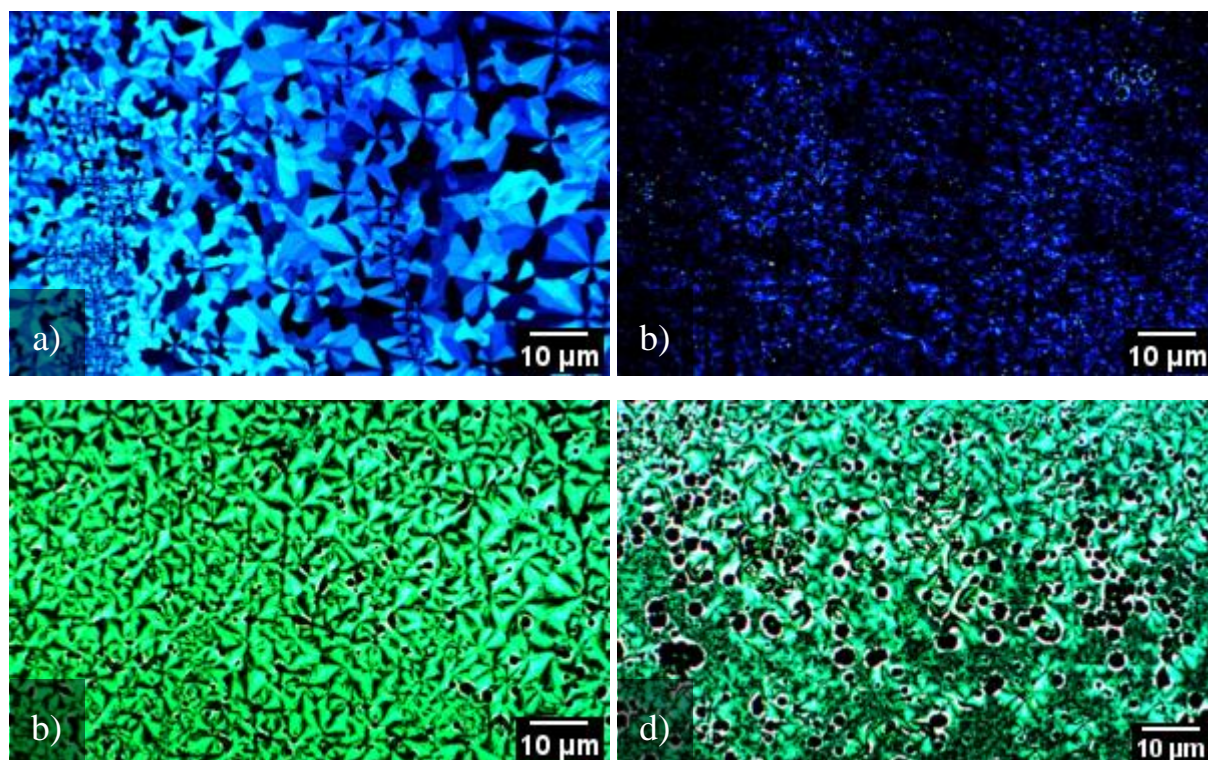


Figure 5.10 POM pictures of a),c) undegraded [3]Ph and [5]Ph, respectively, and b),d) degraded [3]Ph and [5]Ph.

Finally, both [3]Ph and [5]Ph show an increased sensitivity to light when in excited state, i.e. when passed through by current in a working transistor. A demonstration of this will be included in Chapter 6, about electrical measurements.

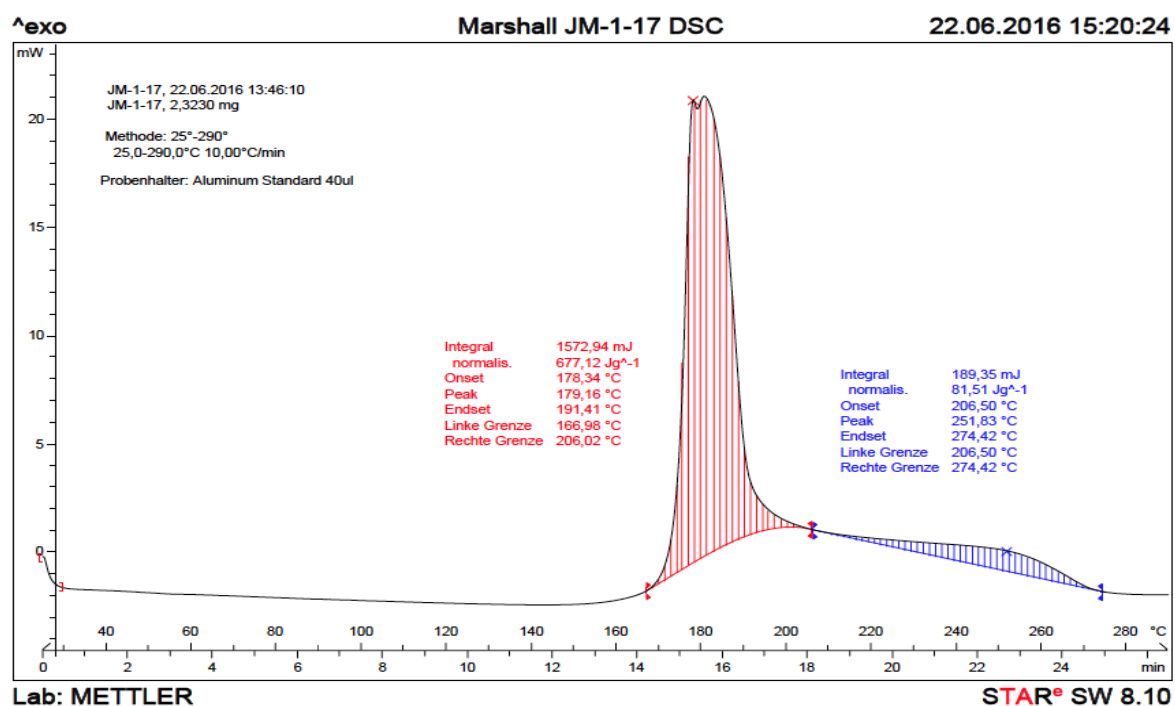
5.3 Thermostability

Before engaging in thermostability tests, the only available information regarding [3]Ph and [5]Ph thermal resistance was mainly referred to the bulk materials.

As a matter of fact, differential scanning calorimetry (DSC) revealed that [3]Ph is thermally stable up to about 250 °C [12], [13]. On the other hand, [5]Ph decomposes at 180 °C, as underlined by DSC, in Figure 5.11(a), and by ThermoGravimetric Analysis, in Figure 5.11. Both analysis were run by Prof. Rik Tykwinski and his team, at the University of Alberta.

However, dealing with solutions and thin films, signs of degradation show up way below those temperatures, especially when working with [5]Ph.

[5]Ph in organic solvents is known to cyclooligomerise at 110 °C [69], but it is entirely possible that other transformations may occur at lower temperatures, based on the very poor thermostability [5]Ph solutions demonstrate. Finding out precisely what kind of transformations take place was beyond the scope of the following thermostability tests. The main goal was to identify a safe range of temperature that would not damage these materials, ultimately to optimise charge transport properties.



a)

stayed for 30 minutes stirring on a hotplate at set temperatures: 80 °C, 100 °C, 120 °C and, for [3]Ph only, 140 °C. Figure 5.12(a) and 5.12(b) show the effect of temperature on the two materials.

Starting from [3]Ph, its signature peak at 425 nm only slightly decreases in intensity, starting from the interval at 100 °C. Besides, the interval at 120 °C seemed to slightly alter the spectrum, which then remains stable even after the last interval at 140 °C.

As for [5]Ph, its main and secondary peaks, respectively at 495 nm and 435 nm, consistently decrease in intensity, while the peak at 370 nm first decreases, then it stays stable, meaning that, proportionally to the other peaks, it actually increases. This is interesting, because the increase of higher energy peaks might be linked to the ageing of the material.

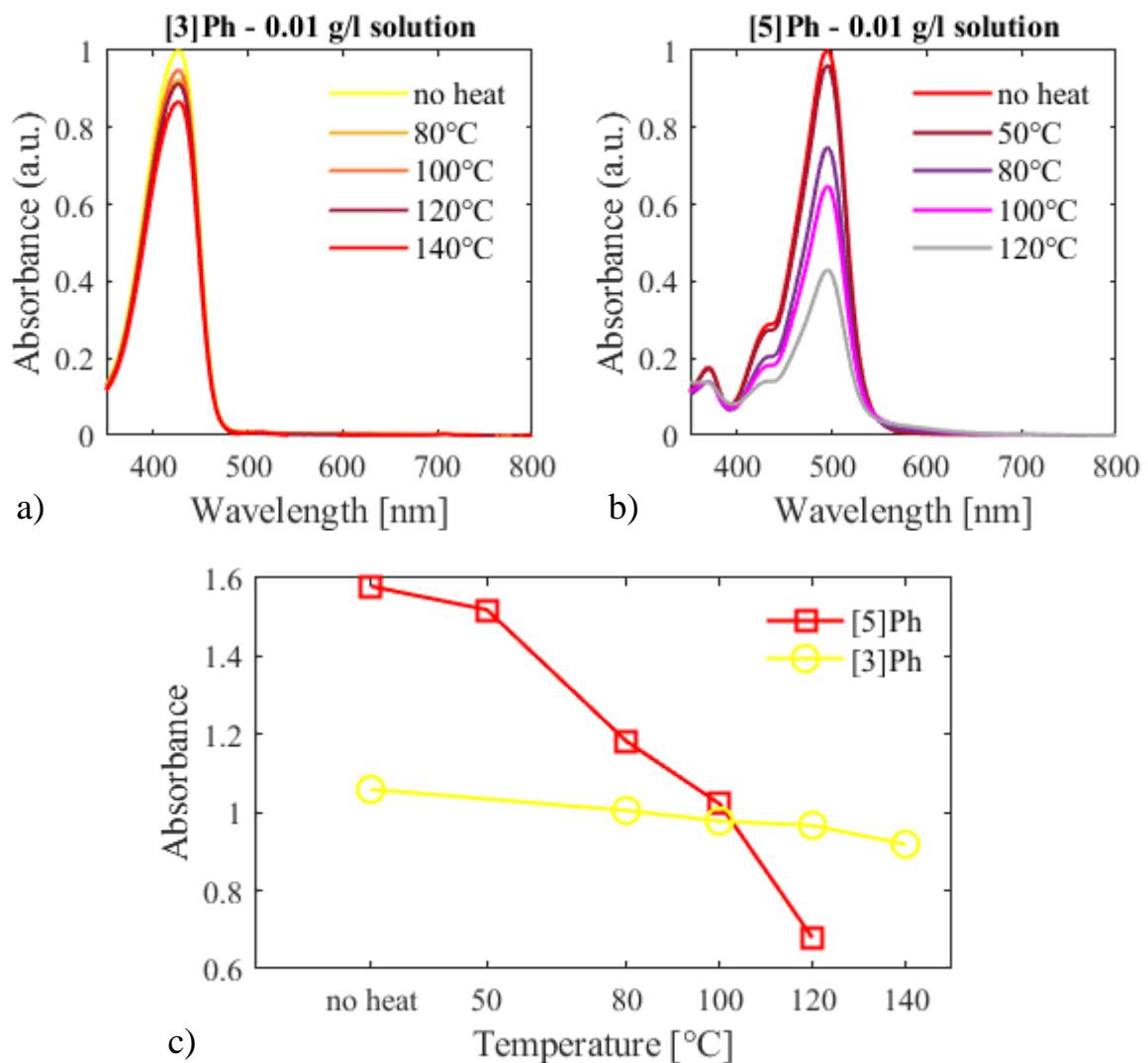


Figure 5.12 a) Evolution of [3]Ph solution absorption spectrum after 30-minute long intervals at set temperatures. b) Evolution of [5]Ph solution absorption spectrum after 30-minute long intervals at set temperatures. c)

Comparison of the trends of the absorption peak of [3]Ph and [5]Ph solutions, as they are heated at 50 °C, 80 °C, 100 °C, 120 °C, 140 °C.

Figure 5.12(c) underlines the difference in the trends of the intensity of the absorption peak for [3]Ph and [5]Ph solutions.

It is also worth noticing that the [5]Ph solution significantly shifted colour by the end of the experiment, as it got much darker, almost brownish, while [3]Ph withstood with little to no degradation even the last interval at 140 °C.

In an attempt to define a suitable temperature range for [5]Ph deposition, a further experiment was conducted on a fresh solution: a first reference measurement was carried out after the usual 30 minutes of stirring at 35 °C. Then, the sample was left stirring on a hotplate at 50 °C for 3 hours, which is regularly done with [3]Ph with no degradation effects detected. The spectra were acquired, showing that the thermal treatment significantly affected the material, as Figure 5.13(a) displays.

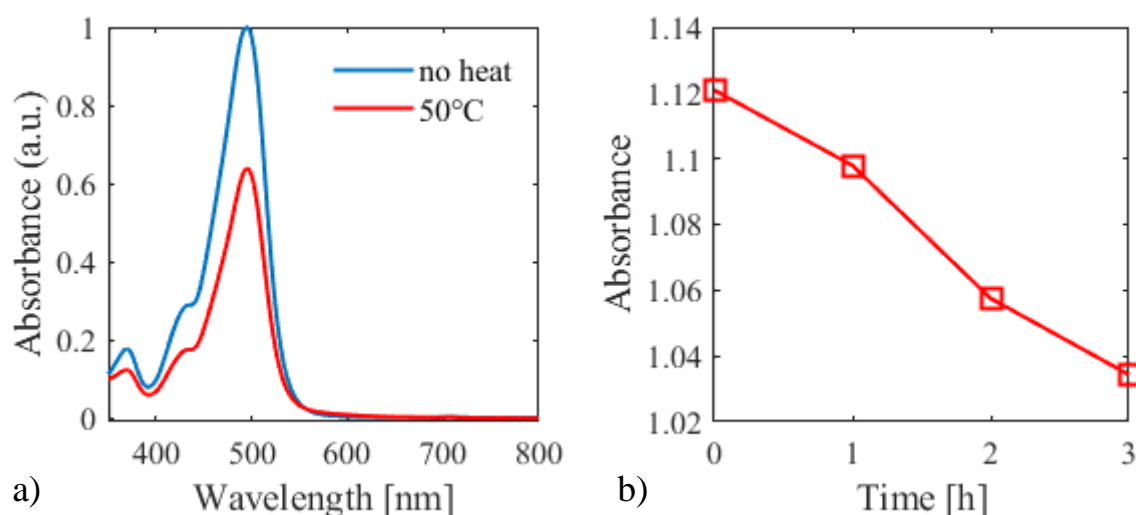


Figure 5.13 a) Evolution of [5]Ph absorption spectrum after 3 hours at 50 °C. b) Trend of [5]Ph absorption peak hour by hour when the solution is heated at 50 °C.

Furthermore, an attempt to bar coat a thin film from that same solution was made and the resulting layer wasn't as homogenous and crystalline as when deposited from a fresh solution.

To further assess the resistance of [5]Ph to heat, the previous experiment was repeated at 35 °C, with samples diluted and analysed each hour for 3 hours.

Figure 5.13(b) shows how this light thermal treatment is enough to cause some minimal alterations in the absorbance spectrum of the material. Indeed, transistors based on [5]Ph films

deposited from a solution that was left on a hot plate at 35 °C for about 5 hours displayed worse performances than others based on films bar coated from fresher solutions.

Similar experiments were not run on [3]Ph, since its solutions are stable, i.e. absorption spectrum does not change and films are formed without any issues, even when kept at 50 °C for days.

5.3.2 Thermostability in solid state

To test [3]Ph and [5]Ph thermostability in solid state, thin films of the two materials were bar coated on previously cleaned and plasma-activated corning glass, from 10 g/l solutions ([3]Ph was stirred at 50 °C for 1 hour, [5]Ph was stirred at 35 °C for half an hour). [3]Ph was bar-coated at 80 °C, with a bar-speed of 20 mm/s, and with a 6 μm bar, while [5]Ph was bar-coated at 45 mm/s, and with a 10 μm bar.

A first reference UV-Vis measurement was run for each of the two materials. Then, each sample was heated up at different temperatures for 30 minutes, in air, as that is the atmosphere the semiconductor is deposited in. The set temperatures were: 50 °C, 80 °C, 100 °C, 120 °C and, for [3]Ph alone, 140 °C. Both [5]Ph and [3]Ph, respectively at 120 °C and 140 °C, were completely melt and degraded after the 30 minute long interval, as shown by Figure 5.14(a) and 5.16(b).

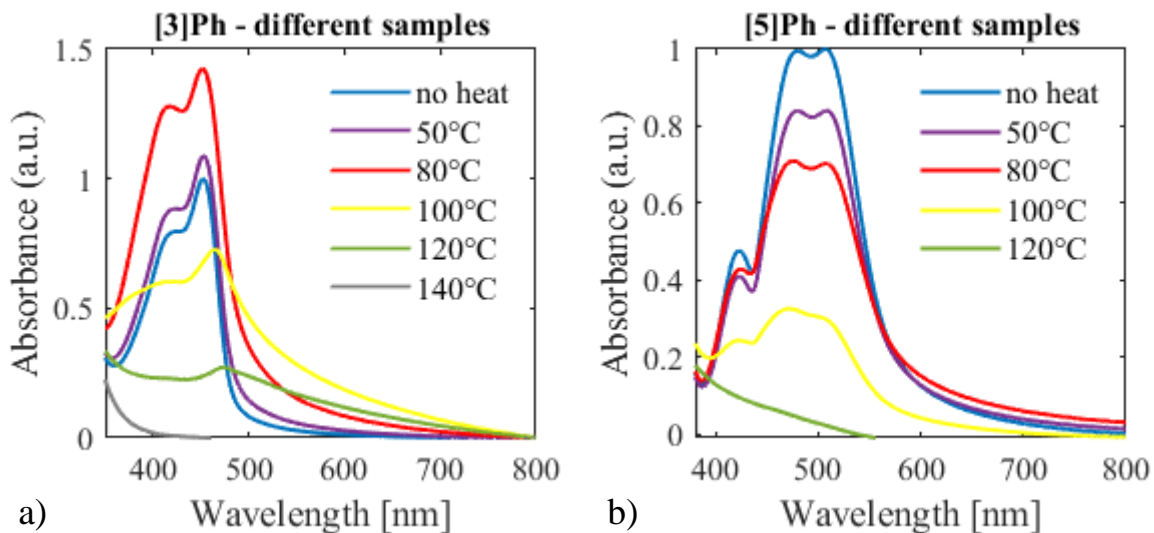
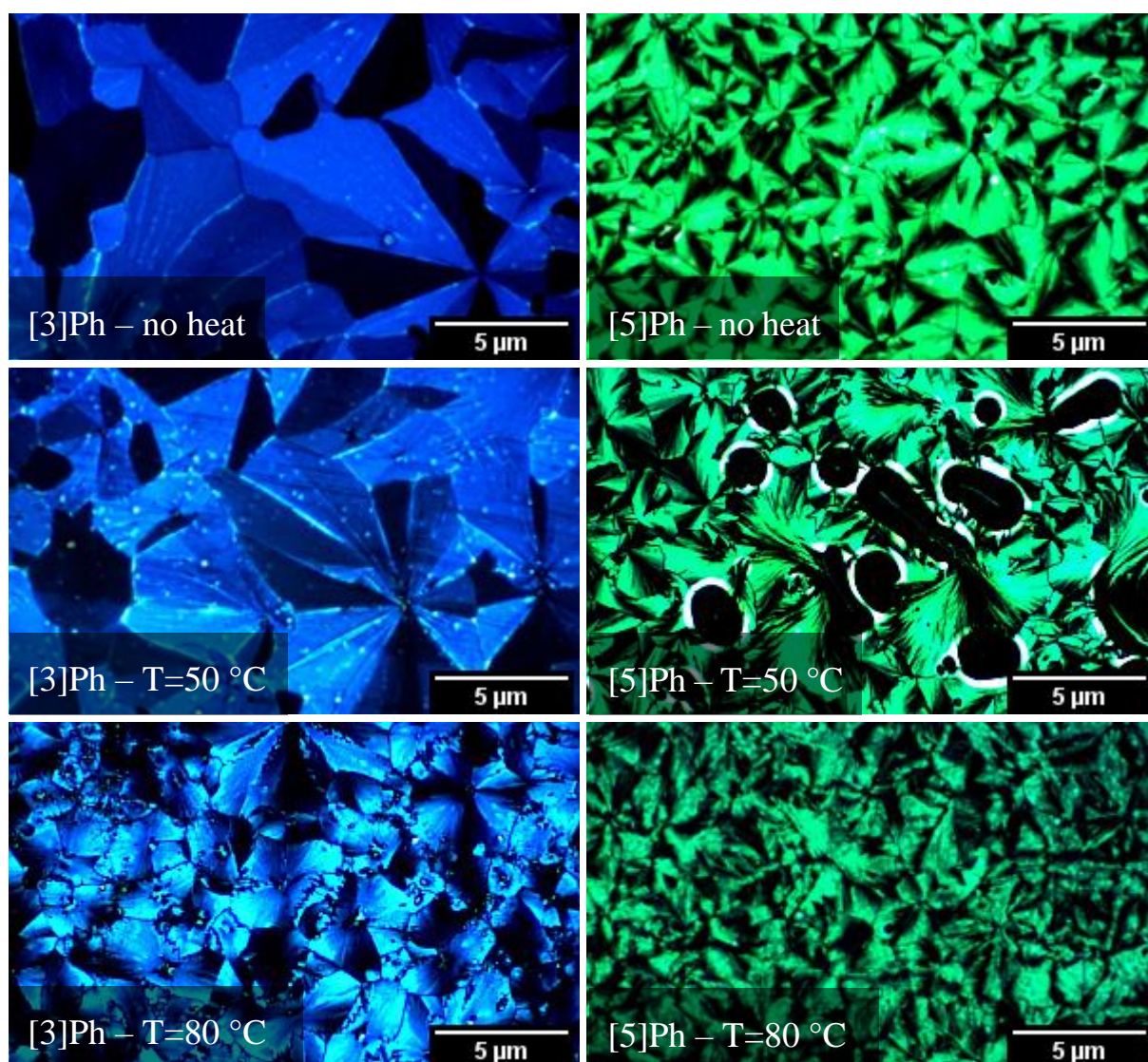


Figure 5.14 Effect of 30-minute long intervals at 50 °C, 80 °C, 100 °C, 120 °C on thin films of a) [3]Ph and b) [5]Ph, each heated at one temperature.

Each measurement was run on different samples, as previously stated, to avoid the accumulation of effects, so the upwards shift of some of the [3]Ph spectra may be due to a slightly different thickness of the film. However, the ratio of the solid state peak, at 452 nm, over the one at 420 nm, is what matters: it remains stable after 30 minutes at 50 °C, then it starts to decrease at 80 °C. At 100 °C the spectrum changes shape, at 120 °C [3]Ph peak is hardly even recognisable and after 30 minutes at 140 °C there is no trace of [3]Ph anymore.

Moving to [5]Ph, it shows thermal degradation at 50 °C already. At 120 °C, it's impossible to recognize the molecule from the spectrum.

Samples were also observed through POM to keep track of the morphology variation, like shown in Figure 5.15.



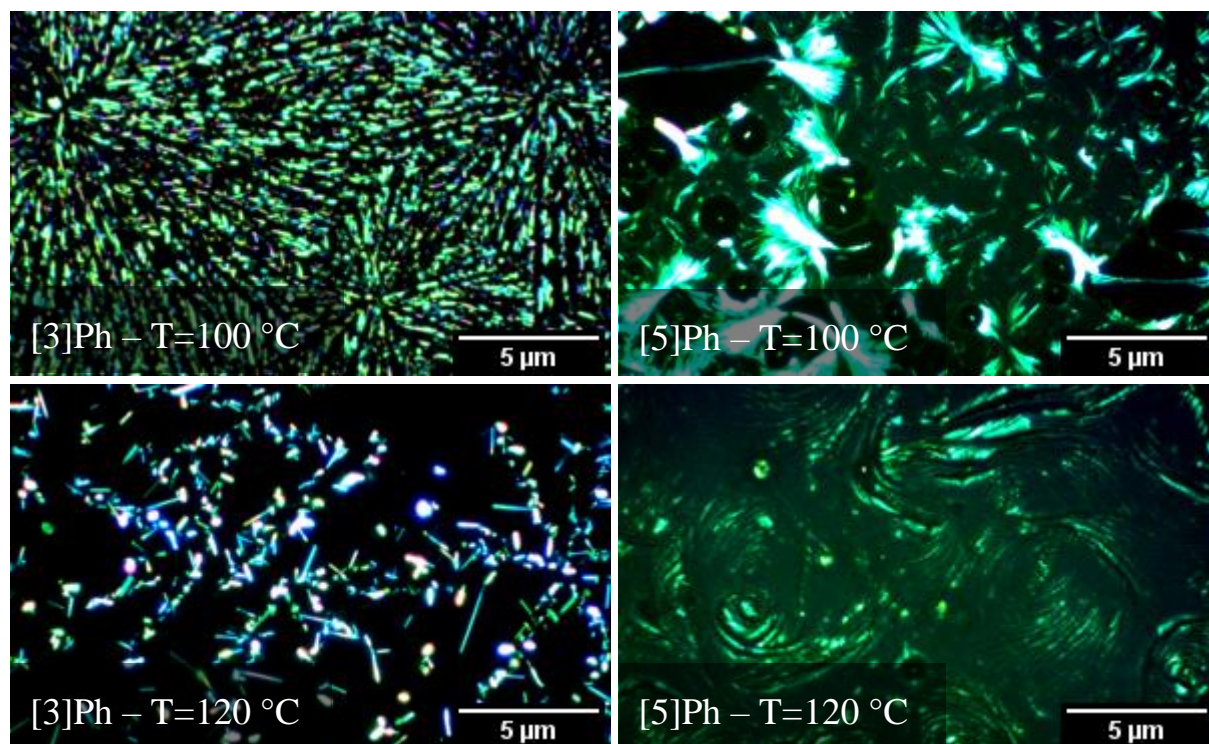


Figure 5.15 Evolution in [3]Ph and [5]Ph thin film structures, when heated up at 50 °C, 80 °C, 100 °C, 120 °C.

The previous thermostability test was repeated by heating two samples of [3]Ph and [5]Ph thin films, one each, at the different temperatures, to avoid the variable of thickness, and by scanning them by UV-Vis spectrophotometry after each step. No optical microscopy was involved to avoid any further influence on degradation coming from light.

Figures 17 a-b confirms what was observed during the tests run on different samples, which is mainly the decrease in the ratio between the two most intense peaks of the spectrum for both molecules.

[3]Ph also displays a broadening of the peaks during thermal degradation, while [5]Ph does not.

It is important to point out that the difference in the absorbance spectra of solid state [5]Ph across the several tests is due to the timing of the tests itself: different stages of optimisation of the film led to slightly different spectrum shapes, but the trend with respect to thermal degradation stays the same.

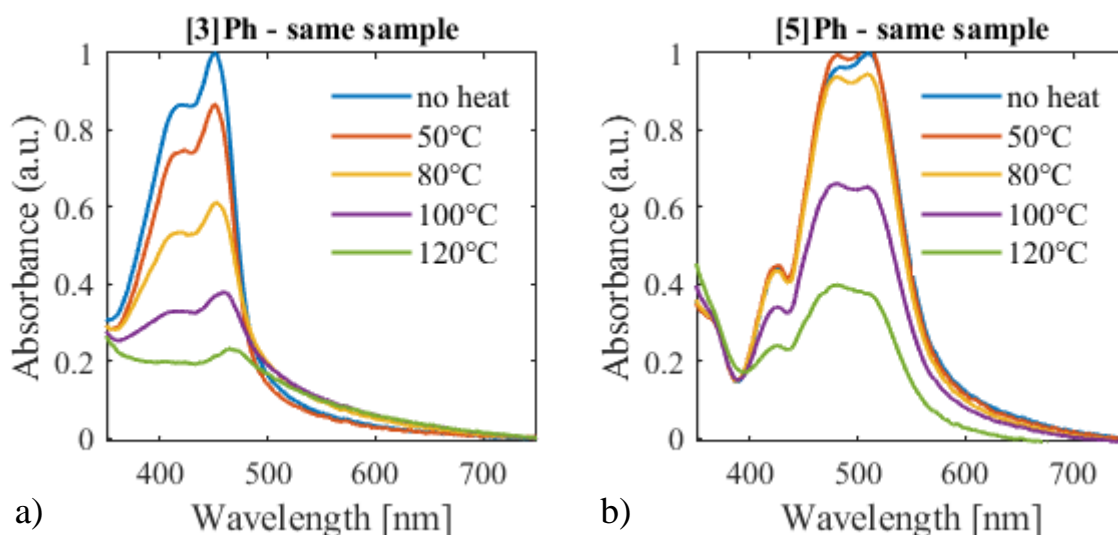


Figure 5.16 Effect of accumulated 30-minute long intervals at 50 °C, 80 °C, 100 °C, 120 °C on thin films of a) [3]Ph and b) [5]Ph.

To rule out any influence from the solvent, such as residues that could allow reorganisation of the molecules at high temperature, the test was repeated, after leaving the samples in high vacuum ($1 \cdot 10^{-6}$ mbar) overnight. [3]Ph was retested at 100 °C (for 30 minutes), while [5]Ph was retested at 80 °C for the same amount of time. As the spectra in Figure 5.17(a) and 5.17(b) show, there is no significant difference between the samples left in high vacuum and those that were left in air.

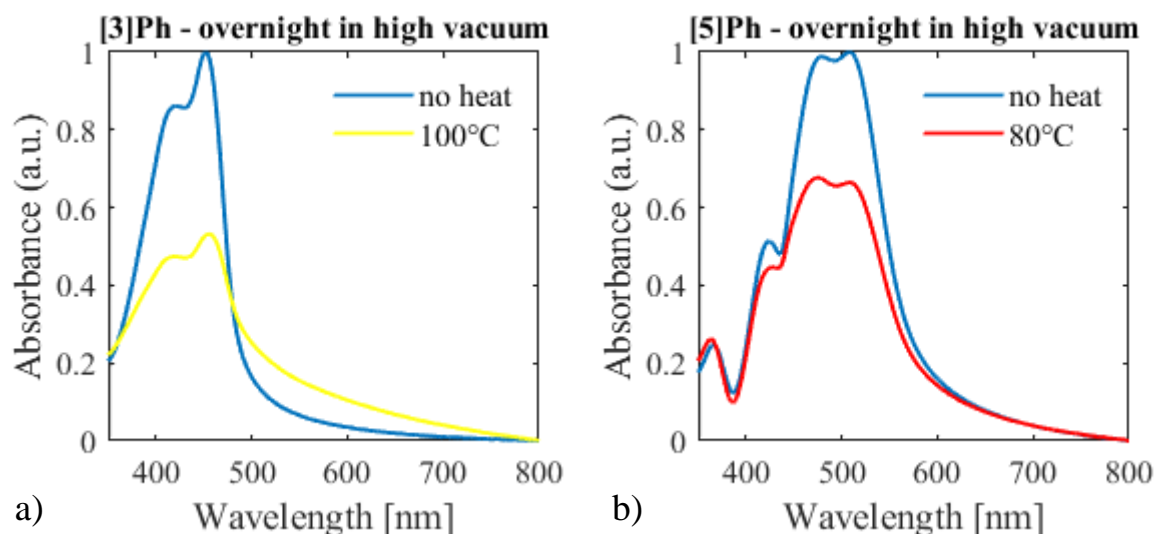


Figure 5.17 Effect of at 30-minute long interval on a) [3]Ph thin film at 100 °C, and b) [5]Ph thin film at 80 °C, when both samples are left in high vacuum.

In addition, by comparing those new spectra with the ones previously showed, we can assume that either 1,2-DCB residues were not present in the earlier tests or that the materials did not suffer any influence coming from the solvent.

In conclusion, many tests were carried out to find the suitable conditions to deposit [3]Ph and especially [5]Ph, without incurring into degradation.

Discovering the reactions that the molecules undergo during degradation was beyond the scope of this task. However, from the UV-Vis spectra, we can speculate that degradation does not lead to the formation of new species, at least not ones absorbing visible light, as no new peaks were present.

That being said, it was confirmed that both [3]Ph and [5]Ph are photosensitive materials, and it only takes a short amount of time of irradiation to cause damage to the films. Solutions seem to be more resistant to visible light for short exposures.

As for heat, [5]Ph solutions proved to be incredibly sensitive to even moderate temperatures, like 50 °C. Hence, the decision to reduce as much as possible the exposure of these solutions to any form of heat. A quick stirring at 35 °C takes place before deposition, for maximum 30 minutes, when the concentration is 10 g/l. For lower concentration, just stirring suffices. [5]Ph and [3]Ph thin films do not benefit from annealing, but they are not as delicate as the solutions, while [3]Ph solutions are incredibly stable even at temperatures well above 100 °C.

6. EXPERIMENTAL RESULTS – ELECTRICAL MEASUREMENTS

The assessment of the charge transport properties of [3]Ph and especially [5]Ph is the ultimate goal of this thesis work.

6.1 [3]Ph

At the beginning of this thesis work, there was on-going research about this molecule, which has been already investigated and optimised[13]. So the aim was to improve its charge carrier mobility and stability even further, if possible, but more importantly [3]Ph was used as a reference for [5]Ph optimisation.

6.1.1 [3]Ph as a reference

The set-up conditions that were proved to allow for the best transistor performance are as follows:

- OFET configuration: top-gate bottom-contact;
- Substrate: low alkali 1737F Corning glass;
- Contacts: interdigitated pattern with channel length varying from 2.5 to 40 μm , defined by standard photolithography. 30 nm Au with 3 nm Cr adhesion layer, deposited by thermal evaporation;
- Semiconductor solution: 10 g/l in 1,2-DCB, stirred at 50 °C for at least 1 hour, then heated up to deposition temperature;
- Semiconductor deposition: nitrogen-assisted bar-coating at 80 °C, with a bar speed of 30 mm/s;
- No annealing required: samples were kept on the bar coater plate just as long as to let the solvent evaporate, so under a minute;
- Dielectric: Parylene C layer, thickness of about 400 nm;
- Gate: ink-jet printed PEDOT:PSS.

Sticking to this procedure, well performing field effect transistors can be fabricated, with field effect hole mobility up to 10^{-1} cm^2/Vs , as Figure 6.1(a) and 6.1(b) demonstrate. Both the transfer and the mobility curves display ideal behaviour, with little to no hysteresis in the reverse sweep; steep subthreshold slope; no dual switching; identical linear ($V_{D,\text{lin}} = -5$ V) and saturation ($V_{D,\text{sat}} = -40$ V) mobilities, which are independent from gate bias (V_g), passed the threshold voltage ($V_{\text{th}} = -6$ V). The device starts switching on at voltages below -2 V, and the $I_{\text{on}}/I_{\text{off}}$ ratio stands at about 10^5 [13].

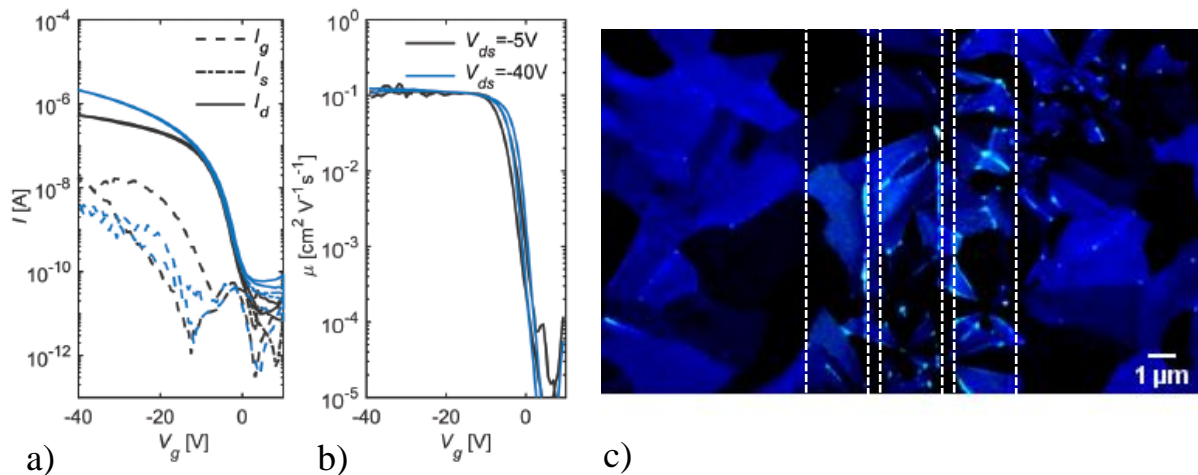


Figure 6.1a) Characteristic transfer curves in both linear and saturation regimes (black and blue lines, respectively) in a TGBC OFET based on [3]Ph [13]. **b)** Charge mobility against gate voltage in both linear and saturation regimes [13]. **c)** POM image of [3]Ph film wire-bar coated on gold contacts, underlined by the dotted line.

Figure 6.1(c) is the POM image of a [3]Ph transistor: in thin films deposited at 80 °C, [3]Ph arranges in flat crystalline grains, that efficiently transport charge across the channels.

6.1.2 Optimisation of transistors based on [3]Ph

The main issue when working with [3]Ph, as underlined in the previous chapter, is certainly its photosensitivity; so, shielding the transistors from light in each step subsequent to semiconductor deposition was the first attempt to improve the performance of those devices.

One option was to employ activated carbon (AC), which is conductive and black, that could act both as a gate and as an opaque barrier. An ink made of fine particles of activated carbon, in ratio 2:1 with its binder and with ethanol as solvent, was spray-coated onto the Parylene layer through an airbrush. A mask ensured the selective deposition of the ink on the channels only (Figure 6.2).

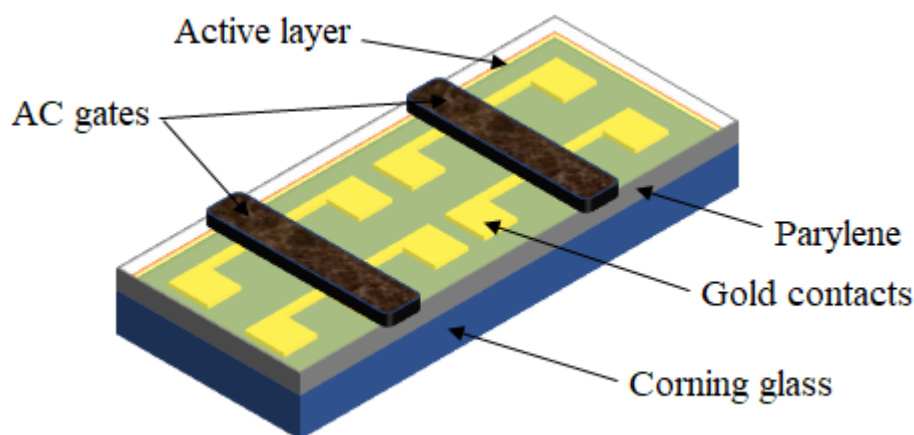


Figure 6.2 Structure of an AC gated [3]Ph transistor, in TGBC configuration.

A few issues were encountered. The airbrushed layer showed very poor adhesion to Parylene, though more importantly, the resulting layer was not homogeneous. The surface finish was rough, the thickness relatively high (a few hundreds of μm) and percolation was not always reached. This led to a relatively low conductivity of the gate, although the light-shielding action was effective, as no light could shine through the AC layer.

None of the transistors fabricated with this kind of gate worked. Some devices just did not modulate the current, others were short-circuited, meaning that the current was free to circulate from the gate to the contacts: no field effect could be established. Apparently, the gate deposition by spray-coating of the AC ink is affecting the insulating properties of the Parylene layer. We might speculate that the soft Parylene layer got damaged by the incoming particles

To enhance the contact conductivity, which was suspected to be at least part of the issue, an increase in the concentration of activated carbon was considered, but that would have caused an even worse adhesion of the spray-coated layer to the substrate, so a different route was chosen.

An ink based on coarser particles of activated carbon, in the same ratio 2:1 with respect to the binder, was airbrushed in the same way. The surface ended up being rougher, but the conductivity was slightly higher, and the layer opacity was still perfect, no light could be transmitted through the layer.

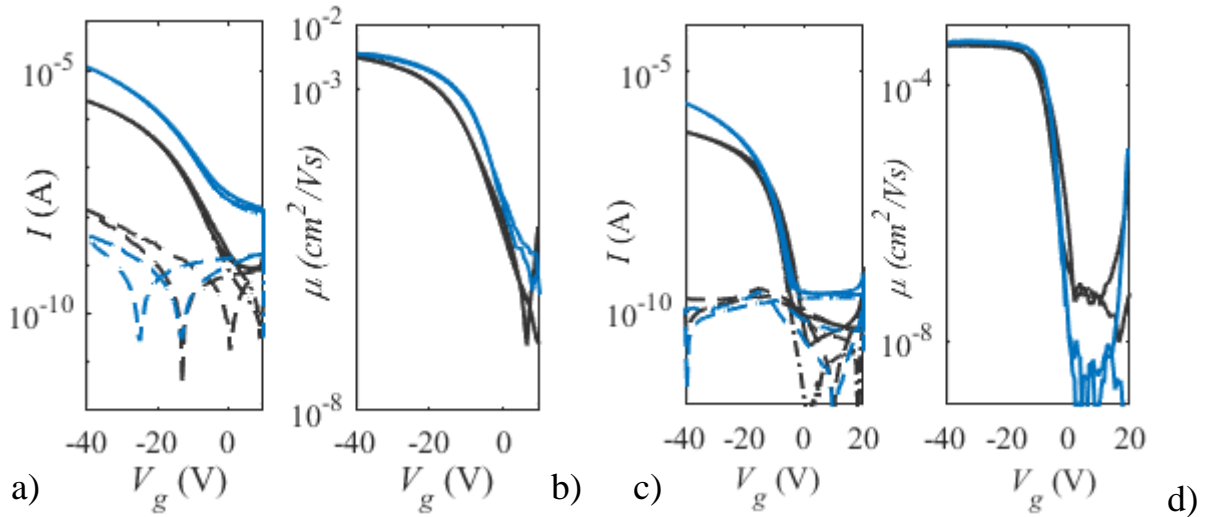


Figure 6.3 **a)** Characteristic transfer curves of a transistor based on [3]Ph and gated through a spray coated activated carbon ink; the black line refers to linear regime (-5 V), the blue one to saturation regime (-40 V); the solid line is the drain current, the dotted one the gate current. **b)** Corresponding charge mobility curves. **c)** Characteristic transfer curve of a transistor from the same batch based on [3]Ph and gated through ink-jet printed PEDOT:PSS. **d)** Corresponding charge mobility curve.

Out of the eight devices gated by the activated carbon ink, six were impossible to measure because short-circuited, while the other two were functional. As displayed by Figure 6.3(a), the shape of the transfer curve of an AC-gated transistor is less ideal with respect to transistors gated by PEDOT:PSS (Figure 6.3(c)), featuring a far less steep subthreshold slope when switching on. V_{on} is comparable with the above mentioned value (about -1,5 V), but V_{th} shifts towards more negative potentials (about -11 V) and I_{on}/I_{off} ratio drops to 10^3 . The measured mobility is around $10^{-3} \text{ cm}^2/\text{Vs}$ (Figure 6.3(b)), which may seem low for this material, but it turned out to be higher than the mobility measured on devices from the same batch but gated through printed PEDOT:PSS (Figure 6.3(d)).

As for light-shielding, one of the two working transistors went through cycles of measurements under light of varying intensity. Figure 6.4(a) underlines the surprising stability of the transistor, whose transfer curve never changed significantly throughout the analysis. In particular, no significant hysteresis appeared. The last measurement, run with no light shining over the sample, assessed a drop in the I_d current, likely due to accumulation of thermal effects, since all the measurements were performed in quick succession, one after the other, and intense voltages were applied on a relatively short-channel transistor (10 μm), so thermal degradation might have been the cause.

As a reference, Figure 6.4(b) shows what would normally happen to a [3]Ph based transistor, measured under the same condition of lighting. It is very easy to detect a progressive decrease

ELECTRICAL MEASUREMENTS

in the current as well as the ever growing hysteresis as the material degrades and traps are formed. V_{th} significantly shifts to lower voltages, reaching the value of -20 V. Mobility does not drop too much (Figure 6.4(c)), but the extracted value becomes more and more unreliable, the farther the transfer curve moves away from ideality. Besides, from the comparison of the normalised values of both mobilities, it is clear that the PEDOT:PSS device suffered much more damage from light than the AC one (Figure 6.4(d)).

The very last measurement on the PEDOT:PSS transistor was run 1 week after fabrication and previous measurements: during this interval, the device was kept protected from light, in nitrogen atmosphere. The material managed to partially recover from photodamage, although currents and charge mobility were still lower with respect to the first measurement, meaning that both reversible and irreversible degradation processes are taking place.

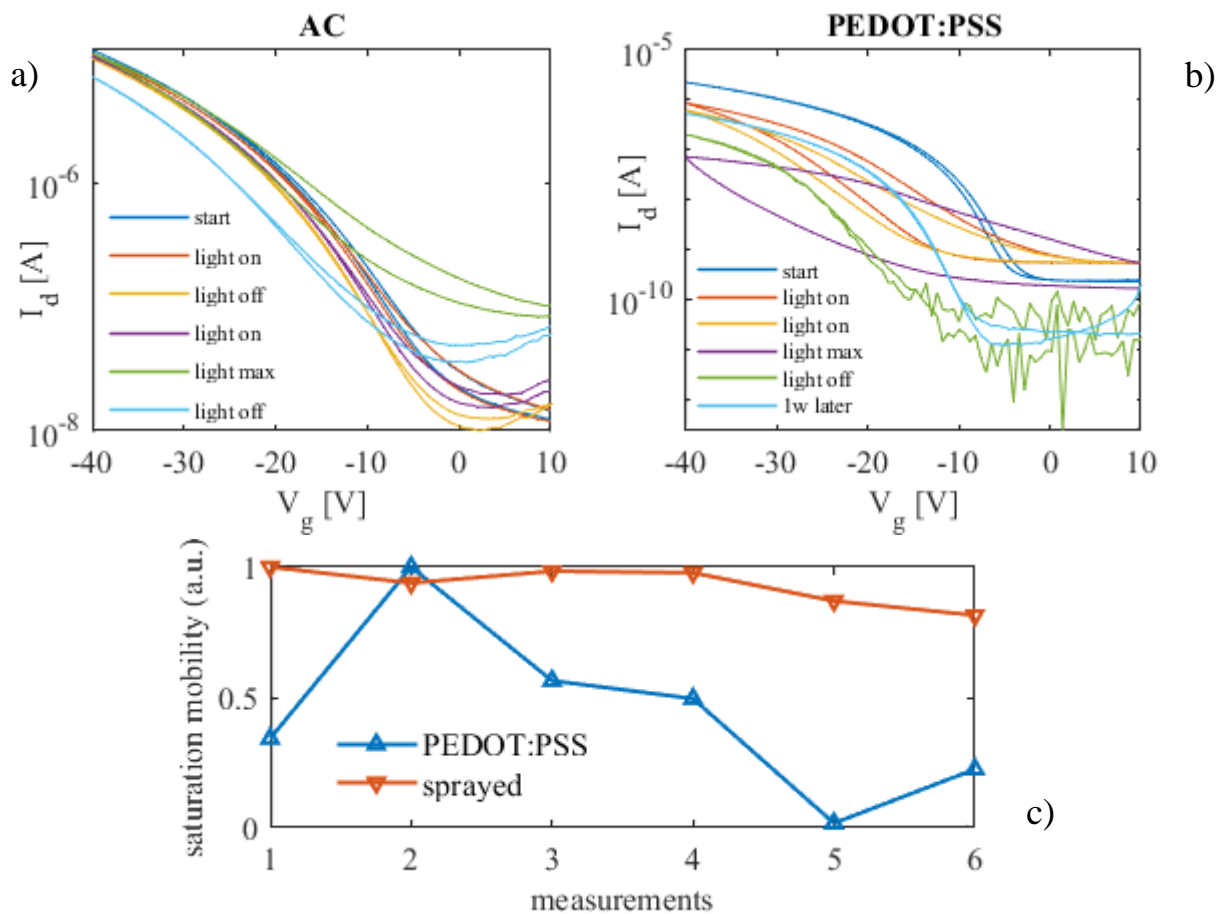


Figure 6.4 a) Transfer curves from a [3]Ph based transistor gated through spray coated AC ink, measured under different light conditions. b) Transfer curves from a [3]Ph based transistor gated through ink-jet printed PEDOT:PSS, measured under different light conditions. c) Comparison between the mobility curves referred to the previous devices, each normalised to their maximum value.

So, we can conclude that this type of gate is a good solution to prevent light from shining on the transistors. On the other hand, this method needs optimisation, as it does not work all the time. The spray coating process is likely to disrupt the soft Parylene layer, either short-circuiting the device altogether or altering the very important interface between the dielectric and the semiconductor. As explained in a previous chapter, that interface needs to be as regular as possible not to hinder the charge transport. Furthermore, the activated carbon layer should be made more homogeneous and adherent to Parylene to make contacting probes easier.

A second option to reduce photodamage of the transistors was attempted: this time, it was about reducing light exposition, rather than shielding the samples from light with an opaque gate; PEDOT:PSS was employed as the third contact, but, instead of depositing it through ink-jet printing, procedure requiring a microscope and so a focused light, it was wire-bar coated at room temperature by a 20 μm bar, with no N_2 flow assistance (Figure 6.5).

No remarkable improvements were observed with respect to the standard procedure based on ink-jet printing, but it turned out to be a reliable, straight-forward and quick method to gate large-area transistors (width of the interdigitated contacts of more than 1 mm).

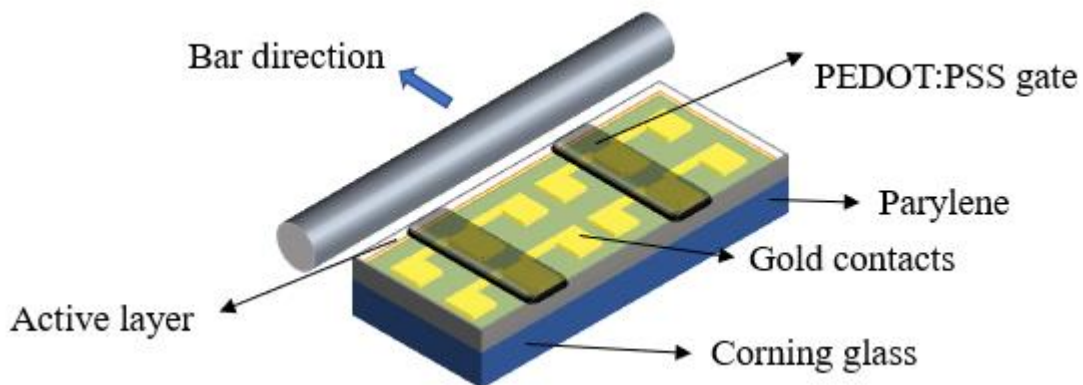


Figure 6.5 TGBC [3]Ph based transistor, gated by bar coated PEDOT:PSS.

It should be underlined that both these techniques, spray coating and bar coating, are mostly suitable for certain contact geometries: they are both easy to perform on CMS patterns, but they are hardly applicable to patterns featuring smaller sizing, such as Fraunhofer-like patterns (Paragraph 3.2.1). For those finer geometries, the high resolution of an ink-jet printer grants more ease of deposition. Shadow masks could be used for making spray coating more precise, and post-deposition selective laser ablation might work as a subtractive process to enhance bar coating resolution, but ultimately those are techniques, which better fit larger geometries.

6.2 [5]Ph

As already mentioned, [5]Ph is a relatively unknown material: it has been studied from a chemical point of view, but very little effort has been dedicated to its solid state properties and to possible applications as of yet.

This molecule is a p-type semiconductor and features a smaller energy gap in comparison with [3]Ph, due to a longer conjugation length and a smaller BLA, suggesting that it might be better performing in terms of charge transport, provided that it can pack efficiently.

In this thesis work, an effort was made to fabricate OFETs based on [5]Ph as the active material.

6.2.1 Transistors in BGBC configuration

At the beginning of this thesis work, to my knowledge there only had been one attempt at fabricating transistors based on [5]Ph, and it was done by dropcasting a 4 g/l solution of [5]Ph in Dichloromethane on Fraunhofer substrates in nitrogen atmosphere. Then the samples were transferred to air, before being put back into a glovebox for the electrical measurements. Both the transfer and the output curves of those devices were very far from ideality: massive hysteresis was present, the subthreshold slope was shallow, the on-off current ratio was also low, and charge injection was inefficient. A mobility as high as 10^{-5} cm²/Vs was obtained, but, given the lack of ideality, it is not a reliable value whatsoever [56].

As a first screening test, a similar procedure was followed, except the solvent was 1,2-Dichlorobenzene: the solution was dropcasted onto a Fraunhofer substrate in a glovebox, i.e. in nitrogen atmosphere, a 30 minute long annealing step at 50 °C was carried out to accelerate evaporation, then the samples were taken out of glovebox and kept protected from light for a couple of days. Finally, the transistors were measured through SPA in controlled nitrogen atmosphere, with both O₂ and H₂O content below 0.1 ppm. Figure 6.6(a) and 6.6(b) show the transfer curve and the extracted mobility.

It is worth pointing out that surface coverage was highly inhomogeneous, as underlined by Figure 6.6(c) and 6.6(d): long needle-like structures are commonly present all over the surface, but they appear randomly oriented in some spots, while they are perpendicular to the evaporation fronts elsewhere. Due to this kind of morphology, which is unfavourable to charge transport, most devices did not work, and it was possible to only measure a few transistors out of the sixteen patterns of the Fraunhofer substrate.

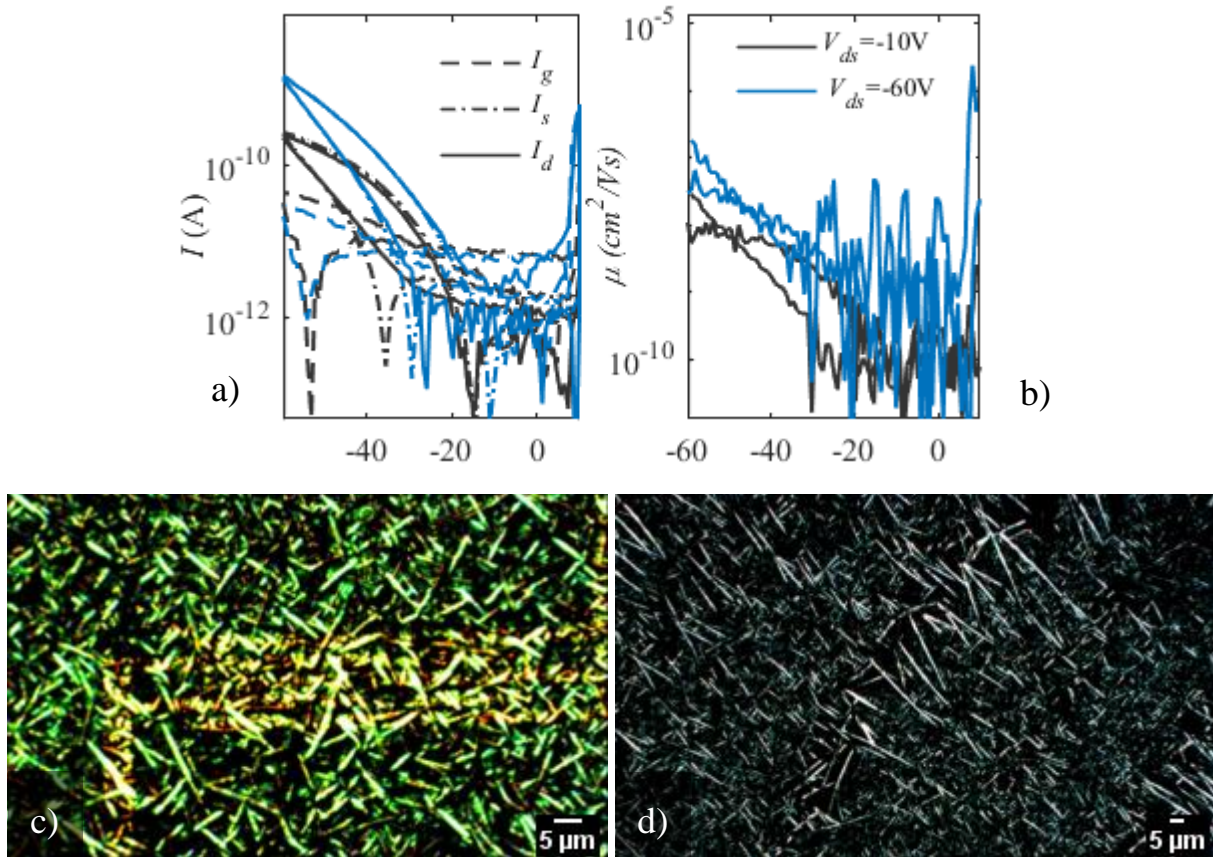


Figure 6.6 **a)** Transfer curves of a transistor based on dropcasted [5]Ph on Fraunhofer substrate, with black line representing linear regime and the blue one for saturation regime. **b)** Mobility referred to the same transistor, in linear (black line) and saturation regimes (blue line). **c)** POM picture of the transistor, with 90° polarisation. **d)** POM picture of the dropcasted [5]Ph structures, with 90° polarisation.

In both regimes, the charge mobility is low, reaching a value of about 10^{-8} cm^2/Vs in saturation regime, and leakage currents are high. Overall, field-effect behaviour is observed, with an on-off current ratio of about 10^5 . However, the transfer curves are far from displaying ideal behaviour, making unreliable the extraction of derived parameters such as mobility, threshold voltage and turn-on voltage, respectively averaging around -11 V and -18.5 V, though more importantly, the transistors display a significant hysteresis in the reverse sweep.

Such clockwise hysteresis is commonly due to the formation of charge traps at the interface with the dielectric at high voltage: those traps decrease the number of available charges, and the resulting current turns out to be much lower than the one of the forward sweep [53]. It's worth pointing out that hysteresis is often limited to the linear regime, after which traps might get filled, so that hysteresis is strongly reduced in saturation regime. Another possible explanation is related to a more intense lateral field: this allows to reduce the trap barrier, which

turn from deep to shallow. However, saturation regime still displays hysteresis in dropcasted [5]Ph transistors, suggesting that traps keep forming and the device does not stabilise.

As an additional test, two solutions of “C6-5” were also dropcasted onto Fraunhofer substrates in the same fashion, but it was impossible to measure them, probably due to lack of crystallinity, as Figures 6.7(a) and 6.7(b) show, and so to very low conductivity. The material did not seem to form any crystalline structures on SiO₂, according to POM inspection: only isolated, irregular agglomerates could be spotted in an otherwise amorphous matrix.

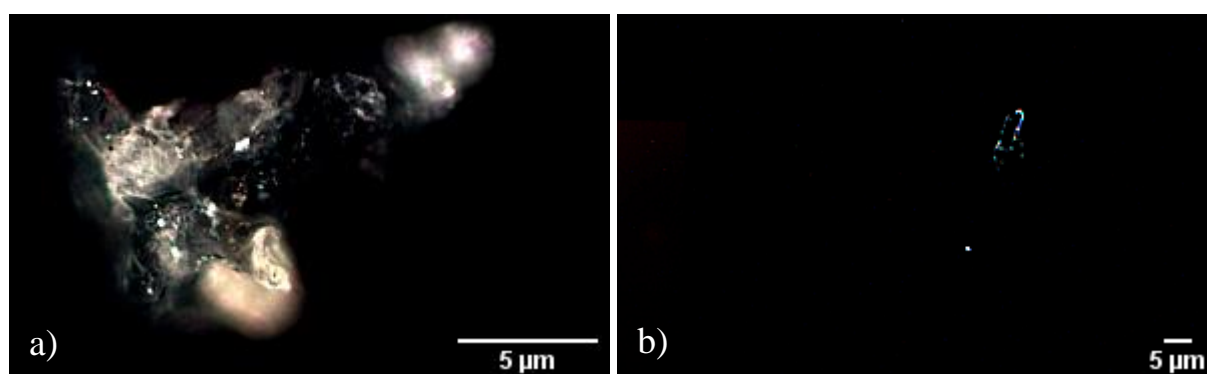


Figure 6.7 a) POM image of a solution of “C6-5” dropcasted onto Fraunhofer substrate, with a polarisation of 90°, showing isolated agglomerates in amorphous matrix. b) POM image of a solution of “C6-5” dropcasted onto Fraunhofer substrate, with a polarisation of 90°, also showing agglomerates in amorphous matrix.

As stated before, the experiment with the dropcasted [5]Ph was just a screening test. This deposition method typically leads to the formation of bulk-like structures, but the goal of this work was to fabricate transistors based on thin films to enhance the charge transport and improve the transistor characteristics.

Indeed, the reasons behind the poor performance of the transistor based on dropcasted [5]Ph are most likely linked to low film quality and possibly to the bulk structures.

So, wire-bar coating was selected as preferential deposition technique and the annealing step was removed, as it was deemed not necessary: deposition is carried out at high enough temperatures and the solvent evaporates within seconds. Besides, [3]Ph had been proved to create good films without post-deposition thermal treatments, and so the same route was chosen for [5]Ph. Later stability tests revealed that thermal treatments actually cause damage to the film, so the annealing step was definitively ruled out.

In Section 4.1, film optimisation was thoroughly described. Several transistor batches were fabricated along this process: the plan was to test the optimised film whenever an improvement of the film coverage and morphology was detected by polarised optical microscopy.

The first batch of transistors in BGBC configuration relied on a 30 nm thick layer of gold as gate electrode, which was evaporated on corning glass with a 3 nm adhesion layer of chromium. Parylene C was then deposited (520 nm of thickness). Photolithography followed, after which a second thermal evaporation was carried out to deposit source and drain. Finally, the semiconductor was wire-bar coated as the last step: a 20 g/l solution of [5]Ph in 1,2-DCB was stirred at 40 °C for 30 minutes; then, bed temperature and bar speed were set respectively at 80 °C and 30 mm/s, according to [3]Ph optimised conditions; the deposition was performed without N₂ flow assisting evaporation, in yellow room.

All the fabrication steps were carried out in air, while the subsequent measurements were performed in a glovebox, in nitrogen atmosphere, by Semiconductor Parameter Analyser.

It was impossible to measure the transistors: most of them did not modulate the current properly, a few were short-circuited. This might have been due to damages to the dielectric layer, which is soft Parylene, likely during the photolithographic step or semiconductor deposition, or to charge injection issues (Section 2.2). Another possible explanation has to do with the fact that in BGBC the active layer is the last layer to be deposited, so it's exposed to the atmosphere.

As a solution to that, Parylene encapsulation was attempted: Parylene C has a low permeability to oxygen and an even lower one to nitrogen, so it could act as a barrier during storing and electrical measuring.

Starting from a BGBC-structured substrate, a solution of [5]Ph (10 g/l in 1,2-DCB), stirred at 40 °C for half an hour, was wire-bar coated following the previously explained procedure: bed temperature at 80 °C, no N₂ flow, bar speed lowered to 20 mm/s, in yellow room, in air.

Two samples, for a total of 32 devices, were processed. One was stored as it was, to be used the next day as reference. The other one was put in the Parylene evaporator and a second Parylene layer of 1000 nm of thickness was deposited.

The transistors were measured the next day in nitrogen atmosphere, with no improvement with respect to previous tests. Neither the devices on the reference sample nor the encapsulated ones were functional. Hence, degradation of the semiconductor due to exposure to oxygen and moisture must not be the principal cause for the devices failure. On the contrary, dielectric layer damage or charge injection issue are still valid explanations.

6.2.2 Transistors in TGBC configuration

The first batch in TGBC configuration was fabricated with the same exact deposition conditions applied to the BGBC devices, except for the glass substrate: a 20 g/l solution of [5]Ph in 1,2-DCB, previously stirred at 40 °C for 30 minutes, wire-bar coated at 80 °C, by a 10 µm bar

ELECTRICAL MEASUREMENTS

moving at a speed of 30 mm/s, with no N₂ flow involved. The semiconductor was deposited on Au contacts (Fraunhofer pattern), previously prepared by lithography and thermal evaporation, in dark conditions, after surface activation run in a plasma asher. Next, Parylene C was deposited in a thickness of 600 nm. The last step was the ink-jet printing of the PEDOT:PSS gate.

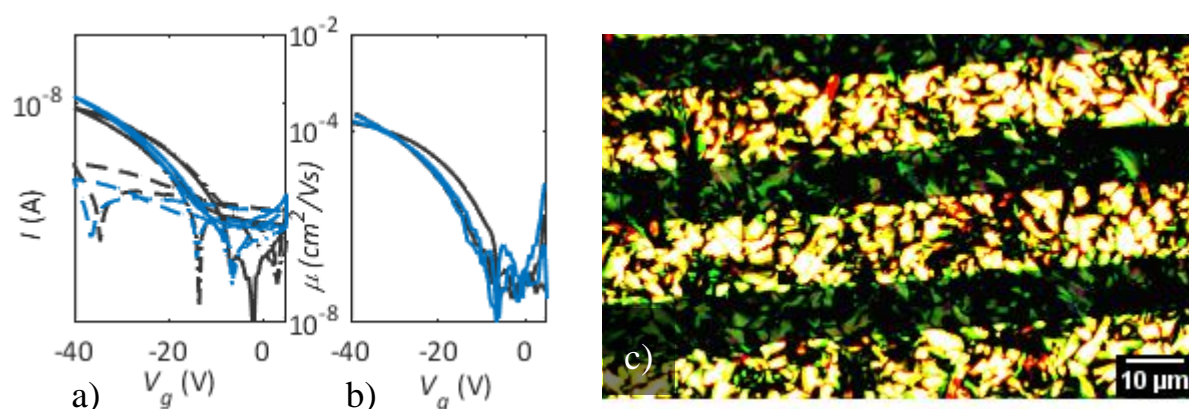
All those steps were carried out in air, while the subsequent measurements were performed in a glovebox, in nitrogen atmosphere, according to Semiconductor Parameter Analyser.

The results were quite promising, as all transistors worked and showed good repeatability.

Figure 6.8(a) shows the characteristic transfer curves referred to a 10 μm channel device, both in linear regime at V_{ds} = -5 V, in black, and in saturation regime at V_{ds} = -40 V, in blue. At this early stage, [5]Ph clearly does not show the ideal behaviour displayed by [3]Ph based devices.

There is hysteresis on the reverse sweep, particularly during linear regime: it's probably due to charge traps, formed at high voltage; when they're filled, the transfer curve stabilises, but V_{on} shifts towards slightly more negative values. In general, saturation V_{on} spans between -5 V and -9 V across this batch of devices, while V_{th} is stable around -19 V. This marks an important difference with respect to the devices based on dropcasted [5]Ph, as those kept showing hysteresis in saturation regime as well, with no remarkable shifts in V_{on} or V_{th}.

Detected currents and extracted mobilities are significantly lower than [3]Ph devices, spanning from 9 × 10⁻⁶ cm²/Vs to 8 × 10⁻⁵ cm²/Vs in saturation regime and not even reaching a plateau in the trend (figure 6.8(b)). One more important point to note is the I_{on}/I_{off} ratio, which is in the order of magnitude of 10⁴, enough to prove field-effect activity.



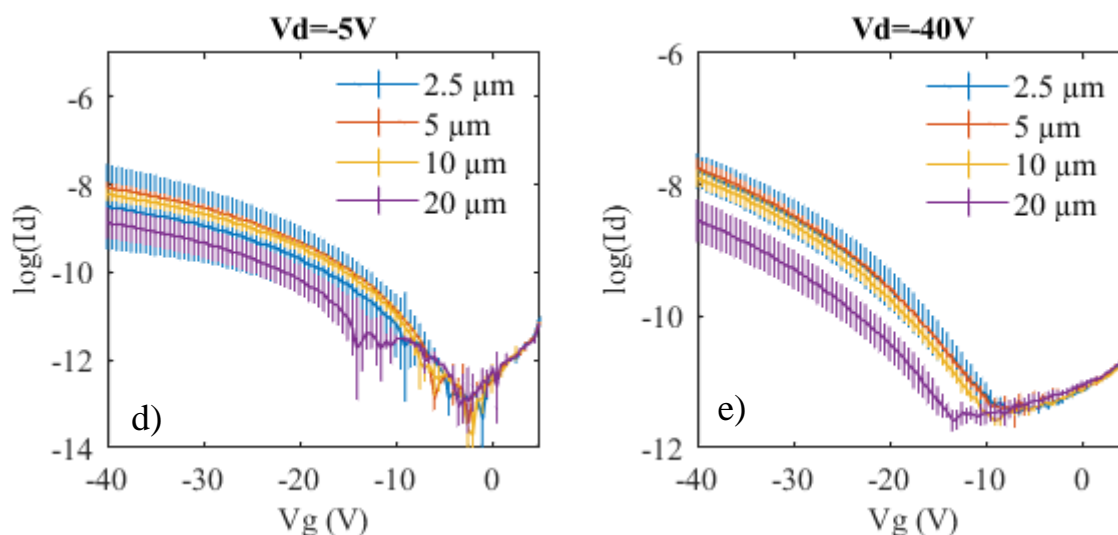


Figure 6.8 a) Transfer curves of a transistor based on bar coated [5]Ph (10 g/l in 1,2-DCB), with black line representing linear (-5 V) regime and the blue one for saturation regime (-40 V); solid line refers to drain current, while the dotted one is for gate current. **b)** Mobility referred to the same transistor, in linear (black line) and saturation regimes (blue line). **c)** POM image of the same transistor, with 90° polarisation. **d)** Standard deviation of the currents, in log scale, across all the measured transistors of a same batch, in linear regime. **e)** Standard deviation of the currents, in log scale, across the measured devices, in saturation regime.

Figure 6.8(c) is a picture of the film on top of the considered device: coverage is good, and the film appears homogeneous, although crystalline grains are small, reaching a maximum length of about 10 μm . This explains what can be observed in pictures Figure 6.8(d) and 6.8(e), which are the standard deviation of the currents in linear and saturation regime, respectively, sorted according to channel length: 20 μm channel devices performed worse than the others because structures are not large enough to cross the channels and provide an effective bridge for charge to be transported by. Indeed, the mobilities measured on those wider channel transistors are lower than on the other devices. 2.5 μm channel devices are typically characterised by a higher influence of the contact resistance, but in this case those transistors performed well.

After this previous attempt, more TGBC devices were fabricated during the optimisation process.

The best results were obtained by wire-bar coating a 10 g/l solution of [5]Ph in 1,2-DCB, at 70 °C, with a bar speed of 45 mm/s and with no N_2 flow. The contacts geometry was switched from Fraunhofer to CMS to minimise the contribution of contact resistance, since CMS devices feature larger gold patterns.

The stirring process of the solution was also kept short, below 30 minutes, and at 35 °C. Parylene thickness was 370 nm, and the devices were gated by bar coated PEDOT:PSS.

All fabrication steps were carried out in air and the measurements took place in nitrogen atmosphere.

Figure 6.9(a) shows the characteristic transfer curves of one of the transistors from that batch: the trend comes much closer to ideality, with respect to previously fabricated devices. There is no sign of hysteresis, leakage current is low and I_{on}/I_{off} ratio is 2×10^6 . On top of that, the subthreshold slope, at 1130mV/dec in saturation, is steeper with respect to previous [5]Ph devices. V_{on} and V_{th} values are also less negative than usual, respectively at -5 V and -13 V. As for field effect mobility, Figure 6.9(b) depicts a plateau at $2.3 \cdot 10^{-3} \text{ cm}^2/\text{Vs}$.

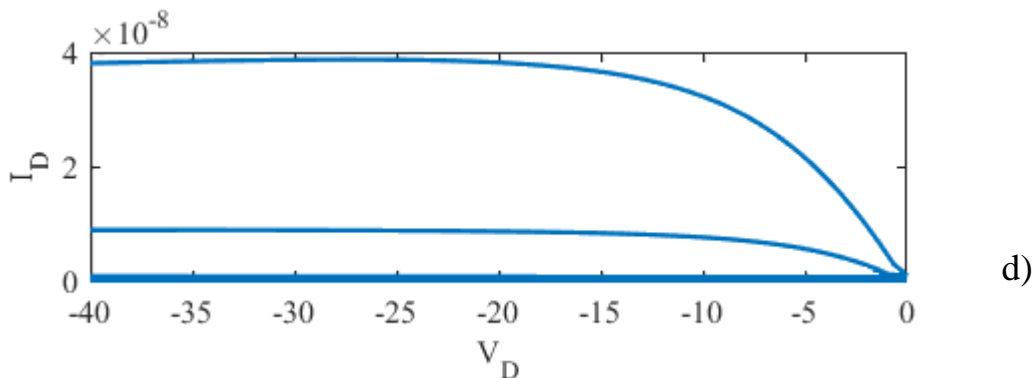
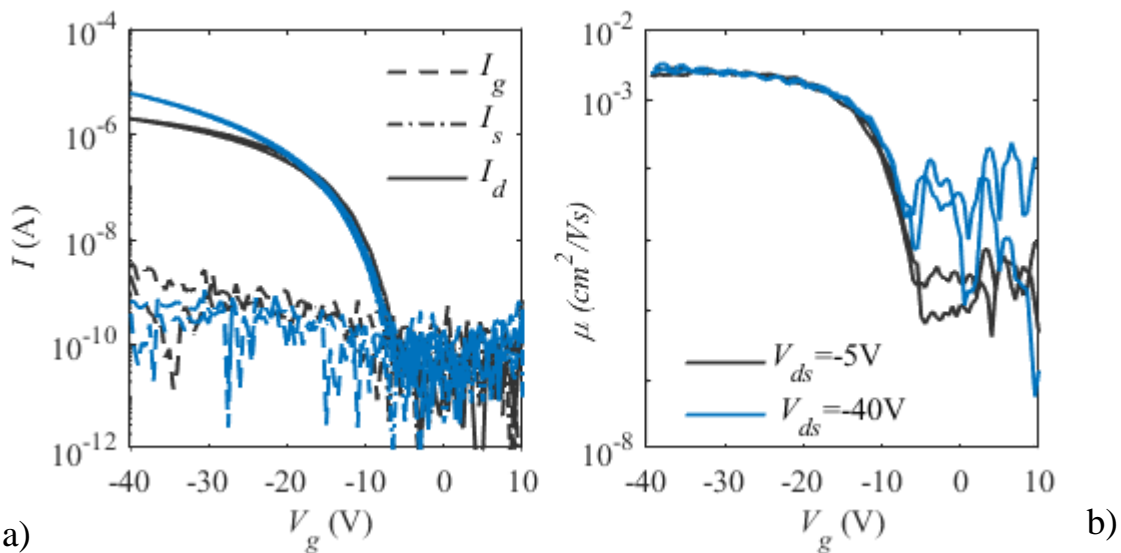


Figure 6.9 a) Characteristic transfer curves of a transistor based on optimised [5]Ph, showing in black the linear regime and in blue the saturation one. **b)** Corresponding mobilities of the same device. **c)** POM image of the same transistor, with 90° polarisation. **d)** Output curves referred to one of the other devices from the same batch.

Figure 6.9(c) shows the POM image of that same transistor: it is interesting to observe that what ended up being the best working device does not display a homogeneous thin film. Indeed, fibre bundles long enough to cross the 20 μm channel appear to be the dominant structures.

Despite a good approximation to ideality shown by the device, V_{on} and V_{th} are still fairly negative in all the transistors from that batch. This might be explained by injection issues, pointed out by the s-shape in the region close to 0 V of the output curve (Figure 6.9(d)).

Overall, at this stage [5]Ph devices are still less performing than [3]Ph ones, but an increase of five orders of magnitude in charge mobility has been accomplished since the beginning of the tests.

6.2.3 Transistors based on [5]Ph:PS

In order to improve the film, attempts were made at blending [5]Ph with dielectric polymers, just like it had been done with [3]Ph. Blending semiconducting small molecules with insulating polymers is a known strategy in organic electronics, because the polymer is supposed to help the small molecule crystallisation, through a vertical phase separation, without interfering in the charge transport measurements [70]

Following this rationale, a blend of [5]Ph:PS, in equal concentration of 10 g/l in 1,2-DCB, was wire-bar coated on a lithography (Fraunhofer pattern). Almost same deposition conditions as before were kept: as dark as possible environment, bed temperature of 80°C, no N_2 flow, bar speed lowered to 20 mm/s. The next steps were Parylene C deposition and gate ink-jet printing. The measurement was then run the usual way.

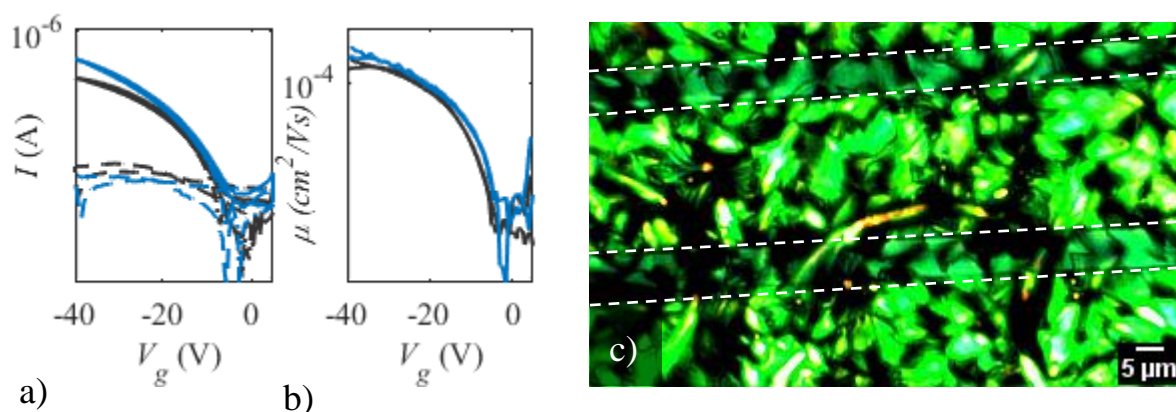


Figure 6.10 a) Transfer curves of a transistor based on bar coated [5]Ph:PS blend (1:1, 10 g/l in 1,2-DCB), with black line representing linear regime ($V_D = -5$ V) and the blue one for saturation regime ($V_D = -40$ V); the solid line refers to drain current, the dotted one to gate current. **b)** Mobility referred to the same transistor, in linear (black line) and saturation regimes (blue line). **c)** POM image of the same transistor, with 90° polarisation: the channels are emphasised by the white dotted line.

Figure 6.10(a) and 6.10(b) depict the transfer curves and the mobilities of the second run of measurements on a $5 \mu\text{m}$ channel device, after the first one produced hysteresis in the backwards sweep in linear regime, similarly to what had happened in the very first batch of TGBC transistors (Figure 6.8(a)): it was most likely due to charge traps forming at high voltages, as already observed in previous tests, and once those traps were filled, the trend became closer to an ideal shape. A very slight shift towards more negative voltages in V_{on} and V_{th} was observed.

It should be noted that out of sixteen transistors, only four were working. This is probably due to a certain inhomogeneity of the film, which appears to have crystallised differently on different areas of the same sample, and possibly to a misplacement of the insulating polymer with respect to [5]Ph and contacts. It is very hard to control the precise vertical phase separation of the blend components, which makes the outcome unpredictable. Figure 6.10(c) is a POM image of the film in correspondence of the device, whose measurement appears in the adjacent pictures, but other spots displayed a different kind of morphology (see Section 4.1 for pictures of different structures formed by the [5]Ph:PS blends), which might explain the difference in the devices across the same sample.

Overall, the working devices were better performing than early ones based on [5]Ph alone. Leakage current is not too high, $I_{\text{on}}/I_{\text{off}}$ ratio is still averaged around 10^4 and saturation charge mobility stands at about $2 \times 10^{-4} \text{ cm}^2/\text{Vs}$ in the considered voltage range, without becoming properly independent on V_g .

Overall [5]Ph:PS devices are inferior in terms of performance with respect to those based on optimised [5]Ph alone.

6.2.4 Transistors based on [5]Ph:PMMA

The next step was trying out a different insulating polymer, i.e. PMMA, in conjunction with [5]Ph. The protocol followed for the fabrication of these devices was identical to previous attempts. The active layer, i.e. a 10 g/l solution of [5]Ph:PMMA (1:1) in 1,2-DCB stirred for an hour at 40°C , was wire-bar coated onto a lithography at 80°C of temperature, 20 mm/s of speed, without N_2 , in a reasonably dark environment, in air. Parylene deposition and gate printing followed, before moving on to the electrical analysis step carried out in glovebox.

A very small number of transistors, mostly short-channel ones, ended up working. The working ones were not well performing, as it can be inferred by the transfer curves in Figure 6.11(a): there is significant hysteresis in the reverse sweep, both in linear and in saturation regimes, detected currents are lower with respect to [5]Ph:PS devices and there is significant leakage, as I_g is fairly high. The extracted saturation mobilities ranged between $3 \cdot 10^{-5} \text{ cm}^2/\text{Vs}$ to $9 \cdot 10^{-5} \text{ cm}^2/\text{Vs}$ (Figure 6.11(b)), saturation V_{on} and V_{th} varied a lot, the former spanning from -4V to -8V, the latter from -15 V to -18 V. $I_{\text{on}}/I_{\text{off}}$ ratio was about $5 \cdot 10^3$.

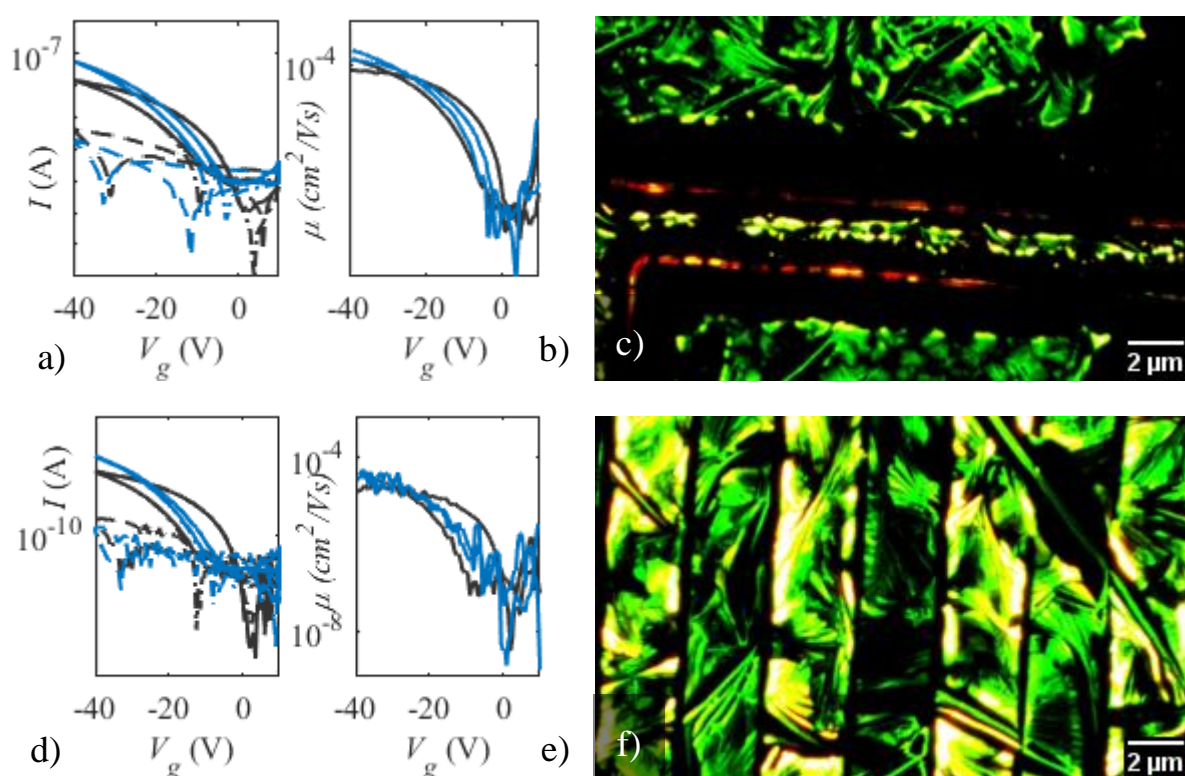


Figure 6.11 **a)** Transfer curves of a transistor based on a [5]Ph:PMMA blend (1:1, 10 g/l in 1,2-DCB), bar coated at 80 °C, with black line representing linear regime ($V_D = -5 \text{ V}$) and the blue one for saturation regime ($V_D = -40 \text{ V}$); the solid line is for drain current, the dotted one for gate current. **b)** Mobility referred to the same transistor, in linear (black line) and saturation regimes (blue line). **c)** POM image of the same transistor, with 90° polarisation. **d)** Transfer curves of a transistor based on a [5]Ph:PMMA blend (1:1, 10 g/l in 1,2-DCB), bar coated at 65 °C, with black line representing linear regime and the blue one for saturation regime. **e)** Mobility referred to the same transistor, in linear (black line) and saturation regimes (blue line). **f)** POM image of the same transistor, with 90° polarisation.

By observing the transistors through polarized optical microscopy, like in figure 6.11(c), it was found that the film had not formed properly on top of the lithography, probably due to poor

wetting of the solution on top of the gold contacts. Alternatively, it is possible that PMMA segregates on the contacts.

A second attempt was made to fabricate transistors out of this blend, with the same exact conditions of the previous test, except for the bed temperature at 60 °C to rule out thermal degradation from the possible issues affecting the previous batch of transistors. No remarkable difference was detected by electrical analysis (few devices worked), like shown in figure 6.11(d), although the film did look better by polarized optical microscopy, as displayed by figure 6.11(f), with respect to the previous case. Saturation mobilities ranged from $4 \cdot 10^{-6}$ cm²/Vs to $2 \cdot 10^{-5}$ cm²/Vs, saturation V_{on} spanned from -4 V up to -9 V, saturation V_{th} was between -15 V and -18 V and I_{on}/I_{off} ratio ranged from 4×10^3 to 10^4 , so a large variability among transistors was found. Again, it is possible to link the unpredictable behaviour of devices on the same sample to the inhomogeneity of the films.

The [5]Ph:PMMA blend was also tried out in BGBC configuration, but none of the devices worked.

6.2.5 Instability in transistors based on [5]Ph

As previously stated, [5]Ph films, as well as films from [5]Ph-polymer blends, are stable in air as well as in nitrogen atmosphere, but during electrical measurements a fraction of molecules is in charged state and their reactivity might increase with respect to the neutral condition, leading to transformations in the material. It is unclear if this can lead to the semiconductor reacting with oxygen, but for sure electrical measurements in air produce much worse results than those carried out in controlled nitrogen atmosphere.

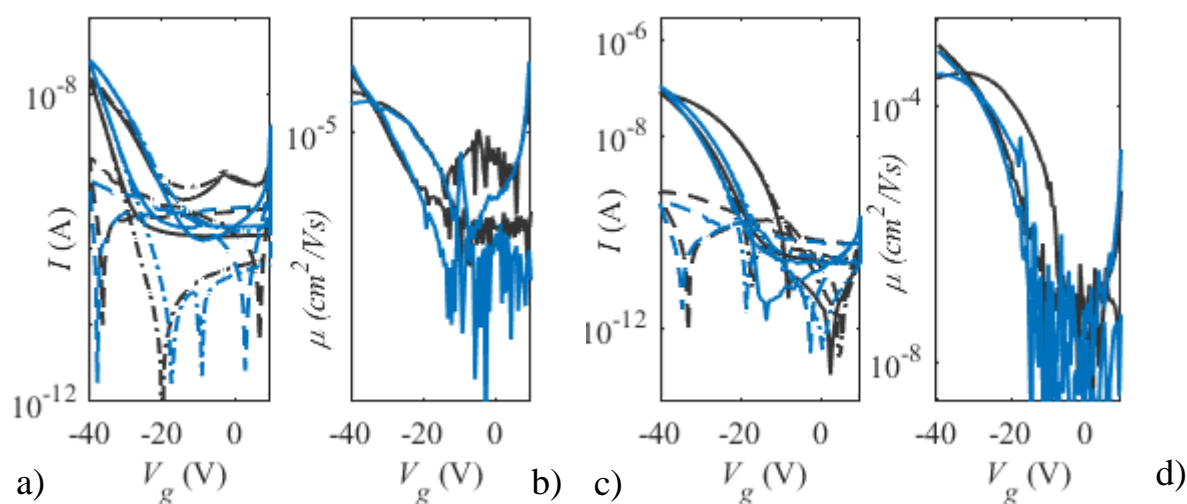


Figure 6.12 a) Characteristic transfer curves of a [5]Ph transistor measured in air, with black line representing linear regime ($V_D = -5$ V) and blue line saturation regime ($V_D = -40$ V); the solid line refers to the drain current,

while the dotted one to the gate current. **b)** Corresponding mobility. **c)** Characteristic transfer curves of a [5]Ph transistor measured in glovebox, with black line representing linear regime and blue line saturation regime. **d)** Corresponding mobility.

Figures 6.12(a)-(b) show the transfer and the mobility curves referred to a TGBC device, based on [5]Ph (10 g/l solution, 1,2-DCB), bar coated at 70 °C, with bar speed equal to 45 mm/s, with no N₂ flow, in dark conditions, in air, and measured in air. As a reference, figures 6.12(c)-(d) represent the same transistor, measured in nitrogen atmosphere right after the first run in air.

Neither measurement resulted in ideal transfer and mobility curves, but the one carried out in nitrogen showed some sign of recovery. In particular, detected I_d are higher, I_{on}/I_{off} ratio is higher, leakage is lower, saturation sweeps have less noticeable hysteresis, and both V_{on} and V_{th} reach less negative values, meaning that the device switches on earlier in nitrogen atmosphere. Mobilities are also greater in the nitrogen curves, even though a plateau was never reached, and the non-ideality of both curves, referred to air and nitrogen, makes the extraction of precise values very unreliable.

It needs to be pointed out that, although the SPA microscope was off during the measurement in air, it is possible that some light might have reached the device, contributing to [5]Ph degradation, while the setup inside the glovebox is more screened from light.

Provided that measurements in nitrogen produce better results than in air, another issue was encountered: detected on-currents, hence extracted mobility, seem to decrease at every measurement run on the same device. Figures 6.13(a) and 6.13(b) refer to a TGBC [5]Ph transistor (10 μm channel), and they underline how saturation (-40 V) I_d and saturation mobility decrease over 4 runs of SPA in nitrogen atmosphere, with a significant drop after the first one.

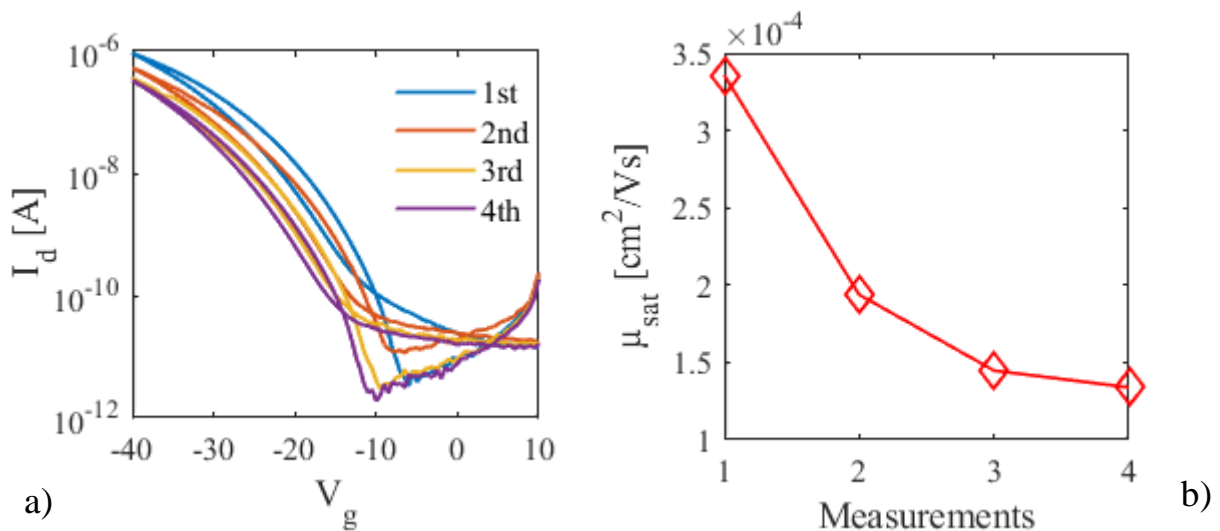


Figure 6.13 a) Characteristic transfer curves in saturation regime ($V_D = -40$ V) of a [5]Ph transistor, measured 4 times in a row. **b)** Corresponding trend in saturation charge mobility.

Whether this phenomenon is due to thermal effects, i.e. Joule heating, developing at high voltages (especially for short channels, since higher currents pass through them) or to increased reactivity triggered by the excited state, it is not clear, but this behaviour is consistent in all transistor batches fabricated during [5]Ph optimisation. If it is in fact due to thermal degradation, improving the overall transconductance of the device by reducing the channel resistance will also solve this issue, since the power emitted through Joule heating is directly dependant on the medium resistance.

Finally, [5]Ph is a photosensitive material. As such, protecting the devices from light was of paramount importance, and in order to do so the same strategies applied to [3]Ph transistors were tested out (Paragraph 6.1.2).

First of all, Figure 6.14(a) and 6.14(b) refer to a TGBC [5]Ph based transistor, and they show how the saturation ($V_D = -40$ V) transfer and mobility curves evolve during the experiment, when measurements were run under different lighting conditions, in nitrogen atmosphere.

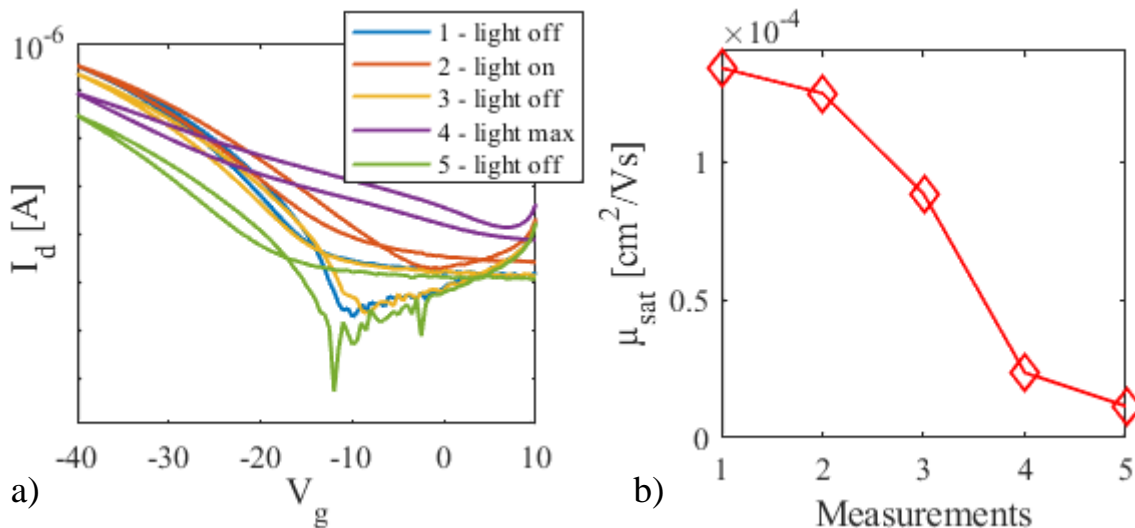


Figure 6.14 a) Characteristic transfer curves in saturation regime ($V_D = -40$ V) of a [5]Ph transistor, measured in 5 different lighting conditions. **b)** Corresponding trend in saturation charge mobility.

It is immediately noticeable how detrimental light is to the charge transport properties of the material. Reverse sweep hysteresis enlarged, I_d and I_{on}/I_{off} ratio dropped, subthreshold slope became more and more shallow, until the transistor stopped working as such.

In particular, the fourth measurement was run under high intensity light, and it matches with the most severe decrease in charge mobility.

The trend did not break when switching off the light, i.e. measurements 2 and 4, and this was likely due to thermal effects, as light can effectively heat up the material.

To counteract this liability, an activated carbon-based gate was considered.

The ink was spray-coated selectively on channel regions through a mask, with the same procedure employed in the fabrication of AC-gated [3]Ph transistors. Both formulations, with coarse and fine particles, were tried out.

Many devices were short-circuited, thus impossible to measure, others did not modulate the current.

The shorted-circuits were due to discontinuities in the Parylene layer, likely caused by spray coating. As for the other ones, the transistors were observed through POM to investigate the reasons behind the malfunctioning, and it was found that the thin film underneath the gate was damaged.

Figures 6.15(a) and 6.15(b) depict the active layer right beneath the spray coated AC gate, respectively in the channel region and away from the gold. There are obvious signs of degradation, such as voids and very small crystalline grains, leading to the impossibility of efficient charge transport across the channels.

As a reference, Figure 6.15(c) shows the film beneath an ink-jet printed PEDOT:PSS gate of a transistor from the same batch as the spray coated ones. The printed device features a homogeneous film after gating.

It is unclear why AC spray coating damaged the film this way, since [3]Ph beneath the same kind of gating do not display any hint of film disruption (Figure 6.15(d)).

In conclusion, an AC gate can be a good solution to photosensitivity in transistors, since it has been proved to work on [3]Ph, but it needs further optimisation. In particular, the deposition should be controlled so that it does not lead to neither dielectric nor active layer damage.

The aim of the opaque gate is to permanently protect the devices from light, but since it was not successful, a second gating strategy was tested. This second one involved a reduction in light exposure during fabrication: a PEDOT:PSS gate was wire-bar coated onto the dielectric layer, following the same procedure employed to gate [3]Ph transistors and described in Paragraph 6.1.2.

As mentioned in Paragraph 6.2.2 and shown in Figures 6.9(a) and 6.9(b), the bar coated gate worked perfectly on CMS-patterned transistors.

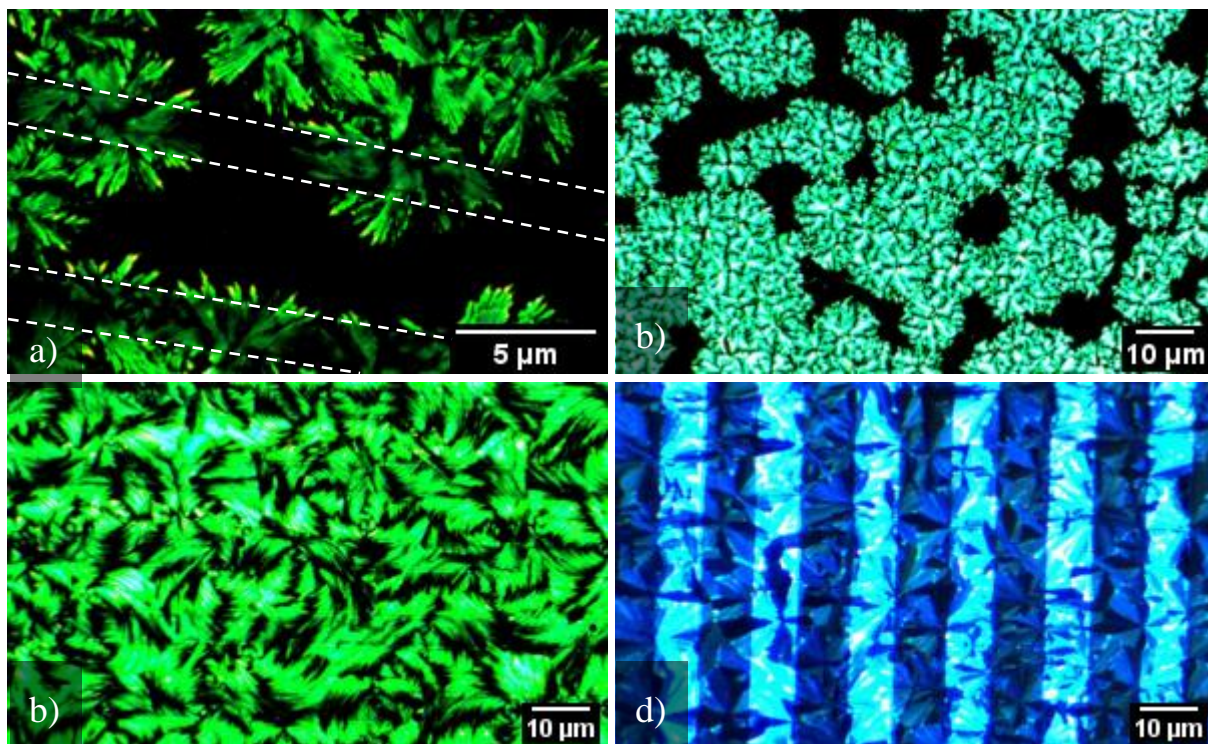


Figure 6.15 a) POM image of degraded [5]Ph thin film on gold contacts and beneath spray coated AC gate, with 90° polarisation. b) POM image of degraded [5]Ph thin film beneath AC gate, with 90° polarisation. c) POM image of pristine [5]Ph thin film on gold contacts and beneath printed PEDOT:PSS gate, with 90° polarisation. d) POM image of pristine [3]Ph thin film on gold contacts and beneath spray coated AC gate, with 90° polarisation.

CONCLUSIONS AND FUTURE WORK

The fabrication and optimisation of OFETs based on [5]Ph and [3]Ph was the focus of this thesis work.

In order to do so, the sensitivity of the two cumulenenic molecules with respect to photostimulation and temperature was tested. Cumulenes and *sp*-carbon molecules in general are notorious for their reactivity, and in order to optimise thin films of these materials for the fabrication of OFETs, it was of crucial importance to find out the amount of light and heat that they could tolerate, both in solution and in thin films.

Tests to induce thermal degradation and photodegradation were set up. Then, UV-Vis spectroscopy was employed to characterise the results, by monitoring the shape of the spectra and the intensity of the peaks.

[5]Ph solutions showed a very low resistance to heat, in comparison to [3]Ph, that proved to be stable over a decently wide range of temperatures. On the other hand, [3]Ph and [5]Ph films were very comparable.

As for light, both materials turned out to be more resistant than expected when in solution form. However, in thin film photodegradation was very quick to occur, especially for [3]Ph.

Taking the results from the stability tests into account, the optimisation of field effect transistors based on [3]Ph and [5]Ph films was pursued.

As for [3]Ph films, which had been studied for longer, this meant the development of solutions against photodegradation. So, two new gating strategies were tested, in an attempt of either permanently screening the devices from light or reducing the exposure during the fabrication step. Promising results were obtained from both routes.

[5]Ph, on the other hand, needed to be optimised, starting from the solution formulation and the film deposition conditions. [3]Ph was set as a reference, and it was eventually possible to fabricate [5]Ph field effect transistors with mobility up to 10^{-3} cm²/Vs and nearly ideal behaviour.

As for future studies, whether [5]Ph has the potential to further increase its mobility through optimisation is up to question. [3]Ph might be close to its limit, as well.

On the other hand, more characterisation analyses need to be run in order to better know these materials. There is on-going research to understand their packing, both in bulk and in thin films, which is crucial for charge transport mechanisms and potential properties.

A precise tailoring of cumulenic molecules, in terms of end groups, might help reaching a more efficient packing in solid state, favouring charge transport, so trying out new molecules from the [3]cumulenes and [5]cumulenes families could prove beneficial.

Finally, with a view to exploit the electrical characteristics of *sp*-carbon molecules to study them, polyynes could be used as the active layer of field effect transistors. They feature a larger energy gap and are thought to be less conductive. However, their increased stability allows polyynes chains to be much longer. Since BLA decreases with chain length and the energy gap is positively correlated with BLA, it is possible that at this stage polyynes might be better semiconductors than cumulenes.

BIBLIOGRAPHY

- [1] A. Hirsch, “The era of carbon allotropes,” *Nature Materials*, vol. 9, no. 11. Nature Publishing Group, pp. 868–871, 2010. doi: 10.1038/nmat2885.
- [2] C. Wang, H. Dong, L. Jiang, and W. Hu, “Organic semiconductor crystals,” *Chemical Society Reviews*, vol. 47, no. 2. Royal Society of Chemistry, pp. 422–500, Jan. 21, 2018. doi: 10.1039/c7cs00490g.
- [3] Z. A. Lamport, H. F. Haneef, S. Anand, M. Waldrip, and O. D. Jurchescu, “Tutorial: Organic field-effect transistors: Materials, structure and operation,” *Journal of Applied Physics*, vol. 124, no. 7, Aug. 2018, doi: 10.1063/1.5042255.
- [4] A. F. Paterson *et al.*, “Recent Progress in High-Mobility Organic Transistors: A Reality Check,” *Advanced Materials*, vol. 30, no. 36. Wiley-VCH Verlag, Sep. 06, 2018. doi: 10.1002/adma.201801079.
- [5] C. Liao, M. Zhang, M. Y. Yao, T. Hua, L. Li, and F. Yan, “Flexible Organic Electronics in Biology: Materials and Devices,” *Advanced Materials*, vol. 27, no. 46. Wiley-VCH Verlag, pp. 7493–7527, Dec. 01, 2015. doi: 10.1002/adma.201402625.
- [6] U. Haas, H. Gold, A. Haase, G. Jakopic, and B. Stadlober, “Submicron pentacene-based organic thin film transistors on flexible substrates,” *Applied Physics Letters*, vol. 91, no. 4, 2007, doi: 10.1063/1.2763973.
- [7] D. Wendinger and R. R. Tykwinski, “Odd [n]Cumulenes (n = 3, 5, 7, 9): Synthesis, Characterization, and Reactivity,” *Accounts of Chemical Research*, vol. 50, no. 6, pp. 1468–1479, Jun. 2017, doi: 10.1021/acs.accounts.7b00164.
- [8] R. B. Heimann, L. Kavan, and S. Evsyukov, *Carbyne and Carbynoid Structures*, vol. 21. Dordrecht: Springer Netherlands, 1999. doi: 10.1007/978-94-011-4742-2.
- [9] C. S. Casari *et al.*, “Chemical and thermal stability of carbyne-like structures in cluster-assembled carbon films,” *Physical Review B - Condensed Matter and Materials Physics*, vol. 69, no. 7, 2004, doi: 10.1103/PhysRevB.69.075422.

- [10] R. R. Tykwinski *et al.*, “Toward carbyne: Synthesis and stability of really long polyynes,” in *Pure and Applied Chemistry*, 2010, vol. 82, no. 4, pp. 891–904. doi: 10.1351/PAC-CON-09-09-04.
- [11] W. Luo and W. Windl, “First principles study of the structure and stability of carbynes,” *Carbon N Y*, vol. 47, no. 2, pp. 367–383, Feb. 2009, doi: 10.1016/j.carbon.2008.10.017.
- [12] A. D. Scaccabarozzi *et al.*, “A Field-Effect Transistor Based on Cumulenic sp-Carbon Atomic Wires,” *Journal of Physical Chemistry Letters*, vol. 11, no. 5, pp. 1970–1974, Mar. 2020, doi: 10.1021/acs.jpcclett.0c00141.
- [13] S. Pecorario *et al.*, “Stable and Solution-Processable Cumulenic sp-Carbon Wires: A New Paradigm for Organic Electronics,” *Advanced Materials*, 2022, doi: 10.1002/adma.202110468.
- [14] C. S. Casari and A. Milani, “Carbyne: From the elusive allotrope to stable carbon atom wires,” *MRS Communications*, vol. 8, no. 2, pp. 207–219, Jun. 2018, doi: 10.1557/mrc.2018.48.
- [15] C. S. Casari, M. Tommasini, R. R. Tykwinski, and A. Milani, “Carbon-atom wires: 1-D systems with tunable properties,” *Nanoscale*, vol. 8, no. 8, Royal Society of Chemistry, pp. 4414–4435, Feb. 28, 2016. doi: 10.1039/c5nr06175j.
- [16] J. A. Januszewski and R. R. Tykwinski, “Synthesis and properties of long [n]cumulenes ($n \geq 5$),” *Chemical Society Reviews*, vol. 43, no. 9. Royal Society of Chemistry, pp. 3184–3203, May 07, 2014. doi: 10.1039/c4cs00022f.
- [17] M. Liu, V. I. Artyukhov, H. Lee, F. Xu, and B. I. Yakobson, “Carbyne from first principles: Chain of c atoms, a nanorod or a nanorope,” *ACS Nano*, vol. 7, no. 11, pp. 10075–10082, Nov. 2013, doi: 10.1021/nn404177r.
- [18] P. B. Sorokin, H. Lee, L. Y. Antipina, A. K. Singh, and B. I. Yakobson, “Calcium-decorated carbyne networks as hydrogen storage media,” *Nano Letters*, vol. 11, no. 7, pp. 2660–2665, Jul. 2011, doi: 10.1021/nl200721v.
- [19] M. Wang and S. Lin, “Ballistic Thermal Transport in Carbyne and Cumulene with Micron-Scale Spectral Acoustic Phonon Mean Free Path,” *Scientific Reports*, vol. 5, Dec. 2015, doi: 10.1038/srep18122.
- [20] A. Milani, M. Tommasini, and G. Zerbi, “Carbynes phonons: A tight binding force field,” *Journal of Chemical Physics*, vol. 128, no. 6, 2008, doi: 10.1063/1.2831507.

- [21] N. R. Agarwal *et al.*, “Structure and chain polarization of long polyynes investigated with infrared and Raman spectroscopy,” in *Journal of Raman Spectroscopy*, Oct. 2013, vol. 44, no. 10, pp. 1398–1410. doi: 10.1002/jrs.4300.
- [22] M. Tommasini *et al.*, “ π -Conjugation and End Group Effects in Long Cumulenes: Raman Spectroscopy and DFT Calculations,” *Journal of Physical Chemistry C*, vol. 118, no. 45, pp. 26415–26425, Nov. 2014, doi: 10.1021/jp509724d.
- [23] A. Milani, M. Tommasini, D. Fazzi, C. Castiglioni, M. del Zoppo, and G. Zerbi, “First-principles calculation of the Peierls distortion in an infinite linear carbon chain: The contribution of Raman spectroscopy,” in *Journal of Raman Spectroscopy*, Feb. 2008, vol. 39, no. 2, pp. 164–168. doi: 10.1002/jrs.1850.
- [24] A. Milani *et al.*, “Raman spectroscopy as a tool to investigate the structure and electronic properties of carbon-atom wires,” *Beilstein Journal of Nanotechnology*, vol. 6, no. 1, pp. 480–491, 2015, doi: 10.3762/bjnano.6.49.
- [25] A. Milani *et al.*, “Charge transfer and vibrational structure of sp-hybridized carbon atomic wires probed by surface enhanced raman spectroscopy,” *Journal of Physical Chemistry C*, vol. 115, no. 26, pp. 12836–12843, Jul. 2011, doi: 10.1021/jp203682c.
- [26] W. A. Chalifoux and R. R. Tykwinski, “Synthesis of polyynes to model the sp-carbon allotrope carbyne,” *Nature Chemistry*, vol. 2, no. 11, pp. 967–971, Nov. 2010, doi: 10.1038/nchem.828.
- [27] S. Yang and M. Kertesz, “Linear C_n clusters: Are they acetylenic or cumulenic?,” *Journal of Physical Chemistry A*, vol. 112, no. 1, pp. 146–151, Jan. 2008, doi: 10.1021/jp076805b.
- [28] X. Zhao, Y. Ando, Y. Liu, M. Jinno, and T. Suzuki, “Carbon Nanowire Made of a Long Linear Carbon Chain Inserted Inside a Multiwalled Carbon Nanotube,” *Physical Review Letters*, vol. 90, no. 18, p. 4, 2003, doi: 10.1103/PhysRevLett.90.187401.
- [29] M. Tommasini, D. Fazzi, A. Milani, M. del Zoppo, C. Castiglioni, and G. Zerbi, “Effective hamiltonian for π electrons in linear carbon chains,” *Chemical Physics Letters*, vol. 450, no. 1–3, pp. 86–90, Dec. 2007, doi: 10.1016/j.cplett.2007.10.100.
- [30] W. Xu *et al.*, “Unusual Length Dependence of the Conductance in Cumulene Molecular Wires,” *Angewandte Chemie*, May 2019, doi: 10.1002/ange.201901228.
- [31] J. A. Januszewski, D. Wendinger, C. D. Methfessel, F. Hampel, and R. R. Tykwinski, “Synthesis and structure of tetraarylcumulenes: Characterization of bond-length alternation versus molecule length,” *Angewandte Chemie - International Edition*, vol. 52, no. 6, pp. 1817–1821, Feb. 2013, doi: 10.1002/anie.201208058.

- [32] M. Franz *et al.*, “Cumulen-Rotaxane: Stabilisierung und Charakterisierung von [9]Cumulenen,” *Angewandte Chemie*, vol. 127, no. 22, pp. 6746–6750, May 2015, doi: 10.1002/ange.201501810.
- [33] B. Sun *et al.*, “The effects of ring strain on cyclic tetraaryl[5]cumulenes,” *Chemistry – A European Journal*, Apr. 2022, doi: 10.1002/chem.202200616.
- [34] C. Castiglioni, M. del Zoppo, and G. Zerbi, “Vibrational Raman spectroscopy of polyconjugated organic oligomers and polymers,” *Journal of Raman Spectroscopy*, vol. 24, no. 8, pp. 485–494, Aug. 1993, doi: 10.1002/jrs.1250240804.
- [35] S. M. Sze and K. K. Ng, *Physics of Semiconductor Devices*, 3rd ed. New York: Wiley, 2007. doi: 10.1002/0470068329.
- [36] G. Horowitz, “Organic Field-Effect Transistors,” *Advanced Materials*, vol. 10, no. 5, pp. 365–377, 1998.
- [37] D. Natali and M. Caironi, “Charge injection in solution-processed organic field-effect transistors: Physics, models and characterization methods,” *Advanced Materials*, vol. 24, no. 11, pp. 1357–1387, Mar. 15, 2012. doi: 10.1002/adma.201104206.
- [38] C. Wang, H. Dong, W. Hu, Y. Liu, and D. Zhu, “Semiconducting π -conjugated systems in field-effect transistors: A material odyssey of organic electronics,” *Chemical Reviews*, vol. 112, no. 4, pp. 2208–2267, Apr. 11, 2012. doi: 10.1021/cr100380z.
- [39] A. D. Scaccabarozzi and N. Stingelin, “Semiconducting:insulating polymer blends for optoelectronic applications - A review of recent advances,” *Journal of Materials Chemistry A*, vol. 2, no. 28, Royal Society of Chemistry, pp. 10818–10824, Jul. 28, 2014. doi: 10.1039/c4ta01065e.
- [40] T. Ohe, M. Kuribayashi, A. Tsuboi, K. Satori, M. Itabashi, and K. Nomoto, “Organic thin-film transistors with phase separation of polymer-blend small-molecule semiconductors: Dependence on molecular weight and types of polymer,” *Applied Physics Express*, vol. 2, no. 12, Dec. 2009, doi: 10.1143/APEX.2.121502.
- [41] S. Ciuchi, S. Fratini, and D. Mayou, “Transient localization in crystalline organic semiconductors,” *Physical Review B - Condensed Matter and Materials Physics*, vol. 83, no. 8, Feb. 2011, doi: 10.1103/PhysRevB.83.081202.
- [42] J. L. Bredas and G. B. Street, “Polarons, Bipolarons, and Solitons in Conducting Polymers,” 1985. [Online]. Available: <https://pubs.acs.org/sharingguidelines>
- [43] N. Vukmirović, C. Bruder, and V. M. Stojanović, “Electron-phonon coupling in crystalline organic semiconductors: Microscopic evidence for nonpolaronic charge

- carriers,” *Physical Review Letters*, vol. 109, no. 12, Sep. 2012, doi: 10.1103/PhysRevLett.109.126407.
- [44] A. Troisi, “Dynamic disorder in molecular semiconductors: Charge transport in two dimensions,” *Journal of Chemical Physics*, vol. 134, no. 3, Jan. 2011, doi: 10.1063/1.3524314.
- [45] S. Fratini, D. Mayou, and S. Ciuchi, “The transient localization scenario for charge transport in crystalline organic materials,” *Advanced Functional Materials*, vol. 26, no. 14, pp. 2292–2315, May 2015, doi: <https://doi.org/10.1002/adfm.201502386>.
- [46] P. A. Lee and T. v Ramakrishnan, “Disordered electronic systems,” *Reviews of Modern Physics*, vol. 57, no. 2, pp. 287–337, 1985.
- [47] P. W. Anderson, “Absence of Diffusion in Certain Random Lattices,” *Physical Review*, vol. 109, no. 5, pp. 1492–1505, 1958.
- [48] K. P. Pernstich, B. Rössner, and B. Batlogg, “Field-effect-modulated Seebeck coefficient in organic semiconductors,” *Nature Materials*, vol. 7, no. 4, pp. 321–325, 2008, doi: 10.1038/nmat2120.
- [49] V. Coropceanu, M. Malagoli, D. A. da Silva Filho, N. E. Gruhn, T. G. Bill, and J. L. Brédas, “Hole- and Electron-Vibrational Couplings in Oligoacene Crystals: Intramolecular Contributions,” *Physical Review Letters*, vol. 89, no. 27, 2002, doi: 10.1103/PhysRevLett.89.275503.
- [50] A. S. Eggeman, S. Illig, A. Troisi, H. Sirringhaus, and P. A. Midgley, “Measurement of molecular motion in organic semiconductors by thermal diffuse electron scattering,” *Nature Materials*, vol. 12, no. 11, pp. 1045–1049, Nov. 2013, doi: 10.1038/nmat3710.
- [51] A. S. Mishchenko, H. Matsui, and T. Hasegawa, “Distribution of localized states from fine analysis of electron spin resonance spectra of organic semiconductors: Physical meaning and methodology,” *Physical Review B - Condensed Matter and Materials Physics*, vol. 85, no. 8, Feb. 2012, doi: 10.1103/PhysRevB.85.085211.
- [52] J. F. Chang *et al.*, “Hall-effect measurements probing the degree of charge-carrier delocalization in solution-processed crystalline molecular semiconductors,” *Physical Review Letters*, vol. 107, no. 6, Aug. 2011, doi: 10.1103/PhysRevLett.107.066601.
- [53] M. Egginger, S. Bauer, R. Schwödianer, H. Neugebauer, and N. S. Sariciftci, “Current versus gate voltage hysteresis in organic field effect transistors,” *Monatshefte für Chemie*, vol. 140, no. 7, pp. 735–750, Jul. 2009, doi: 10.1007/s00706-009-0149-z.

- [54] S. Singh and Y. N. Mohapatra, "Bias stress effect in solution-processed organic thin-film transistors: Evidence of field-induced emission from interfacial ions," *Organic Electronics*, vol. 51, pp. 128–136, Dec. 2017, doi: 10.1016/j.orgel.2017.09.007.
- [55] J. Veres, S. D. Ogier, S. W. Leeming, D. C. Cupertino, and S. M. Khaffaf, "Low-k Insulators as the Choice of Dielectrics in Organic Field-Effect Transistors," *Advanced Functional Materials*, vol. 13, no. 3, pp. 199–204, 2003.
- [56] M. T. Soliman, "Electrical Transport Properties Investigation of Sp-Carbon Linear Atomic Chains-based Molecular Crystals," 2018.
- [57] S. Fratini, M. Nikolka, A. Salleo, G. Schweicher, and H. Sirringhaus, "Charge transport in high-mobility conjugated polymers and molecular semiconductors," *Nature Materials*, vol. 19, no. 5. Nature Research, pp. 491–502, May 01, 2020. doi: 10.1038/s41563-020-0647-2.
- [58] T. Losi, "Master Thesis - Field-Effect Transistors Based on Sp²-Sp Carbon Molecules," 2019.
- [59] Z. Zhang, B. Peng, X. Ji, K. Pei, and P. K. L. Chan, "Marangoni-Effect-Assisted Bar-Coating Method for High-Quality Organic Crystals with Compressive and Tensile Strains," *Advanced Functional Materials*, vol. 27, no. 37, Oct. 2017, doi: 10.1002/adfm.201703443.
- [60] S. B. Lee, S. Lee, D. G. Kim, S. H. Kim, B. Kang, and K. Cho, "Solutal-Marangoni-Flow-Mediated Growth of Patterned Highly Crystalline Organic Semiconductor Thin Film Via Gap-Controlled Bar Coating," *Advanced Functional Materials*, vol. 31, no. 28, Jul. 2021, doi: 10.1002/adfm.202100196.
- [61] D. Khim *et al.*, "Simple bar-coating process for large-area, high-performance organic field-effect transistors and ambipolar complementary integrated circuits," *Advanced Materials*, vol. 25, no. 31, pp. 4302–4308, Aug. 2013, doi: 10.1002/adma.201205330.
- [62] S. Arulkumar *et al.*, "AgNWs-a-TiOx: a scalable wire bar coated core-shell nanocomposite as transparent thin film electrode for flexible electronics applications," *Journal of Materials Science: Materials in Electronics*, vol. 32, no. 5, pp. 6454–6464, Mar. 2021, doi: 10.1007/s10854-021-05362-2.
- [63] T. Marszalek, M. Gazicki-Lipman, and J. Ulanski, "Parylene C as a versatile dielectric material for organic field-effect transistors," *Beilstein Journal of Nanotechnology*, vol. 8, no. 1. Beilstein-Institut Zur Forderung der Chemischen Wissenschaften, pp. 1532–1545, 2017. doi: 10.3762/bjnano.8.155.

- [64] B. Weng, R. L. Shepherd, K. Crowley, A. J. Killard, and G. G. Wallace, "Printing conducting polymers," *Analyst*, vol. 135, no. 11. Royal Society of Chemistry, pp. 2779–2789, 2010. doi: 10.1039/c0an00302f.
- [65] S. Riera-Galindo, A. Tamayo, and M. Mas-Torrent, "Role of Polymorphism and Thin-Film Morphology in Organic Semiconductors Processed by Solution Shearing," *ACS Omega*, vol. 3, no. 2, pp. 2329–2339, Feb. 2018, doi: 10.1021/acsomega.8b00043.
- [66] H. Teng, K. Koike, D. Zhou, Z. Satoh, Y. Koike, and Y. Okamoto, "High glass transition temperatures of poly(methyl methacrylate) prepared by free radical initiators," *Journal of Polymer Science, Part A: Polymer Chemistry*, vol. 47, no. 1, pp. 315–317, Jan. 2009, doi: 10.1002/pola.23154.
- [67] K. F. Kelton, "Analysis of crystallization kinetics," 1997.
- [68] N. Sangiorgi, L. Aversa, R. Tatti, R. Verucchi, and A. Sanson, "Spectrophotometric method for optical band gap and electronic transitions determination of semiconductor materials," *Opt Mater (Amst)*, vol. 64, pp. 18–25, Feb. 2017, doi: 10.1016/j.optmat.2016.11.014.
- [69] N. Islam, T. Ooi, T. Iwasawa, M. Nishiuchi, and Y. Kawamura, "Thermal cyclotrimerization of tetraphenyl[5]cumulene (tetraphenylhexapentaene) to a tricyclodecadiene derivative," *Chemical Communications*, no. 5, pp. 574–576, 2009, doi: 10.1039/b815620d.
- [70] S. Riera-Galindo, F. Leonardi, R. Pfattner, and M. Mas-Torrent, "Organic Semiconductor/Polymer Blend Films for Organic Field-Effect Transistors," *Advanced Materials Technologies*, vol. 4, no. 9. Wiley-Blackwell, Sep. 01, 2019. doi: 10.1002/admt.201900104.

LIST OF FIGURES

Figure 1.1 Carbon orbitals in a) sp^3 -hybridisation; b) sp^2 -hybridisation; c) sp -hybridisation. . .	4
Figure 1.2 a) Schematic structure of a polyynes, with r_1 referred to the triple bond length and r_2 referred to the single bond length. b) Schematic structure of a cumulene, with equally long bonds.	5
Figure 1.3 Structure energy in function of BLA, with a maximum in correspondence of the ideal cumulene, with BLA = 0 [15].	6
Figure 1.4 Energy band gap in function of BLA. A trend associated to wire length, so to the number of carbon atoms, is also shown [29].	7
Figure 1.5 a) π -systems of even aryl-substituted cumulenes. b) π -systems of odd aryl-substituted cumulenes [16].	8
Figure 1.6 [9]cumulene stabilised by bulky end groups and a rotaxane molecule [31].	9
Figure 2.1 Schematic representation of the structure of an OFET.	11
Figure 2.2 Transfer curves of an ideal OFET in a) linear regime and b) saturation regime, with the current in logarithmic scale. c) Output curve of an ideal OFET.	13
Figure 2.3 a) - b) are respectively the schematic representation and the output curve of the linear regime. c) – d) represent the pinch-off point. e) – f) are referred to the saturation regime.	14
Figure 2.4 Schematic representations of devices in configurations: a) TGTC; b) TGBC; c) BGTC; d) BGBC.	16
Figure 2.5 a) Wave function of an extended state, l being the mean free path. b) Localised state, showing the wave function (solid line) decaying to zero assisted by the envelope function (dotted line) [45].	19
Figure 2.6 Time scale against charge carrier diffusion [44].	20

Figure 2.7 Transfer curves showing a) lower back sweep current (BSC) hysteresis, and b) higher BSC hysteresis [52].	22
Figure 2.8 Schematic representation of the phenomena leading to BSC hysteresis [52].	23
Figure 3.1 a) 2D structure of [3]Ph. b) 2D structure of [5]Ph. c) 3D structure of [3]Ph. d) 3D structure of [5]Ph.	26
Figure 3.2 [5]Ph synthesis, carried out by Rik Tykwinski and his team; "Ar" represents phenyl groups [7].	26
Figure 3.3 a) Polystyrene repeat unit. b) Poly(methyl methacrylate) repeat unit.	28
Figure 3.4 a) Schematic representation of a typical Fraunhofer pattern, with a channel width of 2 mm and channel lengths spanning from 2.5 μm to 20 μm . b) "CMS" pattern, with a channel width of 2 cm and channel lengths ranging from 5 μm to 40 μm .	30
Figure 3.5 Schematic representation of the lithographic and contact deposition process for a TGBC device: a) spin coating of LOR and positive photoresist S1813, onto thoroughly cleaned Corning glass; b) UV-curing of S1813; c) developing step, leading to cured S1813 and LOR dissolution, and to the formation of an undercut; d) thermal evaporation of Gold all over the surface; e) removal of the resists and of excess metal during the lift-off step, leading to patterned Gold on glass substrate. f) Patterned gold on Parylene in BGBC configuration.	32
Figure 3.6 a) Schematic representation of the bar coating process [61]. b) Representation of a wire-bar creating a meniscus [60]. c) Regimes of deposition and thickness trends according to the bar speed-thickness relation [59].	35
Figure 3.7 Parylene C repeat unit.	35
Figure 3.8 a) PEDOT and PSS repeat units. b) Schematic representation of the piezo-ceramic in an ink-jet printer cartridge [63].	37
Figure 3.9 a) Schematic representation of a TGBC device. b) Schematic representation of a BGBC device.	38
Figure 3.10 a) POM image of a [3]Ph film, after being exposed to the light of the microscope for 60 seconds, 90° polarisation. b) POM image of a [5]Ph film, split into a undegraded region and a region exposed to the light of the microscope for 60 seconds; 90° polarisation.	39
Figure 3.11 Setup for photodegradation analysis, involving a white light source and a LED.	41
Figure 3.12 Schematic representation of the working principle of an AFM.	44
Figure 4.1 Arrangement of [3]Ph, whose chains are quasi-parallel to the substrate [13].	46

Figure 4.2 a) POM image of a [5]Ph film, wire-bar coated at $T = 60\text{ }^{\circ}\text{C}$, with bar speed $v = 45\text{ mm/s}$, with N_2 flow off, in dark conditions, in air, from a 5 g/l in 1,2-DCB solution, taken with 90° polarisation. b) POM image of a [5]Ph film, wire-bar coated at the same conditions, but from a 20 g/l solution, taken with 90° polarisation.	47
Figure 4.3 a) POM image of the main structure in a [5]Ph:PS film, taken with 90° polarisation. b) POM image of the main structure in a [5]Ph:PMMA film, taken with 90° polarisation.	48
Figure 4.4 a) POM image of a film based on the blend [5]Ph:PS (5 g/l : 15 g/l in 1,2-DCB), wire-bar coated at $T = 80\text{ }^{\circ}\text{C}$, with bar speed of 30 mm/s, with no nitrogen flow, in dark conditions, in air; picture taken under 90° polarisation. b) POM image of a film based on the blend [5]Ph:PMMA (5 g/l : 15 g/l in 1,2-DCB), wire-bar coated at the same conditions as before.....	49
Figure 4.5 POM images (90° polarisation) of [5]Ph film wire-bar coated at a) room temperature, b) $60\text{ }^{\circ}\text{C}$, c) $70\text{ }^{\circ}\text{C}$, d) $80\text{ }^{\circ}\text{C}$, e) $110\text{ }^{\circ}\text{C}$. f) POM image of the arched, fibre-like structures, commonly present as defects in [5]Ph films.	51
Figure 4.6 POM images (90° polarisation) of films bar coated from [5]Ph:PMMA (1:1, 10 g/l in 1,2-DCB) solutions a) at $60\text{ }^{\circ}\text{C}$ and b) at $80\text{ }^{\circ}\text{C}$	51
Figure 4.7 POM images (90° polarisation) of films bar coated from [5]Ph:PS (1:1, 10 g/l in 1,2-DCB) at a) $60\text{ }^{\circ}\text{C}$ and b) $80\text{ }^{\circ}\text{C}$	52
Figure 4.8 Absorption spectrum of a [5]Ph solution (0,01 g/l in 1,2-DCB). The inset, from [16], represents the molecular orbitals of [5]Ph, specifically its two π -systems.	54
Figure 4.9 a) Absorption spectra of [5]Ph in optimised thin film and in solution (0,01 g/l in 1,2-DCB), each normalised to their maxima. b) Absorption spectra of [3]Ph in optimised thin film and in solution (0,01 g/l in 1,2-DCB), each normalised to their maxima.	55
Figure 4.10 AFM 2D images of [5]Ph films, bar coated from a 10 g/l solution in 1,2-DCB, at $70\text{ }^{\circ}\text{C}$, in dark conditions, without nitrogen flow, in air a) at bar speed equal to 15 mm/s, and b) at bar speed equal to 45 mm/s. c) AFM 3D image of the same sample as a). d) AFM 3D image of the same sample as b). e) POM image of the same sample as a)-c), taken under 90° polarisation. f) POM image of the same sample as b)-d), taken under 90° polarisation.....	56
Figure 4.11 AFM images of a [5]Ph film, bar coated at $80\text{ }^{\circ}\text{C}$, 45 mm/s, in dark conditions, in air: a) 2D and b) 3D.....	57
Figure 4.12 a) Band structure diagram, representing the values extracted by UPS analysis. b) UPS spectrum acquired on [5]Ph film by Mirko Prato, at MCF@IIT.	59

Figure 4.13 UV-Vis absorption spectrum of an optimised [5]Ph film, showing the onset of the peak associated to the HOMO-LUMO transition.....	60
Figure 5.1 a) UV-Vis absorbance spectra of a [5]Ph in 1,2-DCB solution (0.01 g/l); the spectra are normalised to the peak of the fresh solution. b) POM picture of a thin film deposited from the old [5]Ph solution.	62
Figure 5.2 Absorbance spectra before and after 30 seconds of white light stimulation for a) [3]Ph (0.01 g/l in 1,2-DCB) solution, and b) [5]Ph (0.01 g/l in 1,2-DCB) solution.	63
Figure 5.3 Trend of the absorption peak of [3]Ph and [5]Ph 0.01 g/l solutions during the test at different wavelengths.	64
Figure 5.4 a-e) Absorbance spectra of the [5]Ph solution (0.01 g/l in 1,2-DCB) during 30-second long intervals of irradiation at 660 nm, 530 nm, 470 nm, 405 nm, 365 nm. f) Absorbance spectrum before and after the test.....	65
Figure 5.5 a-e) Absorbance spectra of the [5]Ph solution (0.01 g/l in 1,2-DCB) during 30-second long intervals of irradiation at 660 nm, 530 nm, 470 nm, 405 nm, 365 nm. f) Absorbance spectrum before and after the test.....	66
Figure 5.6 Absorbance spectra under white light of thin films of a) [3]Ph, and b) [5]Ph.....	67
Figure 5.7 Trend of the absorption peak of [3]Ph and [5]Ph 0.01 g/l solutions during the test at different wavelengths.	68
Figure 5.8 Evolution of the absorption spectrum of [3]Ph films during irradiation for 30 seconds with light having wavelength a) 660 nm, b) 530 nm, c) 470 nm, d) 405 nm, e) 365 nm. f) Absorbance spectra after each interval.....	69
Figure 5.9 Evolution of the absorption spectrum of [5]Ph films during irradiation for 30 seconds with light having wavelength a) 660 nm, b) 530 nm, c) 470 nm, d) 405 nm, e) 365 nm. f) Absorbance spectra after each interval.....	70
Figure 5.10 POM pictures of a),c) undegraded [3]Ph and [5]Ph, respectively, and b),d) degraded [3]Ph and [5]Ph.	71
Figure 5.11 a) DSC and b) TGA performed on [5]Ph crystals, by Prof. Rik Tykwinski and his team (University of Alberta).	73
Figure 5.12 a) Evolution of [3]Ph solution absorption spectrum after 30-minute long intervals at set temperatures. b) Evolution of [5]Ph solution absorption spectrum after 30-minute long intervals at set temperatures. c) Comparison of the trends of the absorption peak of [3]Ph and [5]Ph solutions, as they are heated at 50 °C, 80 °C, 100 °C, 120 °C, 140 °C.....	74

Figure 5.13 a) Evolution of [5]Ph absorption spectrum after 3 hours at 50 °C. b) Trend of [5]Ph absorption peak hour by hour when the solution is heated at 35 °C.	75
Figure 5.14 Effect of 30-minute long intervals at 50 °C, 80 °C, 100 °C, 120 °C on thin films of a) [3]Ph and b) [5]Ph, each heated at one temperature.	76
Figure 5.15 Evolution in [3]Ph and [5]Ph thin film structures, when heated up at 50°C, 80 °C, 100 °C, 120 °C.	78
Figure 5.16 Effect of accumulated 30-minute long intervals at 50 °C, 80 °C, 100 °C, 120 °C on thin films of a) [3]Ph and b) [5]Ph.	79
Figure 5.17 Effect of at 30-minute long interval on a) [3]Ph thin film at 100 °C, and b) [5]Ph thin film at 80 °C, when both samples are left in high vacuum.	79
Figure 6.1a) Characteristic transfer curves in both linear and saturation regimes (black and blue lines, respectively) in a TGBC OFET based on [3]Ph [13]. b) Charge mobility against gate voltage in both linear and saturation regimes [13]. c) POM image of [3]Ph film wire-bar coated on gold contacts, underlined by the dotted line.	82
Figure 6.2 Structure of an AC gated [3]Ph transistor, in TGBC configuration.	83
Figure 6.3 a) Characteristic transfer curves of a transistor based on [3]Ph and gated through a spray coated activated carbon ink; the black line refers to linear regime (-5 V), the blue one to saturation regime (-40 V); the solid line is the drain current, the dotted one the gate current. b) Corresponding charge mobility curves. c) Characteristic transfer curve of a transistor from the same batch based on [3]Ph and gated through ink-jet printed PEDOT:PSS. d) Corresponding charge mobility curve.	84
Figure 6.4 a) Transfer curves from a [3]Ph based transistor gated through spray coated AC ink, measured under different light conditions. b) Transfer curves from a [3]Ph based transistor gated through ink-jet printed PEDOT:PSS, measured under different light conditions. c) Comparison between the mobility curves referred to the previous devices, each normalised to their maximum value.	85
Figure 6.5 TGBC [3]Ph based transistor, gated by bar coated PEDOT:PSS.	86
Figure 6.6 a) Transfer curves of a transistor based on dropcasted [5]Ph on Fraunhofer substrate, with black line representing linear regime and the blue one for saturation regime. b) Mobility referred to the same transistor, in linear (black line) and saturation regimes (blue line). c) POM picture of the transistor, with 90° polarisation. d) POM picture of the dropcasted [5]Ph structures, with 90° polarisation.	88

- Figure 6.7 a) POM image of a solution of “C6-5” dropcasted onto Fraunhofer substrate, with a polarisation of 90° , showing isolated agglomerates in amorphous matrix. b) POM image of a solution of “C6-5” dropcasted onto Fraunhofer substrate, with a polarisation of 90° , also showing agglomerates in amorphous matrix. 89
- Figure 6.8 a) Transfer curves of a transistor based on bar coated [5]Ph (10 g/l in 1,2-DCB), with black line representing linear (-5 V) regime and the blue one for saturation regime (-40 V); solid line refers to drain current, while the dotted one is for gate current. b) Mobility referred to the same transistor, in linear (black line) and saturation regimes (blue line). c) POM image of the same transistor, with 90° polarisation. d) Standard deviation of the currents, in log scale, across all the measured transistors of a same batch, in linear regime. e) Standard deviation of the currents, in log scale, across the measured devices, in saturation regime. 92
- Figure 6.9 a) Characteristic transfer curves of a transistor based on optimised [5]Ph, showing in black the linear regime and in blue the saturation one. b) Corresponding mobilities of the same device. c) POM image of the same transistor, with 90° polarisation. d) Output curves referred to one of the other devices from the same batch. 94
- Figure 6.10 a) Transfer curves of a transistor based on bar coated [5]Ph:PS blend (1:1, 10 g/l in 1,2-DCB), with black line representing linear regime ($V_D = -5$ V) and the blue one for saturation regime ($V_D = -40$ V); the solid line refers to drain current, the dotted one to gate current. b) Mobility referred to the same transistor, in linear (black line) and saturation regimes (blue line). c) POM image of the same transistor, with 90° polarisation: the channels are emphasised by the white dotted line. 95
- Figure 6.11 a) Transfer curves of a transistor based on a [5]Ph:PMMA blend (1:1, 10 g/l in 1,2-DCB), bar coated at 80°C , with black line representing linear regime ($V_D = -5$ V) and the blue one for saturation regime ($V_D = -40$ V); the solid line is for drain current, the dotted one for gate current. b) Mobility referred to the same transistor, in linear (black line) and saturation regimes (blue line). c) POM image of the same transistor, with 90° polarisation. d) Transfer curves of a transistor based on a [5]Ph:PMMA blend (1:1, 10 g/l in 1,2-DCB), bar coated at 65°C , with black line representing linear regime and the blue one for saturation regime. e) Mobility referred to the same transistor, in linear (black line) and saturation regimes (blue line). f) POM image of the same transistor, with 90° polarisation. 96
- Figure 6.12 a) Characteristic transfer curves of a [5]Ph transistor measured in air, with black line representing linear regime ($V_D = -5$ V) and blue line saturation regime ($V_D = -40$ V); the solid line refers to the drain current, while the dotted one to the gate current. b) Corresponding mobility. c) Characteristic transfer curves of a [5]Ph transistor measured in glovebox, with

black line representing linear regime and blue line saturation regime. d) Corresponding mobility.	97
Figure 6.13 a) Characteristic transfer curves in saturation regime ($V_D = -40$ V) of a [5]Ph transistor, measured 4 times in a row. b) Corresponding trend in saturation charge mobility.	98
Figure 6.14 a) Characteristic transfer curves in saturation regime ($V_D = -40$ V) of a [5]Ph transistor, measured in 5 different lighting conditions. b) Corresponding trend in saturation charge mobility.....	99
Figure 6.15 a) POM image of degraded [5]Ph thin film on gold contacts and beneath spray coated AC gate, with 90° polarisation. b) POM image of degraded [5]Ph thin film beneath AC gate, with 90° polarisation. c) POM image of pristine [5]Ph thin film on gold contacts and beneath printed PEDOT:PSS gate, with 90° polarisation. d) POM image of pristine [3]Ph thin film on gold contacts and beneath spray coated AC gate, with 90° polarisation.	101

ACKNOWLEDGEMENTS

First, I thank Prof. Carlo S. Casari, my supervisor, and Mario Caironi, co-supervisor, for giving me the incredible opportunity to work on this project.

My most sincere gratitude goes to Stefano Pecorario, co-supervisor, who patiently guided me through all the stages involved in this work, from laboratory activities to thesis writing.

I also wish to express my appreciation to all the people at the Center of Nano Science and Technology (IIT) for providing a welcoming, diverse and enriching environment where I could learn so much.

Finally, I could have never got so far without the unconditional support of my family and of my closest friends, who stood by me and believed in me all throughout my university studies – even and especially when I was struggling.

